ABSTRACT

Title of Dissertation:	SEA-SURFACE TEMPERATURE BASED STATISTICAL PREDICTION OF THE SOUTH ASIAN SUMMER MONSOON RAINFALL DISTRIBUTION
	Agniv Sengupta, Doctor of Philosophy, 2019
Dissertation directed by:	Professor Sumant Nigam Department of Atmospheric and Oceanic Science

The South Asian summer monsoon brings copious amounts of rainfall accounting for over 70% of the annual rainfall over India. Summer monsoon predictions have drawn considerable public/policy attention lately as South Asia has become a resource-stressed and densely populated region. This environmental backdrop and the livelihood concerns of a billion-plus people generate the demand for more accurate monsoon predictions. The prediction skill, however, has remained marginal and stagnant for several decades despite advances in the representation of physical processes, numerical model resolution, and data assimilation techniques, leading to the following key question: what is the potential predictability of summer monsoon rainfall at lead times of one month to a season?

This dissertation examines the role of influential climate system components with large thermal inertia and reliable long-term observational records, like sea-surface

temperature (SST) in forecasting the seasonal distribution of South Asian monsoon rainfall. First, an evolution-centric SST analysis is conducted in the global oceans using the extended-Empirical Orthogonal Function technique to uncover the recurrent modes of spatiotemporal variability and their potential inter-basin linkages. A statistical forecast model is next developed using these extracted modes of SST variability as predictors. Assessment of the forecasting system's long-term performance from reconstruction and hindcasting over an independent verification period demonstrates high forecast skill over core monsoon regions – the Indo-Gangetic Plain and southern peninsular India, indicating prospects for improved seasonal predictions. The influence of SSTs on the northeast winter monsoon is subsequently investigated, especially, its evolution, interannual variability and the El Niño–Southern Oscillation (ENSO) influence. Key findings from this study include evidence of increased rainfall over southeastern peninsular India and Sri Lanka (generated by an off-equatorial anticyclonic circulation centered over the Bay of Bengal) during El Niño winters.

This dissertation provides the *first quantitative assessment* of the potential predictability of summer monsoon rainfall anomalies – the maximum predictable summer rainfall signal (amount, distribution) over South Asia from prior SST information – at *various seasonal leads*, and notably, at *SST-mode resolution*. The improved skill of the SST-based statistical forecast establishes the bar – an evaluative benchmark – for the dynamical prediction of summer monsoon rainfall.

SEA-SURFACE TEMPERATURE BASED STATISTICAL PREDICTION OF THE SOUTH ASIAN SUMMER MONSOON RAINFALL DISTRIBUTION

by

Agniv Sengupta

Dissertation submitted to the Faculty of the Graduate School of the
University of Maryland, College Park, in partial fulfillment
of the requirements for the degree of
Doctor of Philosophy
2019

Advisory Committee:
Professor Sumant Nigam, Chair
Associate Research Professor Alfredo Ruiz-Barradas
Professor Eugenia Kalnay
Professor Da-Lin Zhang
Professor Sujay Kaushal, Dean's Representative

Dedication

This doctoral dissertation is dedicated

To my beloved mother and father,
whose constant support and encouragement enabled me to pursue my dreams,

To Sumant, my advisor,
who guided me towards my dreams,

To Dishary, for her support and sacrifice.

Acknowledgements

I would like to begin by thanking everyone whose encouragement and support helped me to pursue my dream that resulted in this doctoral thesis. First and foremost, I convey my deepest gratitude to my advisor, Prof. Sumant Nigam, for his guidance. I consider myself fortunate to be mentored by him over the course of my graduate study at the University of Maryland, an experience that I will cherish forever. I have learned great virtues working with Prof. Nigam — patience, positive attitude, scientific vision, attention to minute detail. He has always been very supportive as an advisor and I sincerely thank him for numerous hands-on concept development sessions, encouragement and refinement of my research ideas. I take this opportunity to express my profound gratitude to Dr. Alfredo Ruiz-Barradas for his selfless support with datasets, analysis tools and methods. His valuable technical guidance, often sacrificing time from his own research, was instrumental to the successful completion of my thesis. I would like to thank Prof. Eugenia Kalnay and Prof. Da-Lin Zhang for taking the time to serve on my dissertation defense committee and for their insightful comments and helpful suggestions during the prospectus. Thank you to Prof. Sujay Kaushal for serving as the Dean's Representative on my committee.

I am indebted to the wonderful staff members of the AOSC department, especially, Tammy Hendershot, Bernadette Gatewood, and June Sherer, for their constant support, and, Jeff Henrikson for providing computational support. I greatly appreciate the support I received from my amazing fellow grad students. They have contributed in their own unique way to my grad school experience, which has fostered

my growth both as a researcher and as a person. In particular, I am grateful to the incoming class of fall 2014 and my officemates for their support and friendship.

As an undergraduate student, I have had the privilege of being guided by excellent mentors: Dr. Madhavan Rajeevan (MoES India), Prof. Subimal Ghosh and Prof. Subhankar Karmakar (IIT Bombay), Prof. Sumit Biswas, Prof. Shibnath Chakraborty and Prof. Somnath Ghosh (Jadavpur University). I am thankful to them for introducing me to research and for encouraging me to pursue a doctoral degree.

I am grateful for the unconditional love, unwavering support, and affection of my parents. Mom and Dad, thank you for all the sacrifices you have made in shaping my career. I would like to take this opportunity to thank my lovely fiancé, Dishary, for her support, sacrifice and encouragement. I express my deep gratitude to my two cousins living in Maryland—Suman Dasgupta and Soumyadip Sengupta. Without their support and inspiration, the Ph.D. journey living so far away from home would have been extremely difficult. I am thankful to my friends at the University of Maryland, especially the ones from the Graduate Hills apartment community, for being with me and helping me through this journey.

Finally, I would like to thank India's National Monsoon Mission for supporting my doctoral study and research. I also gratefully acknowledge the support from the University of Maryland Graduate School's Ann G. Wylie Dissertation Fellowship during my final semester.

Table of Contents

List of Tables

List of Figures

List of Abbreviations

AMO	Atlantic Multidecadal Oscillation
AR5	Fifth Assessment Report
CFS	Climate Forecast System
CMIP	Coupled Model Intercomparison Project
CRU	Climate Research Unit
DJF	December, January and February
EAWM	East Asian Winter Monsoon
ECMWF	European Centre for Medium-Range Weather Forecasts
EEOF	Extended Empirical Orthogonal Function
ENSO	El Niño–Southern Oscillation
FR	Fish Recruitment
GCM	General Circulation Model
GFDL	Geophysical Fluid Dynamics Laboratory
GPCC	Global Precipitation Climatology Centre
HadISST	Hadley Centre sea Ice and Sea Surface Temperature dataset
ICES	International Council for the Exploration of the Sea
IGY	International Geophysical Year
IMD	India Meteorological Department
IPCC	Intergovernmental Panel on Climate Change
IPHC	International Pacific Halibut Commission
JJA	June, July and August
JJAS	June, July, August, and September

LF-NAO	Low-Frequency North Atlantic Oscillation
LOESS	Locally Estimated Scatterplot Smoothing
MJO	Madden–Julian Oscillation
MPI	Max Planck Institute
MSLP	Mean Sea Level Pressure
NCAR	National Center for Atmospheric Research
NCEP	National Centers for Environmental Prediction
NEFSC	Northeast Fisheries Science Center
NEM	Northeast Monsoon
NOAA	National Oceanic and Atmospheric Administration
NPGO	North Pacific Gyre Oscillation
OND	October, November and December
PC	Principal Component
PDO	Pacific Decadal Oscillation
PDV-NP	North Pacific decadal variability
PDV-PP	Pan-Pacific decadal variability
RMM	Real-time Multivariate MJO Index
SD	Standard Deviation
SEDAR	Southeast Data, Assessment, and Review
SPNA	Sub-Polar North Atlantic
SST	Sea Surface Temperature
TRMM	Tropical Rainfall Measuring Mission
UKMO	United Kingdom Met Office

Chapter 1: Introduction

1.1 Background

Monsoons over South Asia are characterized by a southwest summer monsoon from June to September (JJAS) and a northeast monsoon (NEM) from October to December (OND). The value of reliable, timely, and long-range predictions of summer monsoon rainfall cannot be overstated for the agriculture dominated economies of the Indian subcontinent (Gadgil and Gadgil 2006), where ~75% of annual rainfall arrives in the summer. Summer monsoon predictions have drawn considerable public/policy attention lately as South Asia becomes a resource stressed region: Rapid population and economic growth have led to significant land-use land-cover changes, heightened demand for freshwater and energy, degraded environment from aerosol and dust loadings, and increased GHG emissions. Regional hydroclimate (precipitation, surface air temperature, soil moisture, subsurface water) exhibits substantial – at times, precarious – trends in the post-1950s period (Kothawale and Rupa Kumar 2005; Bollasina et al. 2011; Turner and Annamalai 2012; Mishra et al. 2012; Dorigo et al. 2012; Krishnan et al. 2016). This environmental backdrop and the livelihood concerns and aspirations of a billion-plus people generate the demand for more accurate summer monsoon predictions, especially with longer lead times.

Seasonal predictability of climate is premised on the presence of influential system components with large thermal inertia, leading to longer timescale (vis-à-vis seasonal) variability. Upper oceans and the Himalayan cryosphere meet the criterion,

but reliable observational records exist only for the former albeit at the surface. SST is an influential variable, especially in the Tropics (Sikka 1980; Charney and Shukla 1981; Shukla and Paolino 1983; Rasmusson and Carpenter 1983; Kumar et al. 1999). It affects both regional and faraway climate through modulation of surface fluxes, convection and clouds, and moisture transports, among others. The influence is not one-way as SST responds to atmospheric circulation and near-surface meteorology. As such, SST of neighboring seas and faraway oceans are potential predictors of the variations of the southwest monsoon.

1.2 Dynamical and statistical monsoon prediction

Forecasting of the summer monsoon rainfall has been performed with both dynamical (for example, Manabe et al. 1974; Palmer et al. 1992; Chen and Yen 1994; Sperber and Palmer 1996; DelSole and Shukla 2012; Ramu et al. 2017) and statistical (for example, Thapliyal 1981; Shukla and Paolino 1983; Mooley et al. 1986; Shukla and Mooley 1987; Navone and Ceccatto 1994; Goswami 1996; DelSole and Shukla 2002; Sahai et al. 2003, 2008, Rajeevan et al. 2007) models.

Dynamical modeling has used atmospheric general circulation models (AGCMs) with prescribed SSTs as well as coupled atmosphere-ocean models (Krishnamurti et al. 2006). Dynamical models operate by approximating the physical processes of the atmosphere and the ocean. Dynamical seasonal forecasts are issued by several operational prediction centers, for example, the India Meteorological Department (IMD), the International Research Institute (IRI) at Columbia University, APEC Climate Center in South Korea, etc. These forecasts often utilize multi-model ensembles to remove the uncertainties associated with the spread of ensemble forecasts

with different initial conditions and the uncertainties resulting from different parameterization schemes (Krishnamurti et al. 1999; Kang and Shukla 2006). The ensemble members are forced by the same SST but initialized from slightly different atmospheric conditions (Dix and Hunt 1995; Kumar and Hoerling 1995; Kang et al. 2004). The simulation differences among the ensemble members are used to quantify the noise due to internal model dynamics, whereas, the relative similarity between ensemble members is considered as the atmospheric response to the external forcing. Subsequently, multi-model ensemble forecasts have been combined into a single forecast using the "superensemble" forecasting technique (Krishnamurti et al. 1999). The prediction skill of the multi-model superensemble has been demonstrated to be higher than individual members, thereby, signifying a major improvement over single-member models and the ensemble mean (Chakraborty and Krishnamurti 2006; Kumar and Krishnamurti 2012). Recent dynamical modeling studies (Yang et al. 2012; Saha et al. 2016; Pillai et al. 2018) have used SST information-based approaches to assess the predictability of the Asian summer monsoon in the Climate Forecast System (CFS) model. The skill of the SST indices — Niño 3, El Niño Modoki Index, equatorial East Indian Ocean anomaly — were assessed for prediction of the Indian summer monsoon rainfall in CFSv2 hindcasts.

Statistical models are trained using long-term observational data and often employ multiple regression approaches using several predictors, such as, an El Niño parameter; SST anomalies over the adjoining oceans; minimum temperature over central India and the eastern coast of India; Northern Hemisphere surface air temperature and zonal winds pattern at the 20-km height over India, the Southern

Oscillation index; the pressure tendency at Darwin on the El Niño–Southern Oscillation time scale; sea level pressure over Argentina; pressure gradient over western Europe; surface pressure anomaly over the Northern Hemisphere; pressure over equatorial Indian Ocean; and Himalayan and Eurasian snow cover (Kumar and Krishnamurti 2012). Sahai et al. (2003) introduced an empirical model for deterministic monsoon prediction using SST from different geographical locations at various temporal lags as predictors. A probabilistic monsoon forecast system using a large ensemble of empirical forecasts was presented in Sahai et al. (2008); the system demonstrated good skill in predicting the monsoon-related droughts of 2002 and 2004. Rajeevan et al. (2007) reported on the experimental statistical models developed at IMD for long-range monsoon forecasting. These statistical models were developed from ensemble multiple linear regression and projection pursuit regression techniques.

1.3 Challenges in seasonal monsoon prediction

Prediction of seasonal summer monsoon rainfall distribution over South Asia, however, remains challenging (Krishnamurti et al. 1999; Gadgil et al. 2005; Krishnamurti and Kumar 2012). The prediction skill has remained marginal and stagnant for several decades despite advances in the representation of physical processes (including ocean-atmosphere coupling, moist convection, aerosol/dust effects), numerical model resolution, data assimilation techniques, and the range of assimilated variables. The major challenges in seasonal monsoon prediction are summarized below:

a) *A challenging physical domain*: The representation of complex orography, land-surface types, and land-ocean boundaries of the Indian subcontinent is a

modeling challenge. Ruiz-Barradas and Nigam 2005, 2010 suggest that current climate models have poor skill in simulating and predicting seasonal summer rainfall even over even the Great Plains – a region devoid of the terrain and coastline challenges presented by South Asia.

b) *A difficult season for hydroclimate prediction — summer*: There is growing evidence that summer season simulations and predictions are more challenging than winter ones, in part, because land-atmosphere interaction (including evapotranspiration) is very active in summer but muted in winter (energy limited). Its deficient representation in models is thus more consequential in summer, distorting regional atmospheric and terrestrial water cycles, and thus hydroclimate.

c) *Model simulation of the key climate processes and feedbacks*: The low seasonal predictability of dynamical models is due to their sub-optimal simulation of the mean rainfall distribution over the South Asian monsoon region (Waliser et al. 2003) and the atmospheric response to SST forcing (Kang et al. 2004). While the representation of ocean-atmosphere interaction is considered essential in predictive models (Krishna Kumar et al. 2005), its representation in current models is sub-par (Bollasina and Nigam 2009, hereafter BN2009; Rajeevan et al. 2012). For instance, BN2009 showed that coupled climate simulations exhibit large systematic biases in precipitation, evaporation, and SST in the Indian Ocean, often exceeding 50% of their climatological values. Many of the biases were common across several model simulations. Representation of air-sea interaction was also found compromised as coupled models emphasized

local forcing in the Indian Ocean (e.g., large precipitation–SST correlations), at odds with the weak local links in observations.

d) *Challenges in assimilating ocean-atmosphere data in a coupled modeling framework*: Attribution of low predictive skill (or prediction errors) invariably involves discussion of the relative contribution of data assimilation errors and model simulation deficiencies, especially in case of seasonal forecasts. This dissertation emphasizes the potential benefits of initializing the coupled model by the projection of the initial state on SST and circulation variability structures obtained using an evolution-centric analysis strategy (e.g., extended-EOFs).

e) The *potential predictability of the South Asian summer monsoon rainfall* (from SST, for example) is yet to be ascertained from observational analysis, motivating this dissertation work. Model-based assessments of monsoon predictability exist, but they can hardly be considered definitive given the large systematic biases in monsoon hydroclimate and distorted representation of ocean-atmosphere interaction in the Indo-Pacific basin.

1.4 Objectives

The primary research objectives of this dissertation are as follows:

- Assess the *SST-monsoon rainfall linkage* from innovative spatiotemporal analyses of 20th–21st century SST and precipitation observations.
- Determine the *SST-based potential predictability* of summer monsoon rainfall from seasonal rainfall reconstruction. Reconstruction will be undertaken with both *contemporaneous* and *SST-leading* precipitation regressions of the principal modes of SST variability, i.e., at modal resolution. This strategy will help provide

a *quantitative assessment* of the *potential predictability* of summer monsoon rainfall from the individual SST modes at various seasonal leads.

- Quantify the *realized predictability* from monsoon rainfall hindcasts in an independent period.
- Generate *experimental forecasts* of seasonal summer monsoon rainfall distribution over South Asia.

1.5 Dissertation outline

This dissertation is structured as: Chapter 2 presents an evolution-centric analysis of SST variability in the global oceans (northward of 20°S) to uncover potential inter-basin links among the recurrent modes of spatiotemporal variability. An array of sensitivity and mode-physicality tests based on analogs and fish recruitment data underpin the analysis' robustness. The focus here is on the space-time structure of multidecadal SST variability, especially its rendition in a spatiotemporal analysis that has no *a priori* basin preference. Chapter 3 investigates the potential predictability of seasonal summer monsoon rainfall over South Asia from a statistical model that uses the extracted modes of SST variability (obtained in Chapter 2) in the Pacific, Atlantic and Indian Ocean basins as predictors. The model allows the reconstruction and hindcasting of observed rainfall anomalies from both *contemporaneous* and *SST-leading* regressions of summer rainfall on the leading modes of SST variability. This technique ensures the integration of the influence of the full spectrum of SST variability on regional rainfall. Chapter 4 focuses on the northeast monsoon (NEM), which has received considerably less research attention than its summer monsoon counterpart. The observational analysis documented here characterizes the NEM's climatological

evolution at a monthly resolution, its interannual variability, long-term trend, the influence of ENSO on NEM and investigates the associated mechanism. Chapter 5 provides a summary and discussion of results, and outlines related future research prospects.

Chapter 2: An Evolution-centric Analysis of Observed SST Variability Factoring for Atlantic–Pacific Inter-Basin Links

2.1 Introduction

Sea surface temperature exerts a significant, and often predictable, influence on Earth's climate. Interannual SST variations related to El Nino Southern Oscillation (ENSO), for instance, impact the Indian summer monsoon to the west (Rasmusson and Carpenter 1983) and the North American hydroclimate to the east (e.g., Ropelewski and Halpert 1987; Joseph and Nigam 2006). Decadal SST variations have been implicated in notable hydroclimate episodes, such as multi-year droughts and drying: The 1930s 'Dust Bowl' drought over the Great Plains of North America has been linked to decadal SST variability in the Pacific (e.g., Ting and Wang 1997; Nigam et al. 1999; McCabe et al. 2004; Seager et al. 2005; Nigam et al. 2011) and the Atlantic (e.g., Namias 1966; McCabe et al. 2004, 2006; Ruiz-Barradas and Nigam 2005; Nigam et al. 2011). The 1950s-1980s 'drying' of the Sahel has also been attributed to long-lived tropical and extratropical SST variations (Folland et al. 1986; Giannini et al. 2003; Zhang and Delworth 2006; Nigam and Ruiz-Barradas 2016; Thomas and Nigam 2018). SSTs influence regional and remote climate via modulation of surface fluxes, convection and clouds, atmospheric circulations, and heat and moisture transports.

Regional hydroclimate predictions can as such benefit from the improved characterization of the nascent and mature phases (i.e., evolution) of the recurrent, pertinent interannual and decadal SST variations – a key goal of this analysis. Coherent large-scale SST anomalies on interannual-to-multidecadal timescales result not only from ocean wave dynamics (as in, but not limited to, tropical basins) and the overlying atmospheric circulation and related surface energy fluxes (as in extratropical basins; Frankignoul and Hasselmann 1977; DeCoetlogon and Frankignoul 2003; Deser et al. 2003; Deser et al. 2010), but also from heat transports by ocean currents and coastal and equatorial upwelling. Large-scale SST anomalies in one basin can moreover impact SSTs in the other basins through the atmospheric bridge (e.g., Alexander et al. 2002; Liu and Alexander 2007), thwarting efforts to unravel regional vs. remote contributions in SST evolution.

Evolution-centric analysis of recurrent SST variability has been undertaken in the Pacific (Guan and Nigam 2008, hereafter GN2008) and Atlantic (Guan and Nigam 2009, hereafter GN2009) basins, but seldom in both basins together, i.e., without a priori specification of basin preference. While conducting such analysis is the preeminent goal of this study as it can reveal lead-lag links between the basins in the context of each variability mode, inter-basin links have been studied before albeit in a piecemeal manner, and especially in the context of ENSO.

The impact of ENSO on the tropical Atlantic (e.g., Enfield and Mayer 1997; Hameed et al. 1993; Chung et al. 2002; Alexander et al. 2002) or of the Atlantic Niño on ENSO (e.g., Ham et al. 2013), or of these both on regional climate (Wang 2006) have been studied; the latter via changes in Walker circulation; see Liu and Alexander

(2007) for an overview. On multidecadal timescales, Chafik et al. (2016) indicated a prominent role of the Sub-Polar North Atlantic (SPNA) in fostering Atlantic-Pacific interaction through propagation of heat anomalies from the Gulf Stream region to SPNA, which impact the Atlantic-Pacific SST gradient, generating decadal variability in Pacific SSTs. Park et al. (2019) recently showed that anomalous warming of the Atlantic warm pool can generate a westward propagating atmospheric response that can suppress precipitation in the subtropical North Pacific, leading to the development of the Pacific meridional mode. Tropical Indo-Pacific SSTs, on the other hand, have been found influential in generating low-frequency SST variability in the North Atlantic (Hoerling et al. 2001; Bader and Latif 2003). Atlantic pacemaker experiments of Sun et al. (2017) show AMO to be teleconnected with decadal variability in the western tropical Pacific. On longer timescales, the recent warming trend in tropical Atlantic SST has been associated with intensification of the Walker circulation and related eastern Pacific cooling (Chikamoto et al. 2012; McGregor et al. 2014; Li et al. 2015).

The modes of decadal-multidecadal SST variability in the Atlantic and Pacific basins, especially, the inter-basin interactions in their evolution are the principal targets of this analysis. The modes themselves, i.e., their mature phase structure are reasonably well known. The decades-long anomalous conditions in the extratropical Pacific since 1976/77 (Nitta and Yamada 1989) and the linking of this oceanic state to variations of marine ecosystems in the northern basin (Mantua et al. 1997) and the hydroclimate of North America (Ting and Wang 1997; Nigam et al. 1999) highlighted the importance of decadal SST variability in the Pacific basin. Likewise, multidecadal SST variability

in the Atlantic basin, e.g., the AMO, is linked with notable hydroclimate anomalies – decadal droughts over North America (Nigam et al. 2011) and multidecadal drying of the Sahel (Thomas and Nigam 2018) – and decadal variations in Atlantic tropical cyclone counts (Nigam and Guan 2011), among others.

The origin of multidecadal variability in the North Atlantic is being actively investigated. The role of oceanic processes, especially heat transports through modulation of Atlantic Meridional Overturning Circulation (e.g., Delworth et al. 1993; Knight et al. 2005; Latif and Keenlyside 2011) is being assessed relative to atmospheric forcing through surface fluxes, both aerosol-influenced radiative fluxes (e.g., Booth et al. 2012) and stochastic heat flux variations (Clement et al. 2015). Zhang et al. (2013, 2016), Zhang (2017), Delworth et al. (2017), O'Reilly et al. (2016), Drews and Greatbatch (2016) and others have stressed the importance of ocean circulation in the generation of multidecadal variability. Decadal fluctuations in the SPNA salinity and heat-content have recently been shown to result from a process sequence involving surface flux forcing, coastal upwelling, Ekman transports, ocean circulation, and bathymetric influences (Nigam et al. 2018).

The SST variability is analyzed in this study using the extended empirical orthogonal function (extended-EOF) technique which extracts variability modes based on both spatial and temporal recurrence, and without the imposition of any periodicity constraints and pre-processing of data. As such, it is able to depict the evolution of recurrent variability, unlike canonical EOF analysis which only identifies the mature-

phase spatial structure, i.e., the pattern (and not mode) of variability.[1] The technique yields characterization of secular warming (through a nonstationary secular trend) and multidecadal natural variability, contextually, i.e., from the same single analysis, as opposed to the more common residual estimation of either component; a contextual separation is deemed essential for detection and attribution of climate change. Unlike Guan and Nigam (2008, 2009), the present analysis pursues contextual characterization of multidecadal SST variability also in the basin realm, i.e., without prejudicing the analysis with an *a priori* basin preference – the case earlier, as GN2008 analyzed Pacific basin variability while GN2009 analyzed the Pacific-unrelated variability in the Atlantic basin. In addition to allowing full expression of inter-basin links through a global analysis domain (20°S-80°N), the present analysis is based on 15 additional years of recent data than GN2008, as it targets the 1900-2018 SST record.

The physicality of multidecadal modes is assessed using Pacific and Atlantic fish recruitment data as well as observational analog counts. The Pacific recruitment records have been augmented relative to GN2008 and Atlantic marine records sourced for physicality assessment – the latter used, perhaps, for the first time. Sensitivity tests, e.g., varying the temporal sampling window-width and the number of rotated modes, are performed to assess the robustness of the final analysis.

[1] Prior analyses of global SST variability used the EOF technique after pre-processing the SST record through time-series normalization (Kawamura 1994), low-pass filtering (Enfield and Mestas-Nuñez 1999), mode rotation (Mestas-Nuñez and Enfield 1999), and separation of seasons (Yasunaka and Hanawa 2005); no pre-processing was used in Messié and Chavez (2011). Chen et al. (2017) used pairwise rotation of EOFs to eliminate mode mixing. The present analysis uses the extended-EOF technique (Weare and Nasstrom 1982), followed by Varimax rotation (Kaiser 1958); see GN2008 and GN2009 for elaboration on the relative advantages of this strategy.

The datasets and analysis method are briefly described below in section 2.2. The principal components and modal evolution from the primary analysis – the rotated extended-EOFs of the seasonal SST anomalies in the 118-year period extending from January 1900 to February 2018 – are discussed in sections 2.3 and 2.4, where the focus is on decadal-multidecadal variability; modal links with ocean subsurface temperature and salinity are documented in section 2.4. Intra and inter-basin links between multidecadal modes, extracted from lead-lag analysis and supported by spatiotemporal evolution, are presented in section 2.5, with a brief commentary on related atmospheric circulation – a key linking agent. The sensitivity of the primary analysis and the physicality of extracted modes is discussed in section 2.6, with concluding remarks following in section 2.7.

2.2 Datasets and analysis method

2.2.1 Sea surface temperature

The UK Met Office's Hadley Centre Sea Ice and Sea Surface Temperature data (HadISST 1.1; Rayner et al. 2003), available monthly from 1900 to 2018 on a 1º grid, is analyzed. For computational efficiency, monthly SSTs are re-gridded onto a 5º by 2.5º longitude-latitude grid. Seasonal SSTs are computed using Northern Hemisphere season definitions, e.g., winter is the December-February average. Seasonal SST anomalies are constructed by removing the long-term climatology of each season. The same procedure is used for other variables in the study.

2.2.2 Mean sea level pressure

The UK Met Office's Hadley mean sea level pressure data (HadSLP2; Allan and Ansell 2006) is used to infer the surface atmospheric circulation associated with SST evolution. The dataset, a combination of land and marine pressure observations, is available at monthly resolution on a 5° global grid from 1850 to the present.

2.2.3 Subsurface temperature and salinity

The UK Met Office's Hadley Centre-produced quality controlled EN4.2.1 dataset (Good et al. 2013) which was bias-corrected using the climatological World Ocean Atlas 2009 (Levitus et al. 2009) is used for the analysis of ocean subsurface temperature and salinity. The data is available at monthly resolution on a 1° grid from 1900 to the present.

2.2.4 Analysis method

Seasonal SST anomalies in a global domain (20ºS–80ºN, 0º–360º) are analyzed for the period winter 1900 – winter 2017/18 using the extended-EOF technique (Weare and Nasstrom 1982). A 5-season-long sampling window is used in the primary analysis, followed by Varimax rotation (Kaiser 1958; Richman 1986) of the 11-leading principal components (PCs). North et al.'s (1982) 'rule of thumb' was used to identify the number of PCs to be rotated. Because of the focus on both spatial and temporal recurrence, the analysis yields recurrent modes (not patterns) of variability; specifically, a 5-season-long spatiotemporal pattern (loading vector, or extended-EOF) and its related time series (principal component) are obtained for each variability mode.

The SST principal components are smoothed, when noted, using the LOESS filter (Cleveland and Loader 1996) with a 10% span window (LOESS-10%; or with window-span equaling 10% of the 118-year record, or ~12 years). The smoothing suppresses seasonal-to-interannual variations, thereby highlighting decadal-multidecadal variability.

The evolution of SST (and other related variables) can be obtained from the linear lead-lag regressions of their seasonal anomalies on the principal components – smoothed or unsmoothed. Note, linear regressions of SST on any PC in the ± 2 season window completely recover the related SST loading vector that was initially obtained. Standard statistical tools such as autocorrelation and cross-correlation are used to estimate modal timescale and inter-modal links, respectively.

2.2.5 Physicality of multidecadal variability modes

Hare and Mantua's (2000) pioneering use of marine ecosystem data in evaluating the physicality of the statistically extracted mode of multidecadal SST variability in the extratropical basin (PDO) opened a new avenue in physicality assessment – one pursued by Guan and Nigam (2008) who also used observational analog counts. North Pacific and the Bering Sea recruitment is assembled from Hare and Mantua (2000; data period 1965-1997), International Pacific Halibut Commission (IPHC) regulatory areas 3B and 4A[2] catchment (data period 1991–2014), and from two IPHC models (Stewart and Martell 2014) for the more extended period (1925–2010). For the Atlantic basin, stock assessment records for *mackerel* (NEFSC 1996; NEFSC

[2] The IPHC regulatory areas are described in their Technical Report No. 49 (Kong et al. 2004).

2006; NEFSC 2018), *Gulf of Maine cod* (Palmer 2014), *menhaden* (SEDAR 2015), and the *Norwegian herring* (Toresen and Østvedt 2000 and ICES 2011) were used in physicality assessment of the Atlantic basin modes.

As the observational realization of a statistically extracted mode is the ultimate proof of its physicality, the observed SST anomalies were objectively scanned to detect instances when they closely resembled any one of the leading modes; an observational analog was recorded when this occurred and the total analog count was an evaluative metric for the physicality of modes; see GN2008 for how resemblance was objectively assessed.

An array of sensitivity tests and mode-physicality assessments lead to the choice of the five-season-wide sampling window and the rotation of eleven leading modes in the 20°S-80°N basin for the primary analysis.

2.3 Spatiotemporal analysis of SST variability – Pacific decadal variability

The section begins with the display of principal components (PCs) of all the 11 variability modes (Fig. 2.1) extracted from the primary analysis. Both the originally extracted PCs and their LOESS-10% smoothed versions are shown, along with and in the order of explained variance; the full name and the corresponding abbreviated label are also noted. The modes of decadal SST variability in the Pacific basin are presented in this section.[3] Pacific decadal variability (PDV) is represented by two modes in this analysis, as in GN2008: the Pan-Pacific (4^{th}-leading) and North Pacific (7^{th}-leading)

[3] The interannual ones (including ENSO) and the Secular Trend mode, characterized in GN2008, are not the primary focus of this study and hence not discussed here.

modes; the more familiar North Pacific mode is discussed first. Modal evolution over a 5-year period is shown in Fig. 2.2.

2.3.1 North Pacific mode (PDV-NP)

The mature phase of the North Pacific mode (Deser and Blackmon 1995; Nigam et al. 1999; Barlow et al. 2001; GN2008) consists of a zonal band of warm SST anomalies (~0.3 K) extending from the coast of Japan into the central-eastern mid-latitude Pacific, and negligible anomalies elsewhere (cf. Fig. 2.2, right column, *t*). The 1-year precursor phase, however, is more populated, with cold anomalies additionally present in the central-eastern equatorial Pacific, i.e., in the cold-tongue domain (e.g., marked in Nigam and Chao 1996). PDV-NP's evolution is very similar to that displayed in GN2008 (Fig. 12, left column) and the depicted 5-year evolution is a, but a snapshot given the mode's multidecadal timescale (estimated later in this section). The mode has more extensive links to the Tropics than evident from the displayed regressions: PDV-NP's links to the southern Indian Ocean and western Pacific become apparent when SST correlations are plotted (Fig. 2.3a) as, unlike regressions, correlations are not adversely impacted by the small amplitude of variability in these regions. PDV's link with the tropical Indian basin has been noted earlier (Deser et al. 2004; GN2008, their Fig. 12).

The PDV-NP mode closely resembles Mantua et al.'s (1997) Pacific Decadal Oscillation (PDO), as noted in GN2008. The PDV-NP PC and PDO index are maximally correlated when PDV-NP lags PDO: at −0.56 at 2-season lag for the unsmoothed versions, and at −0.79 at 1-year lag with the smoothed counterparts (Fig. 2.3b). The negative correlations indicate that PDV-NP's positive phase (displayed in

Fig. 2.2) corresponds to PDO's negative phase. Both capture the 1976/77 shift to a colder Pacific surface state. The PDV-NP and PDO exhibit subtle differences, the above similarities notwithstanding, notably from the extension of PDO's coastal footprints into the Gulf of Alaska (Fig. 2a in Mantua et al. 1997; and Fig. 2.3a here) – a feature not present in the evolution depicted in Fig. 2.2 (right column).

2.3.2 Pan-Pacific mode (PDV-PP)

The Pan-Pacific mode's mature phase (Fig. 2.2; left column, *t*) consists of warm SSTs along the North American coast extending from the Aleutians to Baja California and then southwestward into the central tropical Pacific; the horseshoe structure surrounds weaker cold SSTs in the central mid-latitude basin. The mode was first documented by GN2008 (Fig. 11, left column). Its PC (Fig. 2.1) indicates a multidecadal transition in the 1930s to a warmer coastal state which ended in the 1990s. Its cold phase since the early 2000s, notably, around 2010, and the following transition to the warm phase in ~2013 is relevant in the context of the warm "blob" of water that persisted in the northeastern Pacific for a few years since 2013 (Bond et al. 2015). In recent decades, since at least 2000, the PDV-PP mode has been more energetic than the PDV-NP one.

The Pan-Pacific mode's SST anomalies are similar to the horseshoe-shaped, coastally-focused SSTs associated with the North Pacific Gyre Oscillation (NPGO; Di Lorenzo et al. 2008, Fig. 4b) – the 2nd leading EOF of the modeled sea surface height variations in the extratropical basin. Despite this similarity, connections between the two have, surprisingly, remained uninvestigated. The similarity is stronger in the SST regressions of the common period (1950-2017), as shown in Fig. 2.4a. The extensive

correspondence between the regressions of upper-ocean (5-657m) heat content and salinity on the Pan-Pacific PC and the NPGO index in their common period (cf. Fig. 2.4a) also underpins the close link between the Pan-Pacific mode and the NPGO. Temporally, the Pan-Pacific PC and the NPGO index links are less impressive: The two are found to be maximally correlated at 2-season lag (with the PDV-PP leading), at −0.56 using unsmoothed time series and at −0.69 using their smoothed counterparts in their common 1950-2017 period.

The PDO and NPGO indices are simultaneously correlated at −0.18; their smoothed versions at −0.30. The PDV-NP and PDV-PP principal components are however uncorrelated, as mandated by the extended-EOF analysis, including subsequent PC rotation. Smoothing destroys, to an extent, the strict orthonormality of the PCs; their smoothed versions are simultaneously correlated at −0.01. The PDV-NP and PDV-PP modal structures thus constitute an optimal basis for resolving decadal SST variations in the Pacific basin. Principal component correlations with Pacific marine ecosystem data, including fish recruitment (discussed later in section 2.6), support this assessment.

2.3.3 Variability timescale

The autocorrelation structure of the LOESS-10% smoothed PDV PCs and the equivalently smoothed PDO and NPGO indices are examined in Fig. 2.5a to estimate the variability timescales. For periodic variations, the oscillation period is twice the temporal distance between the zero-crossings of the autocorrelation. Autocorrelation of the PDV-NP and PDO are similar, with no secondary peaks and nearly coincident zero-crossings at ~13 years, i.e., a variability timescale of 50-55 years. In contrast, the

autocorrelation of the PDV-PP exhibits wings, i.e., a non-monotonic decrease with increasing lead-lag, confounding timescale estimation; consideration of the zero-crossings alone yields a ~50-year timescale for the PDV-PP mode. Autocorrelation is also computed for the NPGO and compared with the PDV-PP's in the common period (1950-2017). The comparison reveals reasonably similar zero-crossings, the first of which occurs much earlier than in PDV-PP's full-period (118-year) autocorrelation (thick red line), indicating an estimation bias towards shorter timescales in the shorter period (68-year) analysis.

Quantitative estimation of variability timescales is accorded by the power spectra of the unsmoothed time series (Fig. 2.5b). PDV-NP and PDO exhibit similar spectra – with a primary peak at 55-60 years and secondary peaks at 35-40 and 20-30 years – representing multidecadal periods; with the PDV-NP having more power at nearly all periods. The PDV-PP and NPGO, however, exhibit notable differences: NPGO's primary peak is at 10-15 years while PDV-PP's is at 25-30 (and 15-20 and 55-60) years, with the PDV-PP having more power at longer periods (i.e., lower frequencies). Although wings in the autocorrelation indicate the presence of multiple timescales in PDV variability, some of the shorter periods identified from power spectra were not estimable from the autocorrelation structure as the latter was based on the smoothed time series.

2.4 Spatiotemporal analysis of SST variability – Atlantic multidecadal variability

Multidecadal SST variability in the Atlantic basin consists of at least two modes of variability: Atlantic Multidecadal Oscillation (AMO; Enfield et al. 2001; GN2009; Kavvada et al. 2013; Ruiz-Barradas et al. 2013; Nigam et al. 2018), with warm footprints in the subpolar-to-subtropical basins in its positive phase and an approximate 7-decade timescale (cf. Fig. 2.1). The second is the Low-Frequency North Atlantic Oscillation (LF-NAO), a decadal-multidecadal variability mode known variously for over half a century (Bjerknes 1964; Rogers 1984; Hurrell 1995; Joyce et al. 2000; Marshall et al. 2001; Nigam 2003; Czaja et al. 2003; Zhang and Vallis 2006; Hurrell et al. 2006; Alvarez-Garcia et al. 2008; GN2009; Gastineau and Frankignoul 2015; Nigam et al. 2018; and others). It consists of tri-polar SST anomaly in the North Atlantic, with warm anomalies off Newfoundland and southwest-to-northeast sloping cold anomalies in the subtropical and northeastern basins in its positive phase. The AMO (5^{th}-leading) and LF-NAO (10^{th}-leading) modal evolution are shown in Fig. 2.6.

2.4.1 Atlantic Multidecadal Oscillation (AMO)

A development phase of the AMO is depicted in Fig. 2.6 (left column). A 10-year evolution of SST anomalies at 2-year intervals shows the pre-mature phase ($t-4$ years) to consist of notable anomalies in the subpolar basin, with a focus in the Labrador and Irminger Seas. Two years later ($t-2$ years), warm SSTs are found along the western flank of the subpolar gyre, continuing southward along the Grand Banks. The southeastward extension of warm SSTs at this time and their rapid development

towards and along the African coast in the next two years suggest entrainment of the warm subpolar SST anomalies into the subtropical gyre, and their anticyclonic development hence. In the mature phase (*t*) of the AMO, the entire North Atlantic, but for the Sargasso Sea, is warm; SST anomalies are ~0.4°C in the subpolar basin, with a weaker extension into the subtropics and the Tropics that bears resemblance to the Interhemispheric variability mode in the Atlantic (e.g., Ruiz-Barradas et al. 2000). The 10-year evolution (Fig. 2.6) – a short period in the context of this mode's multidecadal timescale – indicates a subpolar origin of the AMO SSTs followed by their southeastward advance and development in the North Atlantic basin, much as described in GN2009 (Fig. 4) and Kavvada et al. 2013 (Fig. 5); in short, the SST anomalies do not develop concurrently across the basin. The AMO is also not found linked to Pacific and Indian basin SSTs.

The AMO in this analysis closely resembles its earlier characterization: The NOAA-AMO index – based on the linearly-detrended, area-averaged SST anomaly in the North Atlantic basin (0°-60°N, 75°-5°W), following Enfield et al. (2001), and plotted in Nigam et al. (2018, Fig. 1) – is correlated with the AMO principal component at 0.69 during 1900-2017, and at 0.80 when both are smoothed (LOESS-10%) over the same period. The AMO PC and index track closely, capturing the constituent decadal pulses (Nigam et al. 2018) and the multidecadal warm-to-cold basin transition in the mid-1960s and the reverse transition in the mid-1990s; both PC and the index have increased since the mid-1970s.

The SLP regressions on the AMO PC, contoured in blue in Fig. 2.6, show lower SLP in the polar latitudes, with foci over the southern tip of Greenland and the East

Siberian Sea; the former, leading to enhanced westerlies over the subpolar gyre in the Atlantic. Interestingly, the underlying SSTs are warmer, i.e., opposite of what wind-speed driven intensification of surface fluxes would produce; suggesting other origins for this nascent AMO phase. In the mature phase, the meridional SLP gradient is reversed, leading to weakened westerlies and to underlying SST anomalies whose sign – positive – is, at least, consistent with the weakening of surface fluxes. The mechanism's viability, however, depends on more than just the sign: Is a 0.4°C warming of the subpolar gyre consistent with an ∂(SLP)/$\partial\theta$ increase of (0.4hPa)/(15°latitude)?[4] Notable SLP regressions in the post-mature phase (t+4 years) are found, interestingly, not in the North Atlantic but in the North Pacific, indicating potential inter-basin links – a topic pursued in the next section.

2.4.2 Low-Frequency North Atlantic Oscillation (LF-NAO)

A development phase of the LF-NAO is displayed in Fig. 2.6 (right column). Its name stems from its impressive SLP footprint over the North Atlantic – a meridional dipole with a low centered over the Denmark Strait (i.e., between southern tip of

[4] A perusal of Figure 1 in Deser et al. (2010) shows that a pressure difference of approximately 4.0-hPa over 15° of latitude is related to a ~0.4°C change in subpolar gyre temperature. This pressure difference is about 10-times larger than that in AMO's mature phase, and while this discrepancy can call into question the viability of the surface flux forcing mechanism for AMO's mature phase SSTs, one needs to take into account the larger variability timescale in AMO's case – multidecadal – vs. the subseasonal in Deser et al.'s NAO example (2010). For a passive mixed layer (of depth H), subject to periodic downward surface heat-flux forcing (F_{srf}), the thermodynamic response of mixed layer temperature (T) is $\hat{T} \approx -i\hat{F}_{srf}/(HC_p\omega)$, where T(t)=Real$\{\hat{T}e^{i\omega t}\}$ and F_{srf} is similarly represented. Although the equation governing mixed-layer temperature is more complex (cf. Deser et al. 2010, Eqn. 1), a simplified version is used here to highlight the concept of frequency modulation of forcing, i.e., the temperature response is proportional to the forcing amplitude divided by ω, the variability frequency. As ω associated with multidecadal timescales is much smaller than the one associated with subseasonal NAO variability in Deser et al., a realistic multidecadal SST response is, in principle, obtainable even with an order of magnitude smaller surface-flux forcing.

Greenland and Iceland) and an expansive high over the subtropical and midlatitude basin centered westward of Azores – which broadly resembles the NAO positive phase (e.g., Deser et al. 2010, Fig. 1). The two NAO index stations are marked in LF-NAO's mature phase (*t*) whose weak SST anomalies exhibit a triband structure, reminiscent of the NAO SST anomalies (Deser et al., Fig. 1); note, some differences are inevitable due to differences in dominant timescale (multidecadal here vs. subseasonal in Deser et al.) and seasonal stratification (all-season regressions in Fig. 2.6 vs. winter regressions in Deser et al.). The resemblance continues in the temporal domain, with the LF-NAO principal component maximally correlated with Hurrell's NAO index at 0.62 at 4-season lag (with LF-NAO lagging) when both PC and the index are smoothed (LOESS-10%) over the 1900-2017 period.

Unlike the AMO, the LF-NAO is associated with more impressive SLP than SST anomalies, reflecting, perhaps, a dominant role of atmospheric processes in its genesis and evolution. More interestingly, and also unlike the AMO, the LF-NAO is associated with significant SST and SLP anomalies in the Pacific, notably, in the midlatitude basin where a band of cold SSTs extends from the coast of Japan towards the North American coast (e.g., Fig. 2.6, right column, *t*+2 years); the related SLP regressions indicate that these cold SSTs underlie a belt of strengthened surface westerlies (as westerly anomalies are in the region of climatological westerlies). That the band of cold SSTs closely resembles the negative phase of the PDV-North Pacific mode (cf. Fig. 2.2, right column, *t*) is noteworthy, and suggestive of inter-basin interaction, which is investigated in the next section.

2.4.3 Variability timescale

The autocorrelation of the smoothed AMO and LF-NAO principal components (Fig. 2.7) is similarly structured with secondary peaks but their zero-crossings indicate a longer timescale (>80 years) of the LF-NAO mode vis-à-vis AMO (~70 years). The power spectrum (not shown) was of limited use in identifying the dominant periodicities at long periods because the spectrum resolution at low frequencies was limited by the shortness of the analyzed SST record (116 years), leading to a large void between its ultimate and penultimate periods (116 and 58 years, respectively). One can thus conclude only that AMO has more power at the 58-year than 116-year period; vice-versa for the LF-NAO. is noteworthy, and suggestive of inter-basin interaction, which is investigated in the next section.

2.4.4 Subsurface structure

The *subsurface* temperature and salinity extensions of the multidecadal modes of sea *surface* temperature variability – the AMO and LF-NAO – are shown in Fig. 2.8, which also documents, for reference, the corresponding features of the Pacific multidecadal modes. The subsurface structure is shown along transects that bisect key SST anomalies; the transects are marked on the mature-phase SST anomaly maps in the left panels.

The AMO transect goes through the subpolar gyre bisecting the largest SST anomaly, and extends, approximately, from Long Island to the southwest to Faroe Islands (between Iceland and Norway) to the northeast, while going through the Charlie Gibbs Fracture Zone (a Mid-Atlantic Ridge interruption allowing west-east basin connectivity) in the mid-basin. The AMO temperature and salinity anomalies exhibit

coherent, down-sloping structure indicating the gradual sinking of warm-salty anomalies up to a depth of ~1000 m as they head northeast along the transect. Interestingly, this transect is broadly coincident with the path of the North Atlantic Current which must steer the AMO anomalies; these anomalies, however, don't head out of the northeastern basin as they are entrained into the subpolar gyre (Nigam et al. 2018; see Fig. 4).

The transect in the LF-NAO case (Fig. 2.8, 2nd row) is the ~45°N latitude that cuts across the mid-basin SST anomalies, i.e., across the middle feature of the triband SST anomalies associated with this mode (cf. Fig. 2.6 and related discussion in section 2.4.2). Notable subsurface anomalies (warm and salty) are present in the western basin, confined to the near-coastal region along the Grand Banks. These anomalies represent northward excursion of the Gulf Stream which typically follows the positive mature phase of the LF-NAO, with an ~1-year lag. Such meridional excursions of the Gulf Stream on decadal timescales and their lead-lag relationship with the LF-NAO and AMO's decadal pulses were analyzed by Nigam et al. (2018).[5] The cold-fresh water in the upper layers (0-200m) just east of the Grand Banks represents leakage of subpolar water through the Newfoundland basin (see Fig. 4, the third column in Nigam et al. 2018) – an intensified Labrador current. The warm-salty anomalies further to the east originate from the Gulf Stream excursion and its sectional detachment (see Nigam et al. 2018 for more details).

[5] Note, the LOESS-10 smoothed SST PCs (Fig. 2.1, black lines) fully retain the notable decadal pulses present in the raw PCs, and as such, regressions on the smoothed PCs (e.g., Fig. 2.8) represent, primarily, the structure of decadal variability.

The subsurface temperature and salinity anomalies associated with the Pacific modes (Fig. 2.8, bottom rows) do not extend as deeply as the Atlantic ones. The ones related to the PDV-Pan Pacific mode are confined only to the upper layers (0-200m), likely from this mode's transect being limited to the tropics-subtropics. The temperature-salinity combination (warm-salty) and the modest subsurface reach of the anomalies off Baja California indicate anomalous downwelling as the origin. Southwestward towards the equator (and Inter-Tropical Convergence Zone in the central Pacific), the upper layer anomalies are essentially cold and fresh but for the very thin warm layer near the surface. More coherent and deeply extended (up to ~500m) subsurface anomalies are found along the transect bisecting the key feature of the PDV-NP mode – the warm SST anomalies in the midlatitude basin. The warm-salty anomalies in the central basin with the largest amplitude in the-near surface layers and the cold-fresh anomalies in the near-coastal sector in the eastern basin are consistent with the impact of anomalous anticyclonic atmospheric flow on the underlying ocean. Such circulation would lead to diminished westerlies in the mid-basin, reducing heat and moisture fluxes (loss) from the ocean surface, while the related northerlies along the US West Coast would result in increased upwelling. The next section on inter-basin links documents the sea-level pressure distribution during PDV-NP evolution and corroborates the above discussion.

2.5 Link between multidecadal modes: intra-basin & inter-basin linkages

Links between the multidecadal SST variability modes are investigated in this section. As the modes are obtained from an extended-EOF analysis, the principal

components are orthonormal.[6] All modes, including multidecadal ones, are thus unrelated from the PC correlation perspective. The *simultaneous* correlation – mandated to be zero by the analysis technique – is however an incomplete measure of linkage, whose assessment requires additional evaluation of the *lead-lag* correlations. These are documented in this section, beginning with the intra-basin ones.

2.5.1 Intra-basin links

Lead-lag correlations between the AMO and LF-NAO PCs are displayed in Fig. 2.9 (blue curve). While the smoothed PCs are essentially uncorrelated at zero-lag, retaining the property of the unsmoothed PCs (cf. Footnote 5), the AMO lags the LF-NAO by ~6.5 years, and more robustly by ~16 years when the lag correlation is as large as 0.70. The two peaks in the lead-lag correlation structure arise from the presence of decadal and multidecadal variability components. The ~6.5-year lag of the AMO vis-à-vis LF-NAO was noted also in Nigam et al. (2018) where decadal fluctuations of the subpolar gyre were of interest and zeroed on through regressions on the AMO-index-*tendency* rather than the index itself. The longer AMO-lag (~16 years) is of considerable interest in the context of multidecadal evolution of Atlantic SSTs and elaborated on after noting the significant lead/lag links of the AMO and LF-NAO relative to Pacific multidecadal variability.

[6] Rotation of the principal components (PCs) – performed in this analysis – destroys the spatial orthogonality of the related loading vectors (i.e., extended-EOFs) but leaves intact the temporal orthogonality of the PCs. The smoothed (LOESS-10%) PCs also remain approximately orthonormal, e.g., the smoothed PDV-NP and PDV-PP PCs are simultaneously correlated at −0.01.

2.5.2 Inter-basin links

Lead-lag links between the key Atlantic and Pacific multidecadal modes are documented in Fig. 2.9: PDV-NP (or PDO's *–ve* phase) leads the negative phase of LF-NAO by ~6.5 years (red) while AMO leads PDV-NP by ~12.5 years (black), with correlations of 0.69 and 0.56, respectively; indicating significant inter-basin interaction on multidecadal timescales – a new finding.

Stated differently, PDV-NP's *positive* phase precedes the *negative* phase of LF-NAO by ~6.5 years, which, in turn, precedes AMO's *negative* phase by ~16.5 years. The inter-basin interaction loop is closed by noting the AMO's ~12.5-year lead over PDV-NP, which applies to both phases. The positive-to-negative phase evolution of PDV-NP thus takes ~35 years (=6.5+16.5+12.5). A 35-year estimate for phase-reversal would suggest an ~70-year period. The AMO and LF-NAO's period would be just as long in this scheme as the interaction-loop can begin with these modes too. The estimated period (~70 years) is broadly consistent with the independent estimate based on autocorrelation structure (Figs. 2.5b and 2.7), which indicated a 55-80-year period range, with PDV-NP (~55 years) and LF-NAO (~80 years) bracketing the range and AMO (~70 years) at its center.

Some discrepancy between these two estimates of variability timescale can arise from the shortness of the analyzed observational record (118 years) which accommodates less than 2 cycles of multidecadal SST variability in either basin and also from the potential influence of other intra- and inter-basin interactions.

Lead-lag correlations of PCs (Fig. 2.9) are provided spatiotemporal context in Fig. 2.10 from the display of SST and SLP regressions on the smoothed PDV-NP, LF-

NAO, and AMO PCs. The strategy is to temporally sequence the regressions on PDV-NP (over 6 years beginning with its peak +*ve* phase, time ↑), LF-NAO (over 16 years starting with its peak –*ve* phase, time ↓), and on AMO (over 12 years starting from its peak –*ve* phase; time ↑) to facilitate direct visual recognition of PDV-NP's phase-reversal; each lag period is set by the lead-lag links identified in Fig. 2.9.

Fig. 2.10 also provides a dynamical-thermodynamical underpinning to the inter-basin links. Lagged regressions of PDV-NP (left) begin with its peak +ve phase, consisting of a zonal band of warm SST anomalies (~0.3 K) extending from the coast of Japan to the central-eastern mid-latitude Pacific; note, some differences from its Fig. 2.2 (right, 4th from top) portrayal stem from the Fig. 2.10 regressions being on LOESS-smoothed PC. Interestingly, Atlantic SSTs are relatively quiescent at this time, but not SLP. In ~6 years (time ↑), PDV-NP's coherent structure dissipates while the Atlantic SSTs evolve into a triband structure resembling LF-NAO's –*ve* phase. Simultaneous and lagged regressions on the LOESS-smoothed, negative LF-NAO PC, shown in the middle column (time ↓) facilitate visual comparison. The similarity of the two top panels is impressive, attested by the spatial correlation of their Atlantic SST anomalies (0.93), corroborating the earlier finding that PDV-NP's peak phase leads ~6 years later to an opposite-signed LF-NAO peak phase – a Pacific orchestration of North Atlantic SST variability!

Lagged regressions on the negative LF-NAO PC (Fig. 2.10, middle column, time ↓) broadly show the Pacific SSTs as winding down, becoming non-descript in ~12 years – a time span in which the Atlantic SSTs exhibit phenomenal evolution, beginning with the southward leakage of cold-fresh water from the subpolar gyre

through the Newfoundland basin, along the Grand Banks (*t*+2 years) and its subsequent eastward, southeastward, and southwestward expansion into the midlatitude and subtropical basins. At *t*+16 years, SST anomalies in the North Atlantic exhibit resemblance to the mature-phase AMO SST anomalies (e.g., Fig. 2.6, left column, 3rd row; but for the sign), with a lop-sided amplitude distribution favoring the subpolar basin. To facilitate closer comparison,[7] simultaneous and lagged SST (and SLP) regressions on the negative AMO PC (with time ↑) are shown in the right column. Comparison of the two bottom panels indicates broad similarity in the Atlantic (but with more even subpolar-subtropical amplitude distribution in AMO regressions) but differences in the Pacific basin. The spatial correlation of the Atlantic basin SSTs (0.84) attests to the broad similarity noted earlier and supports the finding of LF-NAO's ~16-year lead vis-à-vis AMO – a notable intra-basin link on multidecadal timescale.

Lagged regressions of the negative AMO PC (Fig. 2.10, right column, time ↑) show gradual diminution of SST anomalies in the Atlantic alongside coherent development in the Pacific basin. At *t*+12 years, the Pacific SST anomalies resemble the *–ve* phase of the PDV-NP (or +*ve* PDO) while the Atlantic anomalies are anemic; the resemblance with the *–ve* PDV-NP phase is supported by the robust spatial correlation (−0.92) of the Pacific SST anomalies.

The phase reversal of the multidecadal PDV-NP mode evidently involves both Pacific and Atlantic-leading inter-basin interactions along with modal interactions within the Atlantic basin. Such assertions can be made also for the LF-NAO and AMO

[7] Fig. 2.6 shows SST regressions on the unsmoothed PCs, not the LOESS-smoothed PCs used in Fig. 2.10.

modes – all indicating the importance of inter-basin interactions in the generation of multidecadal SST variability.

2.5.3 Inter-basin links – Mechanics

Investigation of the mechanisms generating inter-basin linkage is beyond the scope of this observational analysis, for reasons of both space and the climate modeling experiments that would need to be conducted for understanding how regional and remote influences of each basin develop. A brief commentary on related atmospheric circulation – a key link agent – however follows, albeit at the surface. The surface focus, through SLP regressions, will limit insights on inter-basin signal propagation (best tracked at an upper-tropospheric level) but could indicate how the near-surface ocean is influenced.

The concurrent SLP regressions on the PDV-NP PC (Fig. 2.10, left, bottom) consists of an expansive anticyclone in the Pacific midlatitudes and another over northeastern Canada. The former – the more impressive one – weakens the Aleutian Low (and the midlatitude westerlies), and as noted earlier (section 2.4.4), the collocation of the westerly reduction region [where ∂(SLP)/∂y is large and +*ve*] and the +*ve* SST anomalies supports the surface flux modulation origin for the SST anomalies.[8] In subsequent years, the Aleutian Low recovers some but both it and the Icelandic Low remain weaker than normal (e.g., Fig. 2.10, center, top-three). Interestingly, SLP regressions, with a +*ve* ∂(SLP)/∂y structure over both northern basins, reflect the presence of geostrophic easterly anomalies in the middle-high latitudes, not unlike that

[8] Note the small contour interval (0.05 hPa) in SLP regressions which would lead to ~1 m/s change in wind speed – small but consequential given the multidecadal timescales.

in the low-phase of the index cycle (e.g., Namias 1950). SST anomalies in the subpolar North Atlantic, unlike those in the Pacific, are not in accord with the surface flux modulation hypothesis, e.g., cold SSTs at t+2 and t+4 years underlie easterly surface wind anomalies, i.e., reduced wind-speed regions. To be sure, the North Atlantic has complex bathymetry, with Labrador, Irminger, and Newfoundland basins, and several regional current systems – all potentially enhancing the contribution of ocean dynamical processes, including advection in the generation of surface-subsurface variability.

2.6 Analysis sensitivity and mode physicality

2.6.1 Sensitivity tests

The robustness of the identified variability modes, especially multidecadal ones, is assessed by perturbing the primary analysis by changing the analysis domain, the number of modes rotated, and the width of the sampling window. Table 2.1 lists the sensitivity tests.

Test T1 closely resembles the primary analysis (T0) but for a 10° southward shift in the analysis domain's northern boundary; the boundary is even further southward shifted in T3. Test T2 involves a change in the number of modes rotated (from 11 to 10) vis-à-vis T1. The temporal width of the sampling window is larger (7-seasons) in T4 vis-à-vis in T0, to assess if the 5-season window width was adequate to sample decadal-multidecadal variability evolution.

Table 2.1. Sensitivity Tests: T0 is the primary analysis while T1-T6 are additional analyses performed for assessment of T0's robustness. Departures from T0 (or its cousins) are enumerated below.

Name	Domain	Modes Rotated	Width of sampling window
T0	80ºN-20ºS, 0º-360º	11	5-season
T1	70ºN-20ºS, 0º-360º	11	5-season
T2	70ºN-20ºS, 0º-360º	10	5-season
T3	60ºN-20ºS, 0º-360º	11	5-season
T4	80ºN-20ºS, 0º-360º	11	7-season
T5	Pacific Ocean (60°N-20°S, 120°E-60°W)	7	5-season
T6	Pacific + Indian Ocean (60°N-20°S, 30°E-60°W)	7	5-season

The analysis domain is restricted to the Pacific basin in T5 and to the Indo-Pacific basin in T6, relative to T3; note, a smaller number of modes are rotated in T5 and T6, commensurate with the smaller spatial domain. Sensitivity results are summarized in Table 2.2 where each mode of the primary analysis (T0) is compared with its perturbed counterpart; the correlation of PCs, variance explained, and the corresponding rank are all tabulated.

The principal findings from Table 2.2 are:

- Low sensitivity to modest variations in the analysis domain's northern boundary: At 80°N in Test T0, 70°N in T1, and 60°N in T3. The PC correlation and explained variance are almost identical in T0 and T1. T0 was chosen as the primary analysis to fully resolve variations of the subpolar gyre along with its current systems. Test T3 (60°N boundary) results are very close to T0's but for the representation of

Sub-Arctic variability – understandably, in view of T3's curtailed northern domain. Note, the total amount of explained variance increases with decreasing domain size for the same number of modes, as expected.

Table 2.2. Sensitivity Results: Column 1 lists the eleven variability modes obtained in the primary analysis (T0). The number following each mode is the percentage variance explained by it, and the subsequent number, its rank. The number in parentheses in the top row is the total percentage variance explained by all modes in that analysis. Columns 2-7 list modal features, with the three slash-delimited numbers denoting correlation between the unsmoothed principal component of the test case (T1-T6) and the primary analysis (T0) over the full period (1900-2018), the percentage variance explained by that mode, and its rank in the test analysis, respectively. Dashed spaces indicate 'not applicable.'

T0 (60.9)	**T1** (61.9)	**T2** (60.7)	**T3** (62.8)	**T4** (58.6)	**T5** (64.5)	**T6** (62.1)
Trend/16.4/1	0.99/15.7/1	0.99/16.0/1	0.99/15.6/1	0.98/17.1/1	0.96/11.9/3	0.96/16.1/2
ENSO Decay/12.8/2	0.99/13.2/2	0.99/13.3/2	0.99/13.6/2	0.77/8.8/3	0.99/18.9/1	0.99/17.0/1
ENSO Growth/10.1/3	0.99/10.4/3	0.99/10.4/3	0.99/10.7/3	0.75/6.8/4	0.99/15.4/2	0.99/13.4/3
PDV-PP/4.2/4	0.99/4.4/4	0.98/4.4/4	0.99/4.5/4	0.95/3.6/5	0.95/6.8/4	0.94/5.5/4
AMO/3.4/5	0.99/3.6/6	0.94/3.5/6	0.99/3.6/6	0.97/3.1/6	–	–
Atl. Niño/3.3/6	0.99/3.6/5	0.99/3.5/5	0.99/3.7/5	0.95/2.4/8	–	–
PDV-NP/2.7/7	0.99/2.8/7	0.99/2.8/7	0.99/2.8/7	0.83/2.7/7	0.92/4.3/5	0.88/3.8/5
Biennial/2.6/8	0.99/2.7/8	0.98/2.7/8	0.99/2.7/8	0.47/1.7/10	0.94/3.5/7	0.95/3.2/6
ENSO-NC/2.3/9	0.99/2.4/9	0.99/2.3/9	0.99/2.4/9	0.58/1.8/9	0.94/3.7/6	0.94/3.1/7
LF-NAO/1.7/10	0.98/1.6/10	0.97/1.8/10	0.93/1.8/10	–	–	–
Sub-Arc. DV/1.4/11	0.98/1.5/11	–	0.86/1.4/11	0.83/1.3/11	–	–

- Low sensitivity to the number of modes rotated: 10 rotated in T2 vis-à-vis 11 in T1, their only difference. PC correlations with T0's are between 0.97-0.99 but for one at 0.94, and variance explained by the 10-leading modes is close (60.4 vs.

60.7), indicating that the 10-leading modes are essentially unchanged, or robust.

- Sampling window sensitivity: Tests T0 and T4 differ only in the sampling window-width, with T4's being larger (7-seasons). Immediately noted are the modest correlations (0.47-0.77) of the interannual modes comprising ENSO (Canonical ENSO Growth and Decay, Non-Canonical ENSO, and Biennial Variability); T4's 2nd-leading mode is most correlated with ENSO-Growth (0.57) among the T0 modes but this is not noted in Table 2.2 as T4's 4th-leading mode is even more strongly correlated with T0's ENSO-Growth (0.75, and thus noted in the Table). The trend and decadal-multidecadal modes fare better, with correlations in the 0.83-0.98 range but the LF-NAO mode of T0 has no counterpart in T4. Additional analysis revealed that the wider sampling window is an overkill in the interannual context, with over-sampling leading to ENSO-Growth's capture as 2 modes and aliased representation of the other ENSO modes. This misrepresentation is not without collateral damage in the decadal-multidecadal realm. The test indicates that the 5-season-wide variability sampling window may be optimal.

- The Pacific basin analysis (T5) is very similar to Guan and Nigam's (2008) but for the updated data set period. The T5 and the Indo-Pacific basin analysis (T6) exhibit PC correlations in the 0.92-0.99 and 0.88-0.99 range, respectively; the weakest correlation in both cases is for the PDV-NP mode (0.92 and 0.88, respectively). That this of all the Pacific modes is impacted the most by the inclusion of the Atlantic basin (T0), indirectly, attests to the significance of inter-basin links in PDV-NP's evolution.

2.6.2 Mode physicality

Assessing the physicality of modes – their physical realizability – is an important step after the mathematical/statistical analysis that yields the modes. These analyses identify optimal structures that succinctly (i.e., efficiently) capture variance but with no assurance that such optimal structures are realizable/realized. A straightforward test of physicality is scanning the observed (or simulated) variability structures for modal analogs. Indirect tests are based on correlations with related but independently gathered/analyzed data. Both have been used in assessing the physicality of the SST variability modes (e.g., Mantua et al. 1997, who pioneered the use of fish recruitment in such assessments; and Guan and Nigam 2008, who used both analogs and fish recruitment data).

Observational Analogs

A mode is deemed to have an observational analog if the observed anomaly at any time strongly resembles the modal structure, i.e., the observed anomaly can be largely accounted for by the expression of just one mode. More formally, an observed anomaly is deemed to be a modal analog if any one of the PCs is much larger than all the rest at that time. The analog count – the total number of observational analogs in the analysis period – is a useful measure of the overall physicality of the analysis. Table 2.3 lists the number of observational analogs in the primary (T0) and perturbed analyses (T1-T6). The number depends on the analysis domain extent, with more analogs found in smaller domains (T1 and T3 vs. T0; T5 vs. T6). The analog count will, of course, be smaller with fewer modes (T2 vs. T1). T0 has 37 analogs, less than that in T1 and T3,

but T0 was chosen as the primary analysis because its more northern resolves subpolar variability.

Table 2.3. Number of observational analogs present in various (T0-T6) analyses of seasonal SST variability during the period 1900-2018. An analog is deemed to occur when the absolute value of the unsmoothed principal component (PC) of any one mode is larger than that of all others by at least one unit in that season; note the PCs are orthonormal. Mathematically, if $| |PC_i(t)| - |PC_j(t)| | > 1.00$ for all j not equal to i, an analog is counted at time t.

	T0	**T1**	**T2**	**T3**	**T4**	**T5**	**T6**
Analog Count	37	38	31	52	31	44	42

Correlations with Fish Recruitment

Fish recruitment provides a unique assessment of mode physicality, especially for the decadal-multidecadal SST variability modes which can influence marine ecosystems. The North Pacific and Bering Sea recruitment records of Hare and Mantua (2000) for the 1965-1997 period were augmented and new ones assembled for the North Atlantic basin (cf. section 2e). Their correlations with the Pacific (PDV-PP, PDV-NP) and Atlantic (AMO, LF-NAO) modes are listed in Table 2.4, along with those of the widely used multidecadal SST variability indices (e.g., PDO and AMO).

The PDV-NP is most strongly correlated (−0.76) with the Gulf of Alaska halibut (FR4), and then with West Coast mackerel (−0.63, FR5);[9] corresponding PDO correlations are 0.73 and 0.66. Longer recruitment records such as FR12-13 (each 96-years long vis-à-vis the 33-year-long FR4-5) are preferred in assessment of multidecadal variability,[10] yielding PDV-NP correlations of −0.41 and −0.45, and PDO

[9]Guan and Nigam's (2008) PDV-NP correlations with FR4 and FR5 were −0.74 and −0.73, respectively, for the same 33-year period.

[10] These longer records – from models – differ significantly in the early period when within-model standard deviation is as large as half of the signal in some years; limiting their utility in physicality assessment.

ones of 0.39. Correlations with both short and long recruitment records reveal that the PDV-NP PC is, at least, as good a marker of marine ecosystem variations as the PDO – and a preferred one, perhaps, in view of its temporal orthonormality with other PCs at zero-lag.

Table 2.4. Correlations of the unsmoothed principal components (PCs) of the Pacific and Atlantic multidecadal SST variability modes from the primary analysis (T0) with selected Fish Recruitment (FR) records. The FR source is noted in the related footnote while the period is listed next to its name. All the time series, including PCs, are annually resolved here. The two highest correlations for each decadal-multidecadal mode are in bold.

FR #	Fish Recruitment Record	Multidecadal PCs and Variability Indices						
		PDV-NP PC	**PDO** Index	**PDV-PP** PC	**NPGO** Index	**AMO** PC	**AMO** Index	**LF-NAO** PC
1	Eastern Pacific zooplankton biomass (40); 1965-1997	–0.19	0.10	0.20	0.32	0.46	0.23	–0.21
2	British Columbia coho salmon catch (67); 1965-1997	0.03	–0.17	**–0.42**	0.32	–0.28	–0.19	–0.33
3	British Columbia pink salmon catch (68); 1965-1997	–0.12	–0.13	–0.24	0.32	–0.13	0.07	0.01
4	Gulf of Alaska halibut recruitment (43); 1965-1997	**–0.76**	**0.73**	0.11	0.37	–0.07	0.06	0.41
5	West Coast mackerel recruitment (81); 1965-1997	**–0.63**	0.66	0.36	0.12	0.05	0.14	0.55
6	Central Alaska chinook catch (51); 1965-1997	–0.41	0.59	0.38	−0.12	–0.16	0.24	**0.76**
7	Eastern Bering Sea rock sole recruitment (20); 1965-1997	–0.42	**0.67**	0.34	−0.18	0.43	0.52	0.27
8	Central Alaska pink catch (54); 1965-1997	–0.45	**0.67**	**0.61**	−0.14	0.26	0.38	**0.56**
9	Regulatory area 3B halibut catch, IPHC; 1991-2014	–0.41	–0.12	–0.35	0.51	0.17	0.26	–0.51
10	Regulatory area 4A halibut catch, IPHC; 1991-2014	–0.50	–0.05	–0.20	**0.54**	0.13	0.25	–0.28

11	Regulatory areas 3B and 4A combined catch, IPHC; 1991-2014	–0.45	–0.10	–0.33	**0.53**	0.17	0.26	–0.48
12	IPHC Coastwide model; 1925-2010	–0.41	0.39	–0.05	0.11	–0.21	–0.16	0.18
13	IPHC Areas-as-fleets model; 1925-2010	–0.45	0.39	–0.11	0.15	–0.07	–0.04	0.21
14	Norwegian spring-spawning Herring; 1907-2010	0.28	–0.28	---	---	**0.54**	**0.57**	–0.20
15	Atlantic Mackerel (Canadian landings); 1901-2016	–0.11	0.06	---	---	–0.15	–0.02	–0.10
16	Atlantic Mackerel (US, Canada, Foreign landings); 1960-2016	0.11	–0.27	---	---	–0.53	–0.54	–0.32
17	Atlantic Menhaden; 1955–2013	0.20	–0.06	---	---	–0.15	–0.09	–0.24
18	Gulf of Maine Cod; 1982–2013	0.08	0.27	---	---	**−0.75**	**–0.70**	0.19

The PDV-PP PC exhibits highest correlation with the Central Alaska pink catch (0.61; FR8), and then with British Columbia Coho salmon (−0.42; FR2); the regional correlations, undoubtedly, stem from this mode's coastal footprints in the Gulf of Alaska (cf. Fig. 2.4); note, both correlations are from 33-year-long records. The North Pacific Gyre Oscillation (NPGO) – a close cousin of the PDV-PP – is however weakly correlated with the FR8 (−0.14) and FR2 (0.32) records. The NPGO does exhibit higher correlation (0.54) with FR10, i.e., catchment in the eastern Aleutians, but this record is only 24-years long.

The AMO PC and the AMO index (Enfield et al. 2001) are strongly correlated with the Gulf of Maine cod (FR18), at −0.75 and −0.70, respectively, but the record is only 32-years long. The PC and the index are similarly and reasonably correlated (−0.53 and −0.54) with Atlantic mackerel (FR16) whose record is longer (57-years).

The longest recruitment record in Table 2.4 is for the Norwegian spring-spawning herring (FR14, 104 years) and it is correlated with the PC and index at 0.54 and 0.57, respectively.

Inter-basin links are also manifested in Table 2.4:

- The AMO exhibits reasonable correlations with Pacific fisheries, e.g., its PC is correlated with Eastern Pacific zooplankton biomass (FR1) at 0.46 and the AMO index with Eastern Bering Sea rock sole recruitment (FR7) at 0.52; and not unexpectedly (cf. Fig. 2.6, middle-left panel).
- PDV-NP and the PDO index are likewise correlated with Norwegian spring-spawning herring (FR14) at 0.28; while smaller, the correlation is from a 3-times longer record and thus notable.
- Finally, and interestingly, the LF-NAO's strongest correlations with recruitment are found in the Pacific – with Central Alaska chinook catch (FR6, 0.76) and pink catch (FR8, 0.56); the strongest Atlantic basin correlation is with mackerel (FR 16, −0.32). LF-NAO's links with Pacific recruitment are not surprising given its substantial Pacific footprint (cf. Fig. 2.6, right).

2.7 Concluding remarks

The Pacific and Atlantic basins are found linked in the context of multidecadal variations of sea-surface temperature!

Across basins, the two prominent Atlantic modes – Atlantic Multidecadal Oscillation (AMO) and Low-Frequency North Atlantic Oscillation (LF-NAO) – are found linked to the key Pacific multidecadal mode – North Pacific decadal variability

(PDV-NP; resembles PDO's negative phase). The AMO leads PDV-NP by ~12.5 years while the LF-NAO lags the opposite phase of PDV-NP by ~6.5 years. The notable development of sea level pressure regressions in the other basin were early indicators of these basin links. Within the Atlantic basin, the AMO lags LF-NAO by ~16 years.

The inter-basin links become evident when modal linkage is investigated using measures that look beyond contemporaneous correlation – a commonly used metric which, interestingly, is mandated to be zero by the deployed principal component (PC) analysis – the PC rotation, notwithstanding. The notable lead-lag PC correlations and lead-lag regressions of the SST and SLP on the PCs build the case for inter-basin links in climate observations.

Other notable findings:

- The subsurface temperature and salinity anomalies linked with Atlantic multidecadal SST variability extend much deeper (to ~1000m) than those of Pacific variability; the PDV-NP extensions reach only ~450m while the PDV-PP ones are even shallower (~300m).
- SST anomalies of the Pan-Pacific decadal mode (PDV-PP; identified by Guan and Nigam 2008) are similar to the horseshoe-shaped, coastally-focused SSTs associated with the North Pacific Gyre Oscillation (NPGO; Di Lorenzo et al. 2008), the 2nd leading EOF of the modeled sea surface height variations in the extratropical basin. Despite this similarity, connections between the two have remained largely uninvestigated in the past decade.

The Achilles heel of the above findings is the shortness of the observed SST record which presently accommodates less than 2 cycles of multidecadal variability.

While this has not stopped the pursuit to characterize the surface/subsurface structure of the PDO and AMO since the late 1990s – when the observed records were even shorter – the robustness of our finding of the Pacific-Atlantic basin link will remain a concern until such time we have multiple multidecadal cycles in the observed record. Unfortunately, climate system models – at least, the IPCC-AR5 genre – were unable to generate realistic spatiotemporal expressions of multidecadal variability in the Atlantic basin (e.g., Kavvada et al. 2013), precluding the use of this model class in studying inter-basin links and their underlying mechanisms.

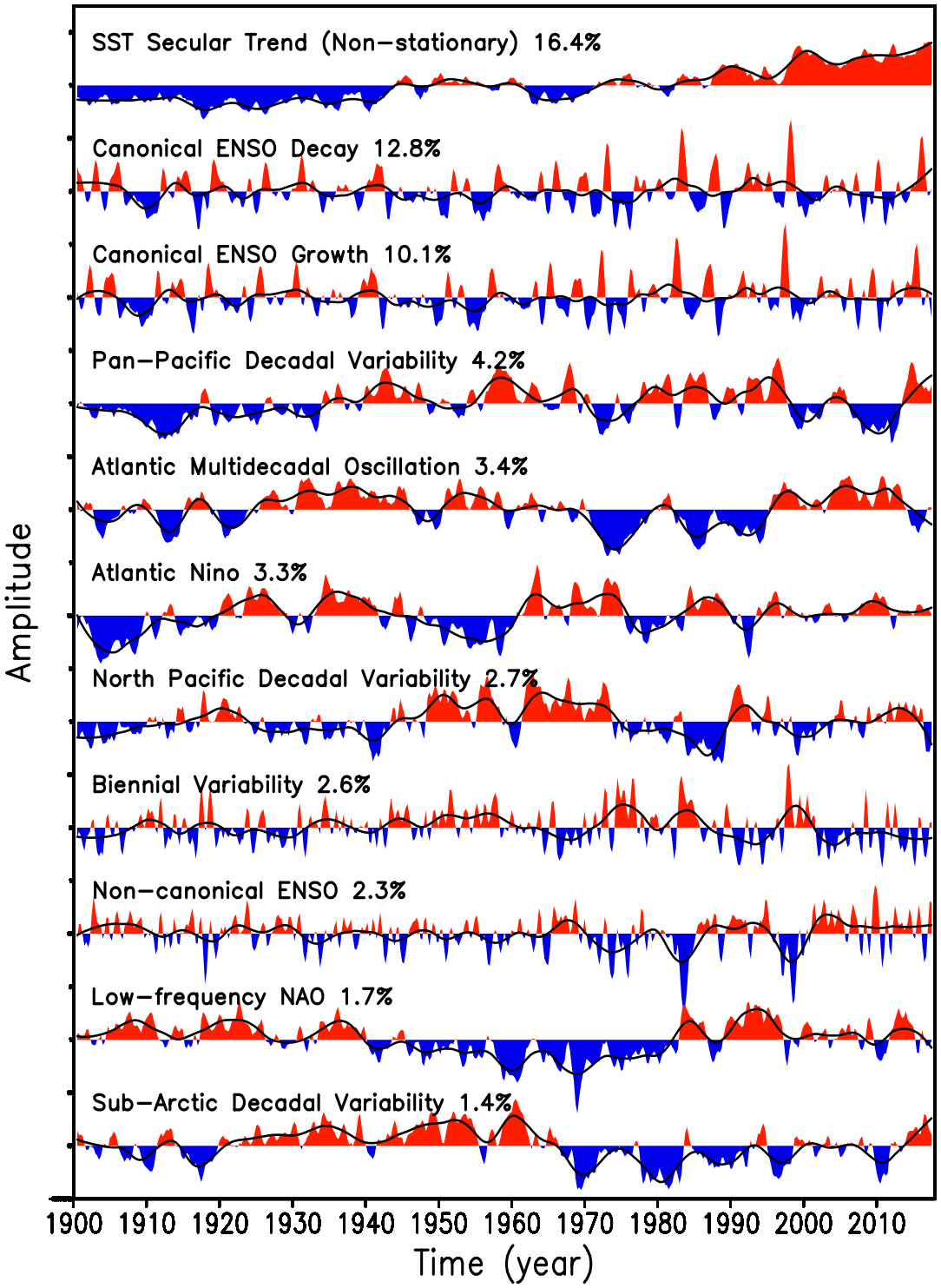

Figure 2.1. *Leading principal components (PCs) of global SST variability* obtained from an extended-EOF analysis of Hadley SSTs; the PCs extend from 1900 (summer) to 2017 (summer). Tick marks on the vertical axis are drawn every three standard deviations. The original, seasonally resolved PCs are shaded while their smoothed versions (from LOESS-10% smoothing) are shown using solid black lines. The percentage of SST variance explained by each mode of spatiotemporal variability is indicated next to its name.

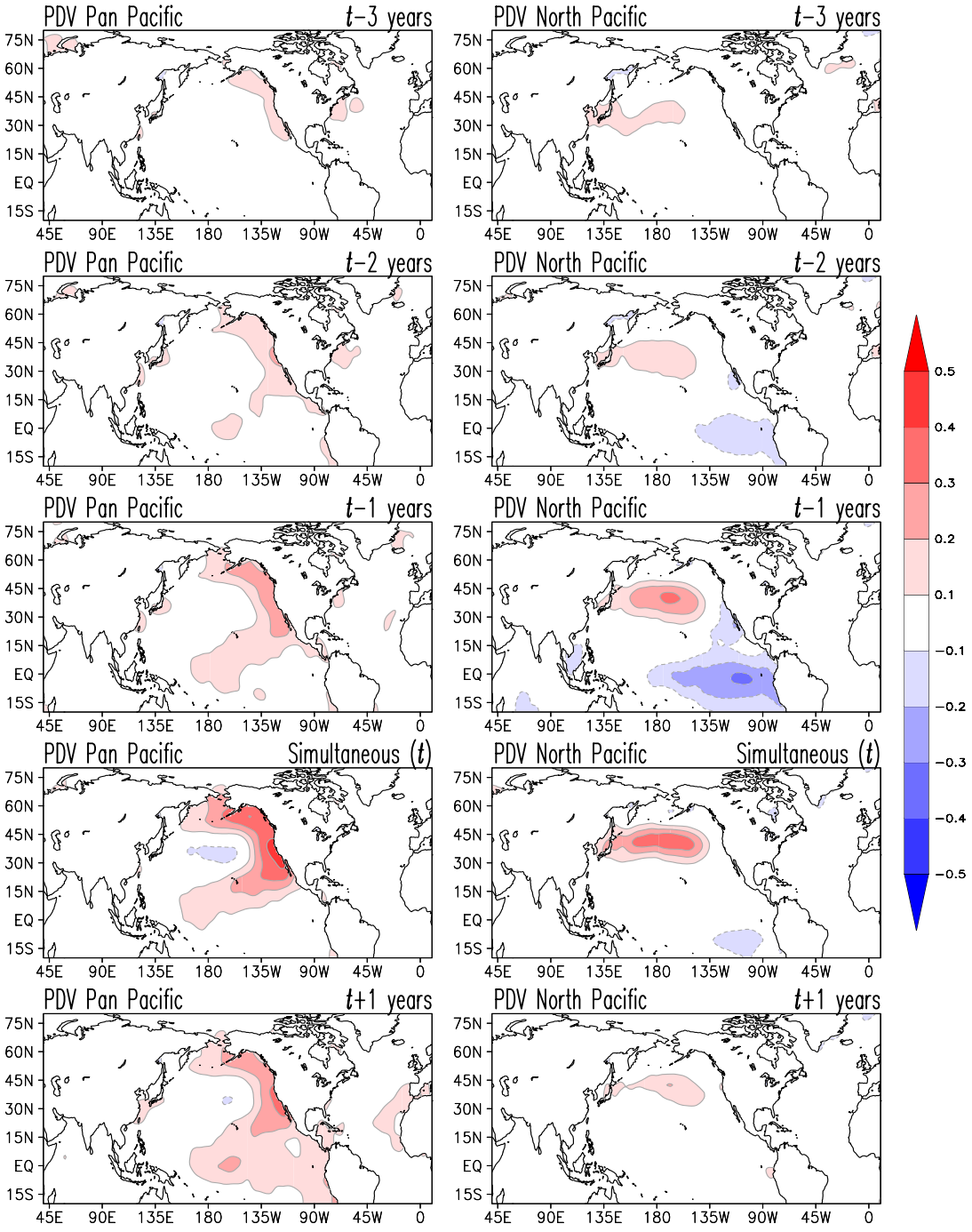

Figure 2.2. *Spatiotemporal evolution of Pacific decadal SST variability*: The Pan-Pacific (PDV-PP, left) and North Pacific (PDV-NP, right) modes are displayed over a five-year span at yearly intervals, with time running downward in both columns. Lead-lag regressions of the seasonal SST anomalies on the PDV-PP and PDV-NP PCs over 1900-2017 are displayed, with label t denoting simultaneous regressions. Red (blue) shading denotes positive (negative) SST anomalies and the zero contour is suppressed. Contour interval and shading threshold is 0.1 K. The fields are displayed after 12 applications of smth9 in GrADS.

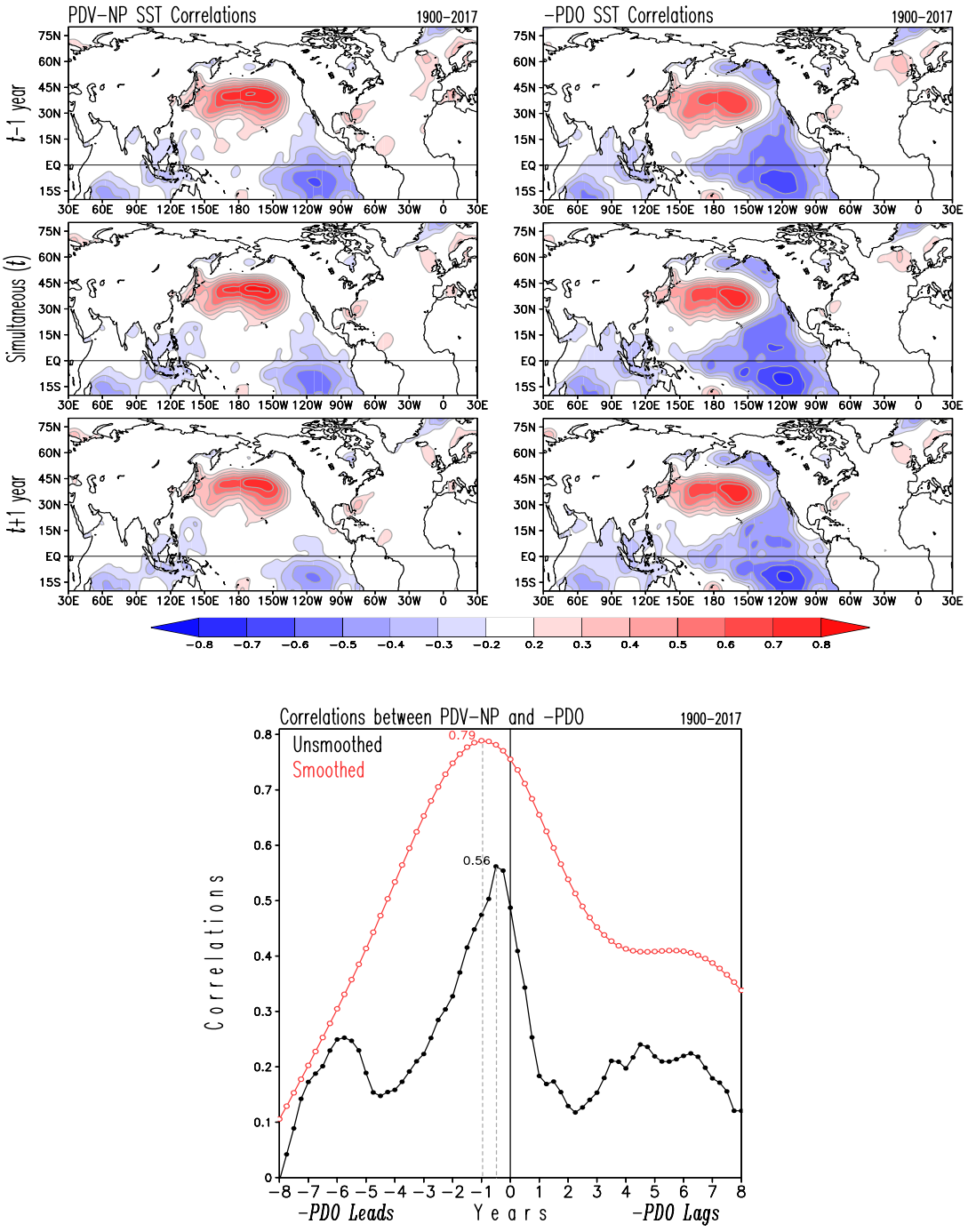

Figure 2.3. *The PDV-North Pacific SST variability mode (PDV-NP) and Pacific Decadal Oscillation (PDO)*: Lead-lag SST correlations on the PDV-NP principal component (left) and the negative PDO index (right) over 1900-2017 in upper panels; the PC, PDO index, and the SSTs were all temporally smoothed (LOESS-10%) before computation. Red (blue) shading denotes +ve (–ve) values starting at ±0.2. Correlations were spatially smoothed with GrADS function smth9, applied 12 times. Lower Panel: Lead-lag correlations of the PDV-NP PC and the negative PDO index over 1900-2017 are displayed, both before (black curve) and after LOESS-10% smoothing (red curve). The two are maximally correlated at 0.56 (0.79) at 2-season (1-year) lead of the unsmoothed (smoothed) negative PDO index.

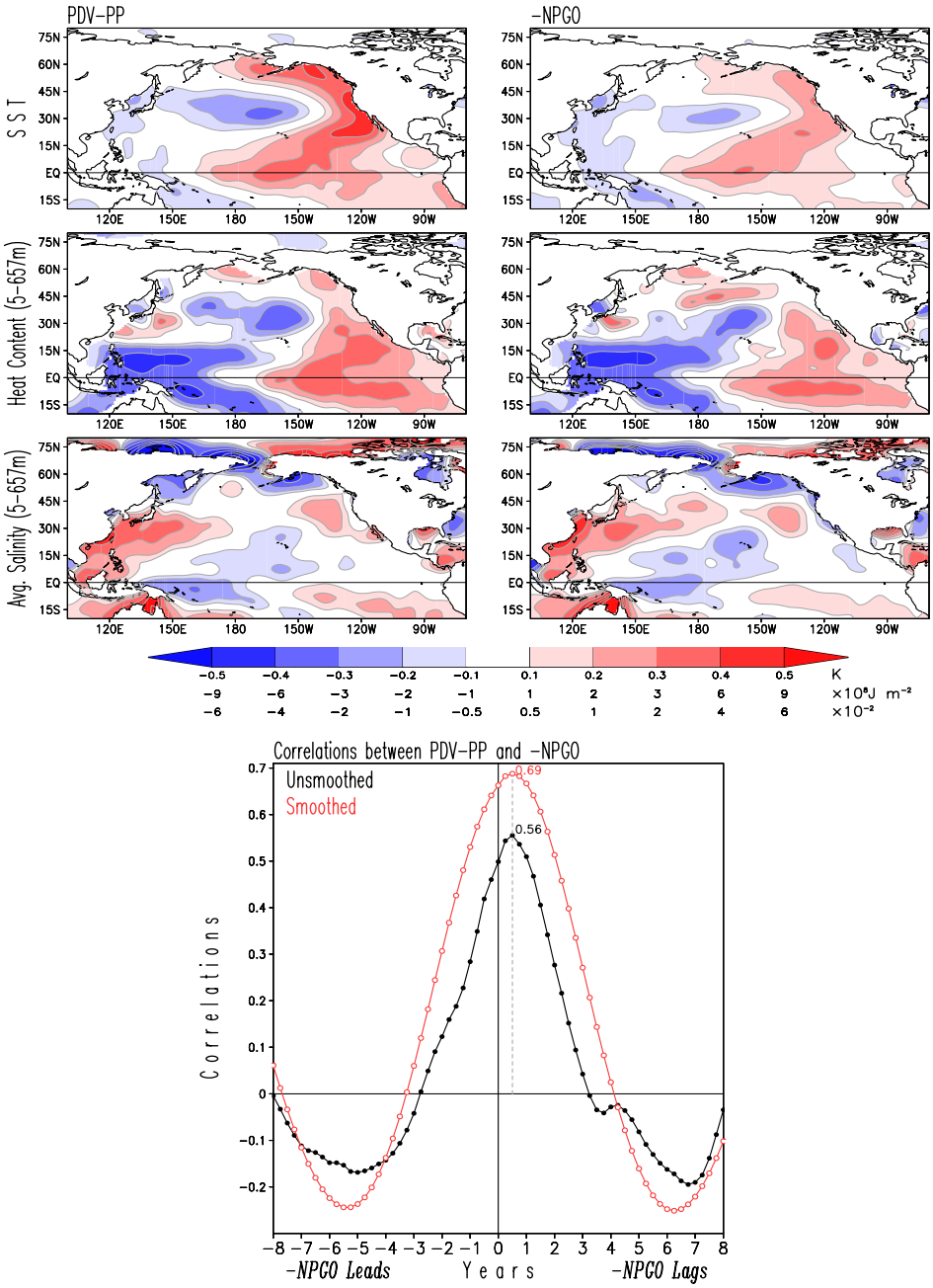

Figure 2.4. *The PDV-Pan Pacific SST variability mode (PDV-PP) and North Pacific Gyre Oscillation (NPGO)*: Simultaneous upper-ocean regressions on the smoothed PDV-PP principal component (left) and the negative NPGO index (right) in the common 1950-2017 period are in upper panels; time series were smoothed to retain similar decadal-multidecadal variabilities from the use of 10% LOESS filter on the 118-yr-long PC and a 17% filter on the 69-yr-long index. SST (K, top), upper-ocean (5-657m) heat content (10^8 J m^{-2}, middle), and vertically averaged (5-657m) salinity (10^{-2}, bottom) regressions are displayed after spatial smoothing with GrADS function smth9, applied 12 times, and plotted using shading and threshold specified in the color bar. Lower Panel: Lead-lag correlations of the PDV-PP PC and the negative NPGO index over 1950-2017 are displayed, both before (black curve) and after smoothing (red curve). The two are maximally correlated at 0.56 (0.69) at 2-season lead of the PDV-PP PC.

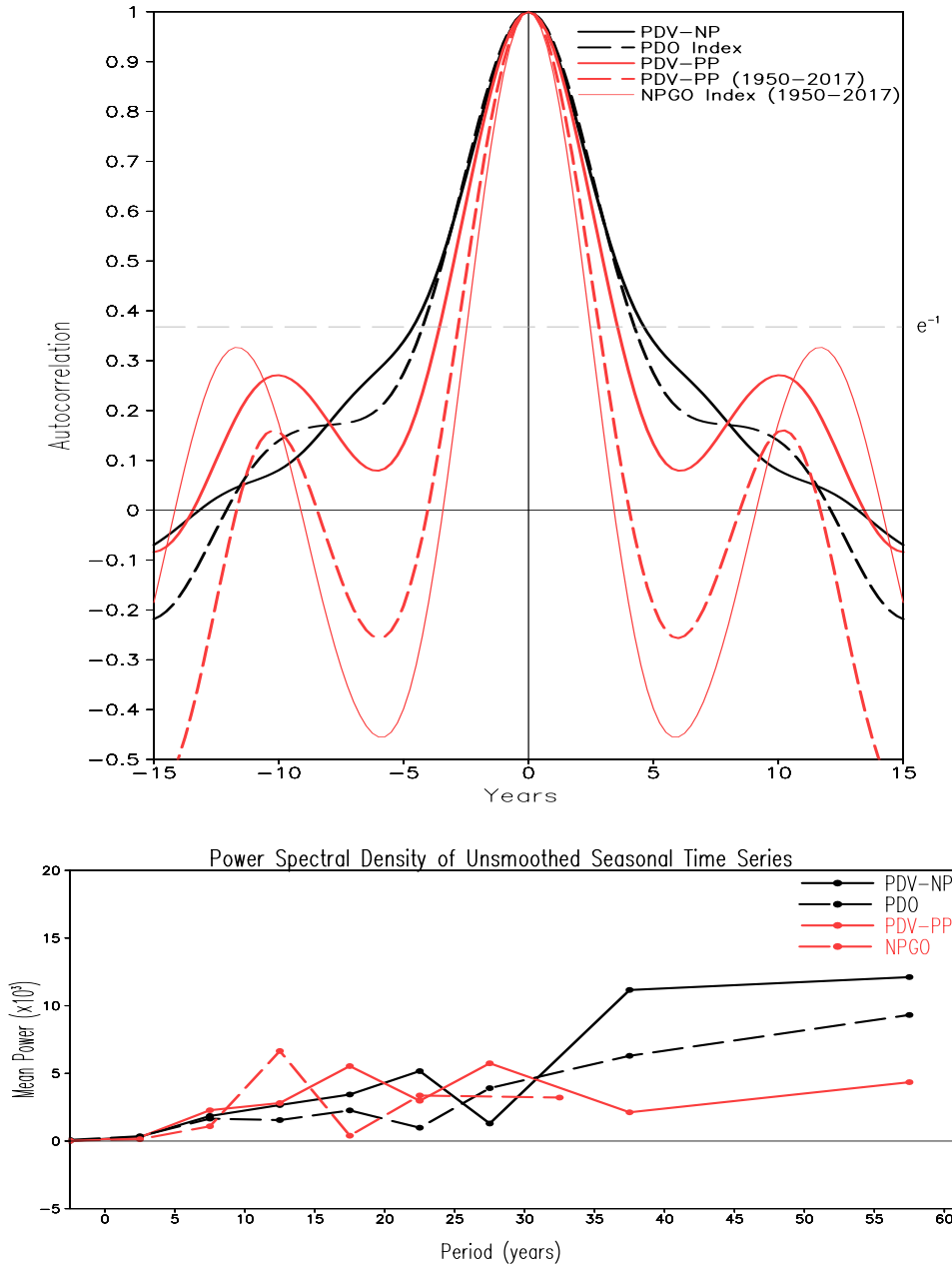

Figure 2.5. *Pacific Decadal Variability timescales*: Autocorrelations of the PDV-North Pacific (solid black) and Pan Pacific (solid red) principal components are compared with that of Pacific Decadal Oscillation (PDO, dashed black) and North Pacific Gyre Oscillation (NPGO, dashed red). PDV-NP and PDO autocorrelations were obtained from their LOESS-10% smoothed versions over 1900-2017. Autocorrelation of the similarly smoothed PDV-PP PC are in solid red for the full-period (1900-2017) and dashed red for the latter half (1950-2017). To facilitate comparison, the NPGO index was smoothed with a LOESS-17% filter over 1950-2017, so as to retain timescales similar to those in PDV-PP. Autocorrelations of the smoothed NPGO index are in thin red. *Lower Panel*: Power spectra of the unsmoothed Pacific PCs/indices. The mean of the spectral peaks identified in each 5-yr bin (1-5yrs, 6-10yrs, 11-15-yrs, … ,56-60yrs) are plotted for the PDV-NP (solid black), PDO index (dashed black), PDV-PP (solid red), and the NPGO index (dashed red), with the x-axis showing the period (in years). See legend for more details. The NPGO spectra is curtailed in view of its shorter record length.

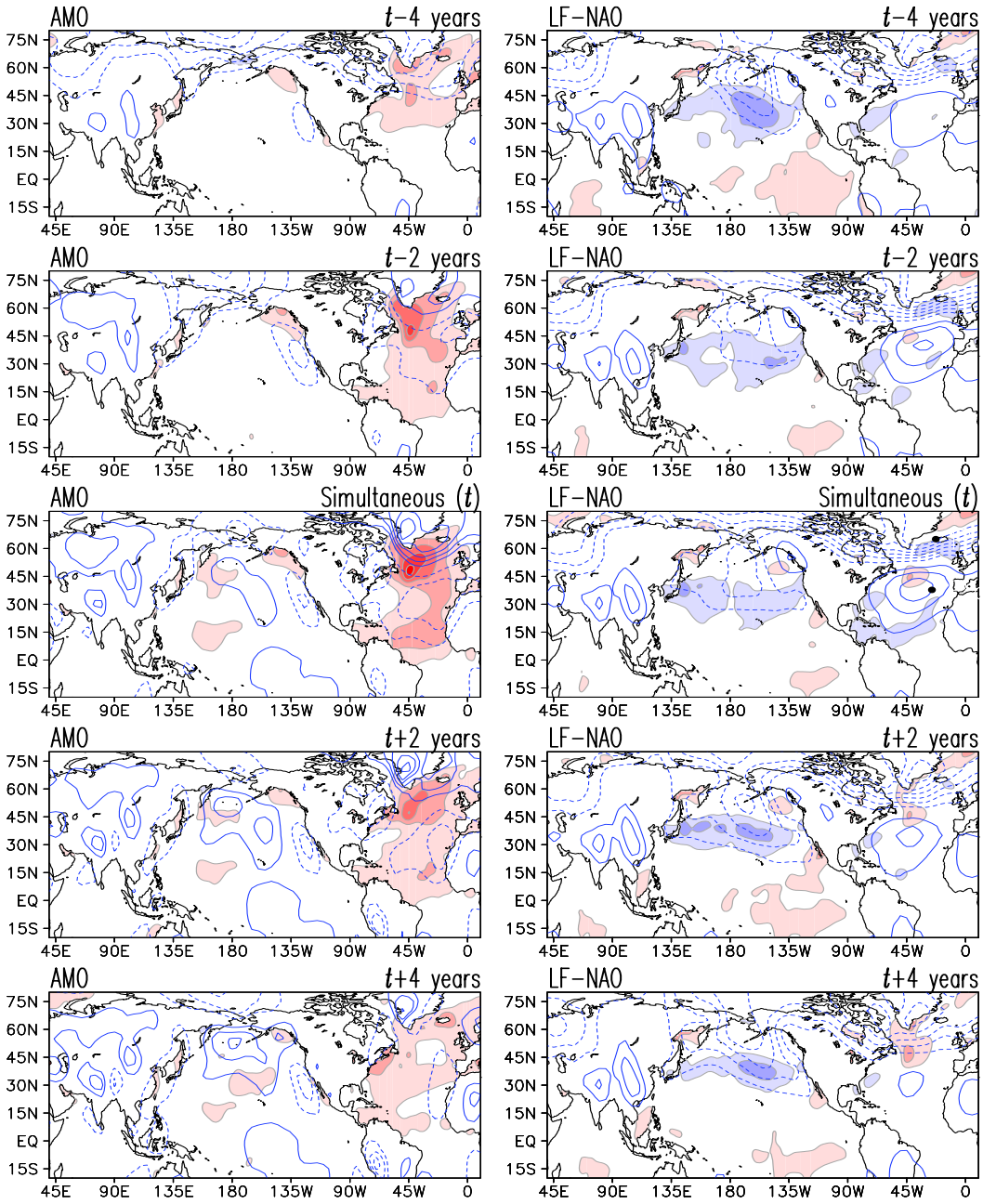

Figure 2.6. *Spatiotemporal evolution of Atlantic multidecadal SST variability*: The Atlantic Multidecadal Oscillation (AMO, left) and the Low-Frequency North Atlantic Oscillation (LF-NAO, right) modes are displayed over a ten-year span at 2-year intervals, with time running downward in both columns. Lead-lag regressions of the seasonal SST (shaded) and sea-level pressure (SLP, from HadSLP2; contoured) anomalies on the LOESS-10% smoothed AMO and LF-NAO PCs over 1900-2017 are displayed, with label *t* denoting simultaneous regressions. Red (blue) shading denotes positive (negative) SST anomalies and the zero contour is suppressed. The overlaid solid (dashed) blue contours denote *+ve (−ve)* SLP regressions. Contour interval and shading threshold for both regressions is 0.1 (K, hPa). The fields are displayed after smoothing from 12 applications of smth9 in GrADS. The black dots in LF-NAO's mature-phase mark Stykkisholmur/Reykjavik (Iceland) and Ponta Delgada (Azores) – the two stations whose SLP anomalies define the synoptic-monthly NAO index.

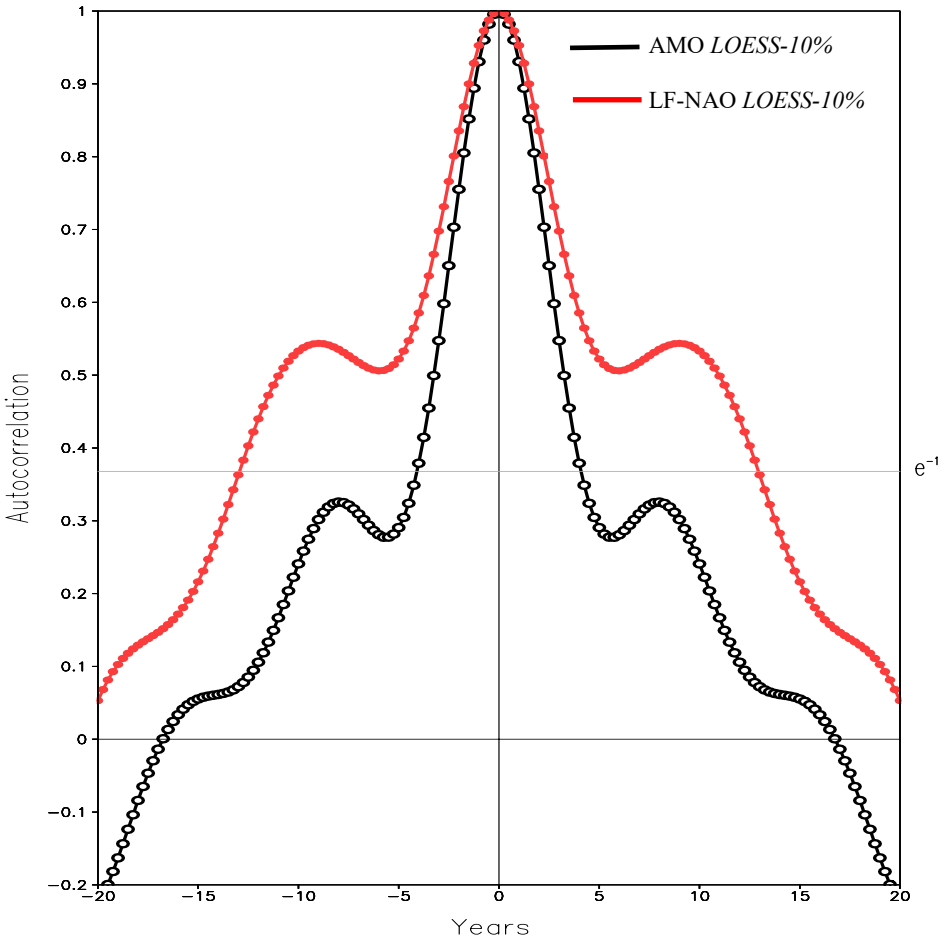

Figure 2.7. *Atlantic Multidecadal Variability timescales*: Autocorrelation of Atlantic Multidecadal Oscillation (AMO, black) and the Low-Frequency North Atlantic Oscillation (LF-NAO, red) principal components. The autocorrelations were obtained from the LOESS-10% smoothed versions of the principal components over 1900-2017.

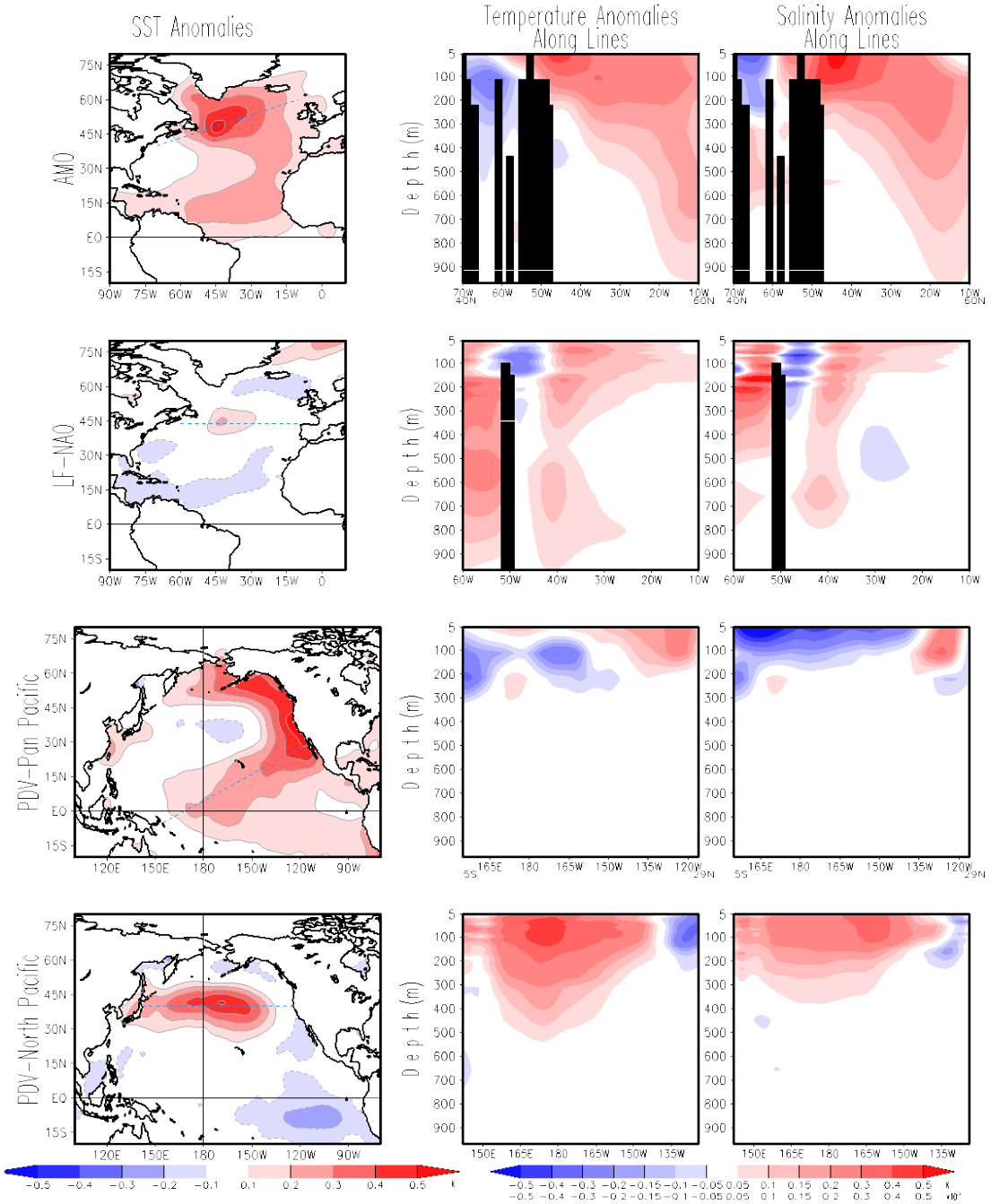

Figure 2.8. *Subsurface extensions of decadal-multidecadal SST variability*: Contemporaneous regressions of SST (left, K), and subsurface temperature (middle, K) and salinity (right, 10^{-1}) on the smoothed (LOESS-10%) principal components of AMO (top), LF-NAO (second from top), PDV-PP (second from bottom), and PDV-NP (bottom) over 1900-2017. The subsurface structure (middle and right columns) is along transects marked on the related mature-phase SST regressions (left column) using dashed blue lines; the transects intersect regions of maximum sea *surface* temperature anomalies; subsurface fields are from the EN4.2.1 data set. Red (blue) shading denotes positive (negative) regressions as per the color bars. The fields are displayed after smoothing from 12 applications of *smth9* in GrADS.

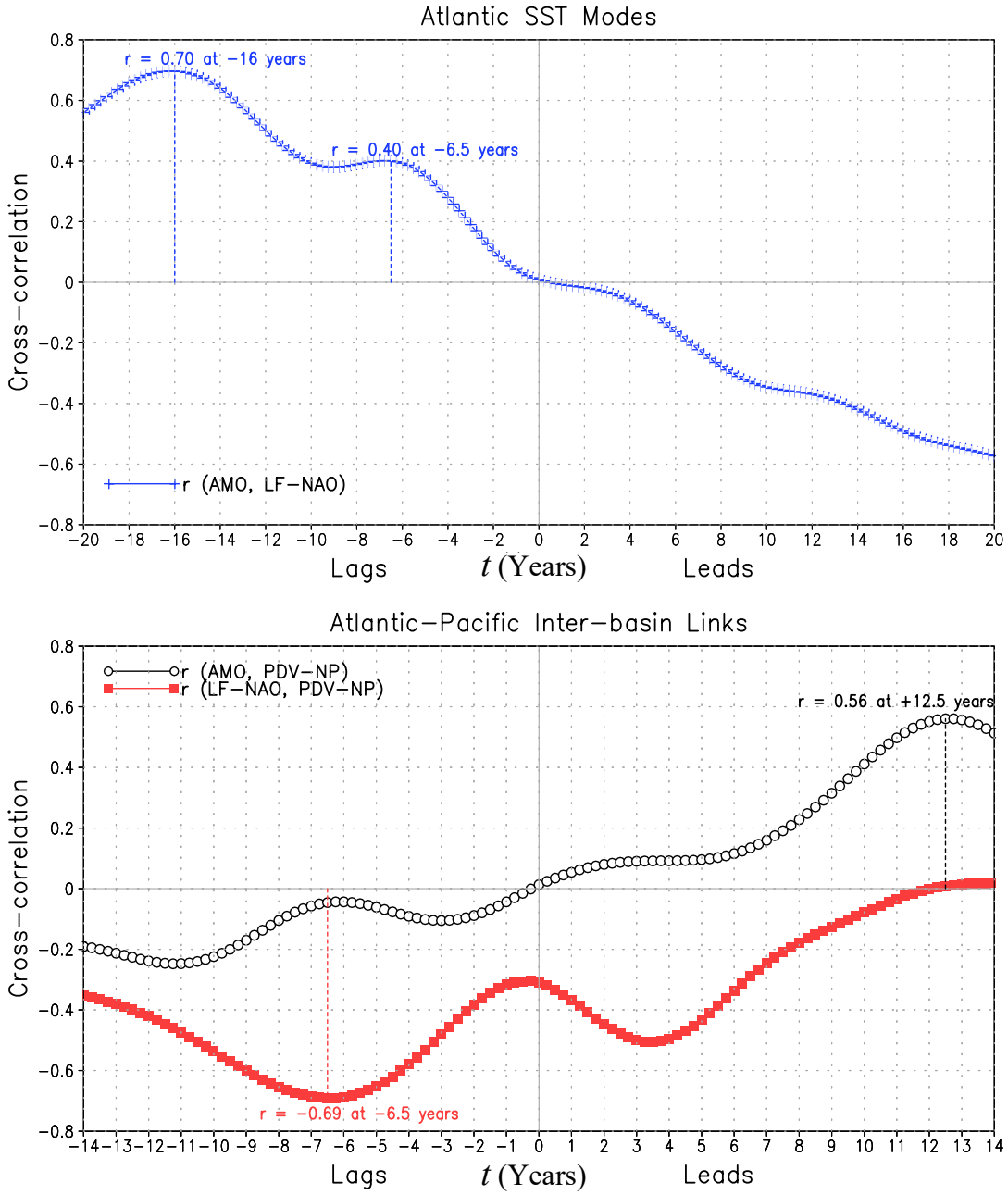

Figure 2.9. *Intra and Inter-Basin Modal Links*: Within-Atlantic basin links (upper panel) are documented from the lead-lag cross-correlations of the smoothed (LOESS-10%) Atlantic Multidecadal Oscillation (AMO) and Low-Frequency North Atlantic Oscillation (LF-NAO) principal components (PCs). The Atlantic-Pacific basin links (lower panel) are documented through lead-lag cross-correlations of the smoothed AMO and PDV-NP PCs (black), and the smoothed LF-NAO and PDV-NP PCs (red). The plotting convention is as follows: If r(A, B) > 0 for t < 0, B leads A; if $r > 0$ for t > 0, B lags A; and if $r < 0$ for t > 0, B lags –A.

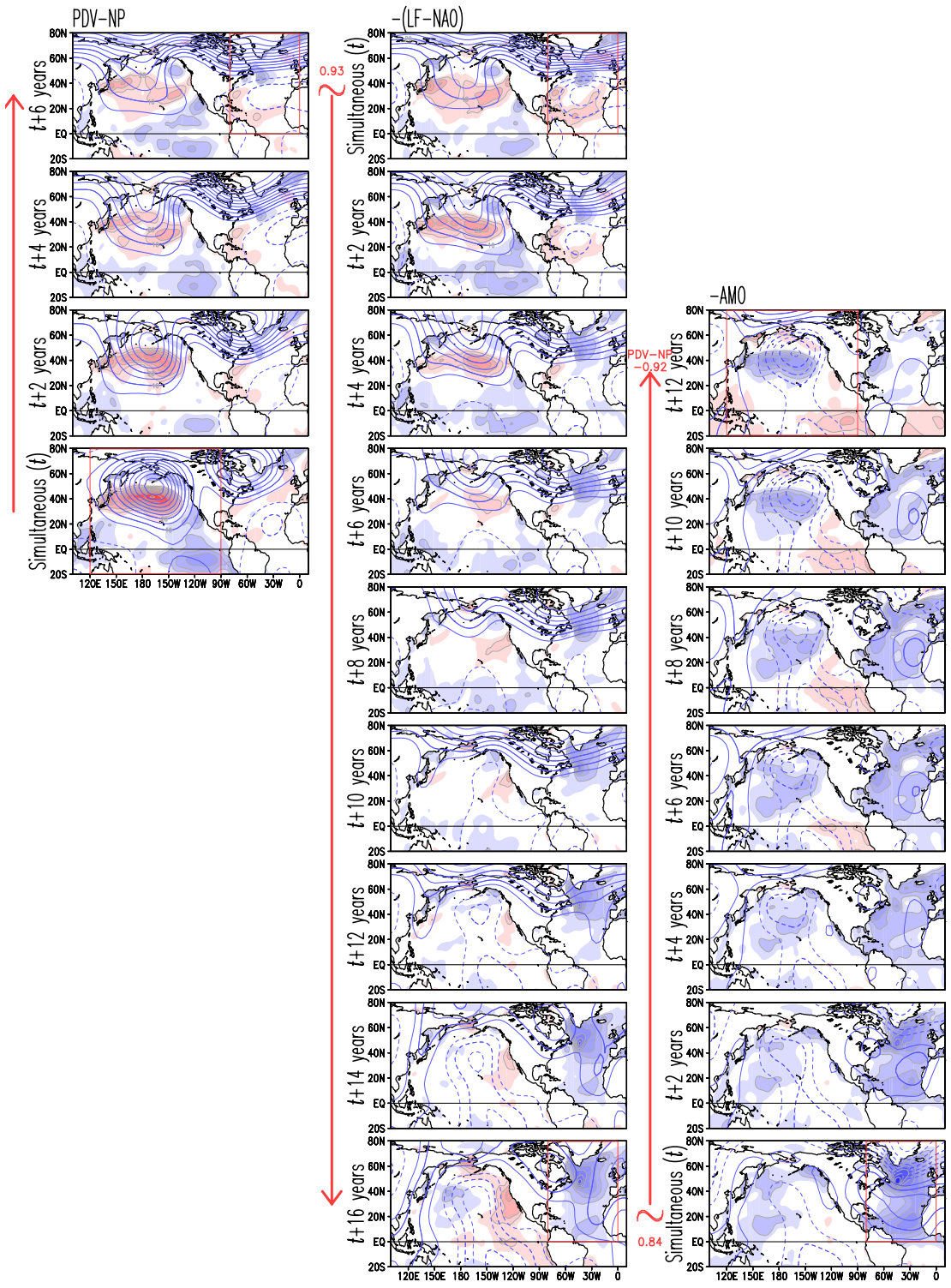

Figure 2.10. *Basin links manifest in lag-regressions of multidecadal PCs*: Lagged regressions of SST (shaded) and SLP (contoured) on the smoothed (LOESS-10%) PDV-NP (left), negative LF-NAO (central), and negative AMO (right) PCs over 1900-2017, are shown from the mature phase at 2-year intervals with red arrows indicating increasing time lag. Red (blue) shading denotes *+ve (−ve)* SST regressions (K); the shading interval and threshold is 0.05K. The overlaid solid (dashed) blue contours denote *+ve (−ve)* SLP regressions at 0.05-hPa interval.

The fields are shown after smoothing from 12 applications of *smth9* in GrADS. Note, the 6-year-lag regressions on PDV-NP (top-left) resemble the mature *–ve* phase of the LF-NAO (top-middle), as evident from the high spatial correlation (0.93) of the Atlantic SST anomalies (within the red box in both panels). The 16-year-lag regressions of the negative LF-NAO, on the other hand, resemble the mature negative phase of the AMO (bottom-right), supported by the 0.84 spatial correlation of SST anomalies in the Atlantic domain (red box). Finally, 12-year-lag regressions of the negative AMO mode (top-right) closely resemble the mature phase of PDV-NP (bottom-left) in the Pacific basin but for the sign; the resemblance is underscored by the high spatial correlation (−0.92) of the SST anomalies in the Pacific basin (the red box in both panels). It is noteworthy that an initial *+ve* PDV-NP phase (bottom-left) leads to a *–ve* PDV-NP phase (top-right), i.e., a phase-reversal, after 34 years (=6+16+12 lags), from both intra and inter-basin interactions.

Chapter 3: SST-based Predictability and Prediction of the South Asian Summer Monsoon Rainfall Distribution

3.1 Introduction

The value of reliable, timely, and long-range predictions of summer monsoon rainfall cannot be overstated for the agriculture dominated economies of the Indian subcontinent (Gadgil and Gadgil 2006), where ~75% of annual rainfall arrives in the summer. Summer monsoon predictions have drawn considerable public/policy attention lately as South Asia becomes a resource stressed region: Rapid population and economic growth have led to significant land-use land-cover changes, heightened demand for freshwater and energy, degraded environment from aerosol and dust loadings, and increased GHG emissions. Regional hydroclimate (precipitation, surface air temperature, soil moisture, subsurface water) exhibits substantial – at times, precarious – trends in the post-1950s period (Kothawale and Rupa Kumar 2005; Bollasina et al. 2011; Turner and Annamalai 2012; Mishra et al. 2012; Dorigo et al. 2012; Krishnan et al. 2016). This environmental backdrop and the livelihood concerns and aspirations of a billion-plus people generate the demand for more accurate summer monsoon predictions, especially with longer lead times.

Forecasting of the summer monsoon rainfall has been carried out with both dynamical and statistical models. Dynamical modeling has used both atmospheric general circulation models (AGCMs) as well as coupled atmosphere-ocean models (Krishnamurti et al. 2006). Meanwhile, statistical models have employed a multiple

regression approach using several predictors (Rajeevan et al. 2007). Prediction of seasonal summer monsoon rainfall distribution over South Asia, however, remains challenging (Krishnamurti et al. 1999; Gadgil et al. 2005; Krishnamurti and Kumar 2012). The prediction skill has remained marginal and stagnant for several decades despite advances in the representation of physical processes (including ocean-atmosphere coupling, moist convection, aerosol/dust effects), numerical model resolution, data assimilation techniques, and the range of assimilated variables. The low seasonal predictability of dynamical models is due to their sub-optimal simulation of the mean rainfall distribution over the South Asian monsoon region (Waliser et al. 2003) and the atmospheric response to SST forcing (Kang et al. 2004). While the representation of ocean-atmosphere interaction is considered essential in predictive models (Krishna Kumar et al. 2005), its representation in current models is sub-par (Bollasina and Nigam 2009, hereafter BN2009; Rajeevan et al. 2012). For instance, BN2009 showed that coupled climate simulations exhibit large systematic biases in precipitation, evaporation, and SST in the Indian Ocean, often exceeding 50% of their climatological values. Many of the biases were common across several model simulations. Representation of air-sea interaction was also found compromised as coupled models emphasized local forcing in the Indian Ocean (e.g., large precipitation–SST correlations), at odds with the weak local links in observations.

Seasonal predictability of climate is premised on the presence of influential system components with large thermal inertia, leading to longer timescale (vis-à-vis seasonal) variability. Upper oceans and the Himalayan cryosphere meet the criterion, but reliable observational records exist only for the former albeit at the surface. SST is

an influential variable, especially in the Tropics (Sikka 1980; Charney and Shukla 1981; Shukla and Paolino 1983; Rasmusson and Carpenter 1983; Kumar et al. 1999). It affects both regional and faraway climate through modulation of surface fluxes, convection and clouds, and moisture transports, among others. The influence is not one-way as SST responds to atmospheric circulation and near-surface meteorology.

As such, SST of neighboring seas and faraway oceans are potential predictors of the variations of the southwest monsoon. Sahai et al. (2003) introduced an empirical model for deterministic monsoon prediction using SST from different geographical locations at various temporal lags as predictors. A probabilistic monsoon forecast system using a large ensemble of empirical forecasts was presented in Sahai et al. (2008); the system demonstrated good skill in predicting the monsoon-related droughts of 2002 and 2004. However, there is a lack of observationally rooted analyses for establishing SST-based summer rainfall prediction targets, which can, in turn, facilitate the monitoring and improvement of dynamical models. The present analysis is motivated by such evaluative opportunities. Recent dynamical modeling studies (Yang et al. 2012; Saha et al. 2016; Pillai et al. 2018) have used SST information-based approaches to assess the predictability of the Asian summer monsoon in the Climate Forecast System (CFS) model. The skill of the SST indices — Niño 3, El Niño Modoki Index (EMI), equatorial East Indian Ocean (EEIO) anomaly — were assessed for prediction of the Indian summer monsoon rainfall in CFSv2 hindcasts. Determination of the SST-based potential predictability of seasonal summer monsoon rainfall over South Asia and follow-up hindcasting of seasonal rainfall anomalies in an independent period are the principal targets of this study.

The enabling SST analysis in this predictability study is based on the objective identification of the spatial and temporal recurrence of SST anomalies using the extended empirical orthogonal function technique; this technique extracts SST variability modes without imposing any periodicity constraints and pre-processing of data. As such, the technique is capable of depicting the evolution of recurrent variability, unlike canonical EOF analysis which only identifies the mature-phase spatial structure, i.e., the pattern (and not mode) of variability. It yields the characterization of secular warming (through a nonstationary secular trend) and natural variability from a single analysis. The present study pursues the characterization of global SST variability also in the basin realm, i.e., without prejudicing the analysis with an *a priori* basin preference –as in Guan and Nigam (2008), who analyzed the Pacific basin variability, while, Guan and Nigam (2009) analyzed the Pacific-unrelated variability in the Atlantic basin.

Datasets and analysis methods are discussed below in section 3.2. The spatial distribution of the climatological summer monsoon rainfall, circulation, and associated rainfall standard deviation is described in section 3.3. The principal components from the primary analysis – the rotated extended-EOFs of the seasonal SST anomalies in the 118-year period extending from January 1900 to February 2018 – are presented in section 3.4. Summer monsoon rainfall regressions of the SST variability modes, extracted from the spatiotemporal analysis, are documented in section 3.5. The potential predictability of summer monsoon rainfall from the SST modes at various seasonal lead times is quantitatively assessed in section 3.6, while hindcast validation over an independent period is performed in section 3.7. A real-time verification of the

2019 summer monsoon forecast, developed using the SST-based strategy, along with intercomparison with other statistical and dynamical model forecasts from leading climate prediction centers is presented in section 3.8. Concluding remarks, including implications of this statistical prediction strategy in augmenting operational forecasting of summer monsoon rainfall and its hydroclimate impacts, follow in section 3.9.

3.2 Datasets and analysis methods

The present analysis is based on seasonal resolution data. Seasonal data are constructed by averaging monthly data over their respective 3-month boreal definitions, namely: winter is the mean of December, January and February, spring is the mean of March, April and May, summer is the mean of June, July and August, and autumn/fall is the mean of September, October and November.

3.2.1 Observed sea surface temperature

The analysis uses the UK Met Office's (UKMO) Hadley Centre Sea Ice and Sea Surface Temperature dataset, HadISST 1.1 (Rayner et al. 2003) , globally available at monthly 1º resolution (https://www.metoffice.gov.uk/hadobs/hadisst/). Seasonal SST anomalies are constructed by removing the long-term seasonal means. For computational efficiency, the seasonal anomalies are re-gridded to a 5º by 2.5º longitude-latitude grid.

3.2.2 Observed sea level pressure and winds

The study utilizes the National Center for Environmental Prediction (NCEP) reanalysis (Kalnay et al. 1996) to characterize the circulation associated with the

summer monsoon, namely, the mean sea level pressure (MSLP) and the 925-hPa winds. This reanalysis dataset is a global retrospective analysis of atmospheric fields obtained via the recovery of land surface, ship, rawinsonde, pibal, aircraft, satellite, and other data, followed by quality controlling and data assimilation. It is available at monthly resolution on a 2.5° x 2.5° global grid at 17 pressure levels from January 1949 (http://iridl.ldeo.columbia.edu/SOURCES/.NOAA/.NCEP-NCAR/.CDAS-1/.MONTHLY).

3.2.3 Observed precipitation

The Global Precipitation Climatology Centre (GPCC; Schneider et al. 2018) monthly data product, version 8, at a 0.5° x 0.5° spatial resolution is used in the present study. This precipitation data set (provided by Deutscher Wetterdienst, the German Meteorological Service, from their website at https://doi.org/10.5676/DWD_GPCC/FD_M_V2018_050) is a land-surface monthly precipitation dataset derived from an expanded set of 79,200 stations worldwide which feature at least 10 years of records for the period January 1891–December 2016.

3.2.4 Enabling SST analysis

Seasonal SST anomalies in the global domain (20ºS–80ºN, 0º–360º) are analyzed during the winter 1900–winter 2017/18 period using the Extended Empirical Orthogonal Function (EEOF) technique (Weare and Nasstrom 1982). The EEOFs are rotated using the Varimax criterion (Kaiser 1958; Richman 1986). The number of modes to be rotated and the sampling window width were determined by weighing for the physicality of the obtained modes of SST variability using biological marine

recruitment records and also by using observational analog count technique (A. Sengupta et al. 2019, submitted); in all, SST anomalies were staggered from -2 to 2 seasons, for a 5-season sampling window for the EEOF analysis, and then 11 modes were rotated. The SST principal components (PCs) are smoothed, when noted, using the LOESS filter (Cleveland and Loader 1996) with a 10% span window (LOESS-10%; i.e., with the window span being 10% of the 1900–2017 period, or, ~12 year), which suppresses the sub-seasonal-to-interannual fluctuations and makes the decadal variability more prominent. The raw and smoothed PCs, the name of the associated mode of SST variability and corresponding explained variance are discussed later in section 4.

3.2.5 Monsoon rainfall reconstruction from contemporaneous and antecedent SST anomalies

Linear, contemporaneous, seasonal regressions of the summer monsoon rainfall on the extracted global SST PCs in the common period 1901–2016 constitute the building blocks for the rainfall reconstruction from contemporaneous SST anomalies – the N = 0 case. Three other schemes are explored for the reconstruction of summer rainfall from preceding seasonal SST anomalies:– from the antecedent spring SST anomalies (the N = -1 case), from the preceding winter SST anomalies (the N = -2 case), and from the previous fall SST anomalies (the N = -3 case). For these three cases, temporally lagged regressions of summer rainfall on the antecedent season SST PCs in the historical period (1901–2016) form the building blocks of the reconstruction. A similar strategy was used to reconstruct tropical cyclone counts in the Atlantic sector

(Nigam and Guan 2011) and precipitation variations over the Great Plains (Nigam et al. 2011). The SST PCs are temporally orthogonal (assured by the rotated extended-EOF analysis method). Multiplication of each time-dependent SST PC with its time-independent summer rainfall regression pattern and summing the 11 modal contributions yield the summer rainfall anomalies for the reconstruction. Seasonal rainfall anomalies were reconstructed for the 59 summers of the post-International Geophysical Year (IGY) period, 1958–2016. The SST-based rainfall reconstruction is assessed at each land grid point by the temporal standard deviation (SD) and correlation statistics; the former evaluates the amplitude of the variability in the reconstructed rainfall, while the latter assess the temporal coherence of the reconstructed rainfall anomalies with corresponding observations.

3.2.6 Monsoon rainfall hindcast strategy

Hindcasts are developed for an independent period of 8 summers from 2009 to 2016. The building blocks for the hindcasts are the temporally lagged regressions of summer rainfall on the antecedent (spring, N = -1; winter, N = -2; and autumn/fall, N = -3) seasons' SST PCs but over a 108-year development period from 1901–2008 summers. In other words, the hindcast period (2009–2016) is fully independent of the regression training period (1901–2008). The SST principal components (in the hindcast period) are multiplied by their time-independent lagged seasonal rainfall regressions obtained in the training period, generating the summer monsoon rainfall hindcast. Given the use of EEOF SST PCs, the hindcast strategy is illustrated in Fig. 3.1, where a 5-season long sampling window width is deployed. The SST PC at t=t_o is determined using SST information from t_o−2 to t_o+2 seasons. For the hindcast period, only

antecedent SST PC (t=t_o) is used to reconstruct rainfall at t_o+3 seasons (i.e., 3 seasons later). The scheme does not utilize any rainfall data for the hindcast period and, therefore, shifts from reconstruction to a prediction problem.

3.3 Monsoon climatology

3.3.1 Summer rainfall and circulation

The spatial distributions of summer [June–August (JJA)] mean monsoon rainfall and associated sea level pressure and low-level circulation are displayed in Fig. 3.2a. The salient feature of the seasonal circulation during the summer monsoon is the cross-equatorial southeasterly flow that ultimately arrives as southwesterly winds (~10–12 m/s) over the Indian subcontinent. This flow structure is consistent with the meridional pressure gradient, set up due to the presence of a low-pressure center over northern India (e.g., the 1000-hPa isobar in Fig. 3.2a) and the Mascarene High in the southern Indian Ocean. Prior studies (Hoskins and Rodwell 1995; Slingo et al. 2005) have noted that the orography of the north-south oriented East African Highlands aid in the formation of the southwesterly monsoonal flow. The summer monsoon brings copious amounts of rain to South Asia, with the populous and agrarian Indo-Gangetic Plain recording ~8–10 mm/day over the JJA season. Summer rainfall maxima (~18–20 mm/day) occur over the west coast of India, parts of northeast India lying in the Himalayan foothills, and along the west coast of Myanmar. The regions of maxima reflect the interaction of monsoonal circulation with orography, namely the Western Ghats and the Himalayas for India and the Arakan mountain range in case of Myanmar. Over central India and Gangetic West Bengal, the rainfall is also large (~10 mm/day).

Southeastern peninsular India receives much less rainfall in comparison (~2–4 mm/day) as it remains in the rain-shadow region of the Western Ghats, which forms an orographic barrier effectively shielding the region from the moisture-laden southwesterly winds. The relatively weaker monsoonal flow (~5–8 m/s) over the Indochina Peninsula brings impressive rains (> 8 mm/day) to Southeastern Asia. Over eastern and southern China, the mean flow is southerly in nature and of much lesser magnitude (~2–4 m/s); the pre-Mei-yu and Mei-yu rainfall in this sector peaks in late spring, i.e., before the advent of the South Asian summer monsoon (Sengupta and Nigam 2019; their Fig. 1).

3.3.2 Interannual variability of summer rainfall

The interannual variability of the summer (JJA) monsoon rainfall is estimated from the standard deviation of the summer rainfall (Fig. 3.2b). The SD over the Ganges and Brahmaputra river basins (marked in red, Fig. 3.2b) is 2–4 mm/day, where the climatological summer rainfall is 8–10 mm/day. The summer rainfall SD over the western coasts of India and Myanmar is ~2–4 mm/day against a climatology of 18–20 mm/day. SD of summer rainfall is also large (> 1.5 mm/day) over Southeast Asia and eastern China. Over northwestern India, summer rainfall is seemingly less variable but not when viewed to its regional climatology, for example, SD values are 1.5–2.0 mm/day against a background climatology of 2–4 mm/day. Rainfall over southeastern peninsular India exhibits less variability in summer (~0.5–1.0 mm/day); this region is a predominantly a winter monsoon (October–December) area.

3.4 Spatiotemporal analysis of global SST variability

Assessment of the potential predictability of monsoon rainfall is rooted in the analysis of natural variability and the secular warming trend in global SSTs in the 20th century and early 21st century. By focusing on spatial and temporal recurrence in pattern recognition, the present analysis identifies the recurrent modes of SST variability – interannual, decadal-multidecadal, and the nonstationary secular trend – all without any advance filtering (and potential aliasing) of the SST record. This rotated EEOF analysis yields eleven global ocean modes whose temporal evolutions was shown earlier by their PCs in Fig. 2.1 of Chapter 2. The non-linear secular warming trend is the leading mode, i.e., it explains the largest percentage of SST variance (16.4%) over the analysis period. The variability of SSTs in the Pacific Ocean is identified by six modes, ranging from interannual to decadal-multidecadal timescales. Among them, the rich spectrum of ENSO variability is captured by four underlying modes – ENSO growth and ENSO decay (representing canonical variability), non-canonical ENSO, and the biennial variability. Pacific decadal variability is resolved into two modes, the Pan-Pacific and the North Pacific. The Atlantic Ocean SST variability is identified by four modes with decadal-to-multidecadal timescales – the Atlantic Multidecadal Oscillation (AMO), Atlantic Niño, the low-frequency North Atlantic Oscillation (LF-NAO), and the Subarctic decadal variability.

3.5 Impact of SST variability modes on summer monsoon rainfall

The individual influence of the natural variability and secular trend modes of SST variability on the summer (JJA) monsoon rainfall is shown in Fig. 3.3. The impact

is obtained from linear, contemporaneous regressions of rainfall on the summer PCs of the associated SST modes for their common period 1901–2016. Of notable interest is the influence of ENSO on the South Asian summer monsoon rainfall distribution, which is captured in Fig. 3.3a-d. In the development year of an emerging El Niño episode, there is a large rainfall deficit over the entire subcontinent (Fig. 3.3a). The regressions are ~ -0.6 mm/day per SST-index unit in the Indo-Gangetic Plain, which translates into a negative monsoon rainfall signal of ~ -1.2 mm/day for a strong El Niño episode (ENSO growth PC amplitude of ~2). Comparison with the background regional climatology (~ 8 mm/day; cf. Fig. 3.2a) suggests that the anomalies are significant, being ~15% of the climatology. Likewise, the anomalies over peninsular India are ~ -0.4 mm/day per index unit, or ~ -0.8 mm/day for a strong episode, where the regional JJA climatology is 6 mm/day (cf. Fig. 3.2a). ENSO's impact in the summer following the peak warm phase (Fig. 3.3b) is more modest and comprised of a rainfall dipole with a deficit (~ -0.4 mm/day per index unit) in the eastern subcontinent and surplus along the west coast of India (~ +0.4 mm/day per index unit). The non-canonical ENSO and the biennial variability modes also generate significant negative rainfall signal (Fig. 3.3c-d) along the west coast and positive anomalies over parts of eastern India in their warming phases with the former mode been more like the canonical ENSO mode in its growing phase in the distribution of positive and negative rainfall anomalies.

Summer rainfall regressions of the decadal-multidecadal modes of natural variability in the Atlantic (Fig. 3.3e-h) and Pacific (Fig. 3.3i-j) are also shown. All of these modes force rainfall anomalies of limited extent along regions such as the Western coastal plains and the Gujarat Plains, over the Deccan Plateau between the

Godavari and Krishna Rivers, and to its east along the Eastern coastal plains, over the Indo-Gangetic Plains and coastal Bangladesh and Myanmar. The Atlantic Niño has some impact over northern and southern Myanmar (+0.2 to +0.4 mm/day per SST-index unit), while, the low-frequency NAO has deficits along the west coast and northeastern states of India (~ -0.4 mm/day per SST-index unit). Significant anomalies (~ 0.4 mm/day per SST-index unit) for the AMO and Subarctic modes are mostly focused along southern Gujarat and coastal Maharashtra, with rainfall surplus (deficit) associated with positive AMO (Subarctic DV) events. Of the two Pacific decadal variability (PDV) modes, the PDV Pan-Pacific has a stronger impact (Fig. 3.3i), with surplus rainfall (~ +0.2 mm/day per SST-index unit) along the western coast to the northwestern states of India, and suppressed rainfall (-0.4 to -0.8 mm/day per SST-index unit) along coastal Bangladesh and Myanmar. The North Pacific DV (Fig. 3.3j) has notable positive rainfall signals (~ +0.4 mm/day per SST-index unit) in northern India and southern Myanmar.

The precipitation change associated with the SST secular trend component over the South Asian region is shown in Fig. 3.3k. Along the western coast, positive precipitation anomalies (~ 0.6 mm/day per SST-index unit) are notable, especially over southern Gujarat and coastal Maharashtra. The southwestern coast (comprising the state of Kerala) and parts of the Ganges-Brahmaputra basins, on the other hand, exhibit negative precipitation anomalies (~ -0.6 mm/day per SST-index unit).

3.6 South Asian monsoon rainfall reconstruction

3.6.1 Using all 11 global modes of SST variability

The potential skill of the SST-based monsoon rainfall reconstruction is assessed at lead times of 3 seasons (i.e., from the previous fall SSTs; N = -3), 2 seasons (from the antecedent winter SSTs; N = -2), and 1 season (from the previous spring SSTs; N =-1), and from contemporaneous SSTs (i.e., using the summer SSTs; N = 0) in Fig. 3.4. Rainfall over 59 summers is reconstructed for the post-IGY period, 1958–2016. Reconstruction is undertaken in this case with both contemporaneous and SST-leading rainfall regressions of all the eleven modes of global SST variability. The top panel shows the SD of the reconstructed seasonal rainfall anomalies in the boreal summer across the four schemes. The SD values are found to be 1.0–1.5 mm/day in the northern Gangetic Plain, and 1.5–2.0 mm/day in western peninsular India (Fig. 3.4a-d). The amplitude of the variability from the reconstructed summer rainfall is assessed in the middle panel from the display of the ratio of reconstructed and observed SDs. The N = 0, N = -1, and N = -2 panels show large regions of northern, eastern, and southern peninsular India with SD ratios greater than 0.4–0.6 (cf. Fig. 3.4f-h), i.e., 40–60% of the observed variability is captured in the reconstructions. The ratio of the SDs is smaller in the 3-season SST-lead reconstruction scheme (Fig. 3.4e), with values ~0.4 in eastern and southern India; SD ratio in northwestern India is below the shading threshold. Temporal correlation between the reconstructed and observed summer rainfall anomalies is displayed in the lower panel of Fig. 3.4 to assess if the SST-based reconstruction strategy also yields the correct phase of each summer's anomaly. The SST-based 3- (Fig. 3.4i) and 2-season-lead rainfall reconstructions (Fig. 3.4j) exhibit

correlations larger than 0.4 over large swaths of the Gangetic Plain (all across the Ganges and Brahmaputra river basins), peninsular India, and southern Myanmar. Correlations are found to be greater (> 0.5) over these same regions for the N = -1 (Fig. 3.4k) and N = 0 (Fig. 3.4l) schemes. The present analysis thus provides a quantitative assessment of the SST-based potential predictability of monsoon rainfall at various seasonal lead times.

3.6.2 Using the six Pacific and secular warming trend modes of SST variability

An inspection of the relative contribution of an individual ocean basin, namely the Pacific, towards the overall rainfall reconstruction is presented in Fig. 3.5. For N = 0, N = -1, and N = -2 schemes, SD values of reconstructed rainfall are found to be 0.5 mm/day across the Indian mainland, with values reaching 1.0–1.5 mm/day in the northern Gangetic Plain and western coastal regions (cf. Fig. 3.5b-d). For the 3-season SST (Pacific only)-leading reconstruction (Fig. 3.5a), the SD values are even smaller, especially in southern India. Comparison between reconstructed and observed summer rainfall SDs from the reconstructed summer rainfall, via their SD ratio (Fig. 3.5; middle panel), indicates that the SD ratios are of the order of 0.4–0.6 in the core monsoon regions – Gangetic Plain and southern peninsular India. A comparison with amplitude reconstructed using all eleven SST modes (cf. Fig. 3.4; middle panel) reveals the Pacific as the more influential basin; SD ratios are robust even while using the influence of only seven out of the eleven SST modes. In terms of the temporal correlation between the reconstructed and observed summer rainfall anomalies, the 3- and 2-season SST-lead rainfall reconstructions (Figs. 3.5i, and 3.5j) have values of 0.3 in the

Gangetic Plain and southern peninsular India (i.e., 0.1 smaller than corresponding correlations using all the 11 modes in Fig. 3.4i-j). Correlations are found to be higher (~0.4) over similar regions, including southern Myanmar, for the 1-season SST-lead and contemporaneous SST-based rainfall reconstructions (Fig. 3.5k-l). This assessment indicates the strong impact that the main modes of global SST variability have on the seasonal summer monsoon rainfall, and that the modes from the Pacific basin, including the Trend mode, contribute the most to the modal reconstruction.

3.7 South Asian monsoon prediction skill assessment

The predictive skill of the SST-based modes for the summer monsoon rainfall is explored in this section. This prediction exercise uses the modal SST-based summer rainfall regressions obtained for the period, 1901–2008, in order to predict the rainfall anomalies for the period 2009–2016; in this way, the prediction period is fully independent of the regression training period for a definitive assessment of the SST-based potential predictability of seasonal monsoon rainfall. The assessment of the prediction of the summer monsoon rainfall anomalies is shown in Fig. 3.6. The SD of the predicted summer rainfall is of the order of 1.0–1.5 mm/day in the northern Gangetic Plain, western coast of India and in parts of southern Myanmar for the 2- and 1-season SST-lead hindcasts (Fig. 3.6b-c); over other parts of India, SD values are ~0.5 mm/day. Fig. 3.6a reveals that SD is weaker over southeastern peninsular India for the 3-season SST-lead hindcast, that is, the SD ratio of hindcast rainfall compared to the observed over southern peninsular India is 0.6–0.8, whereas the SD ratio is > 0.8 over eastern India and southern Myanmar (Fig. 3.6d). The SD ratio for the 2-season SST-

lead hindcast (Fig. 3.6e) is also large over southern peninsular India (~0.8–1.0), Gangetic Plain, and, parts of western and central India (~0.6). The skill of amplitude reconstruction is seemingly the largest with the 1-season SST-lead hindcast (Fig. 3.6f); for example, the SD ratio over southern peninsular India and the Gangetic Plain is 0.8–1.0 (i.e., explaining 80–100% of the observed variability). Even for parts of northwestern India, a climatologically dry region, this scheme has considerable prediction skill (~0.6).

The temporal coherence of the hindcast rainfall anomalies with the observed anomalies is assessed in the lower panel of Fig. 3.6. Consistently high correlation values are found over expansive stretches of peninsular India (~0.6), Gangetic Plain (~0.4–0.6), and western India (~0.4) for the 2-season (N = -2; Fig. 3.6h) and 1-season (N = -1; Fig. 3.6i) SST-lead hindcasts. In the case of the 3-season (N = -3; Fig. 3.6g) SST-lead hindcasts, the correlations are slightly lesser, yet impressive (~0.4) in southern peninsular India and the Gangetic Plain. The SST-based rainfall prediction scheme appears to be not as robust in the northeastern Indian states, as indicated by the out-of-phase relationship between the hindcasts and the observations.

A more regional assessment of the predicted summer rainfall anomalies over the four meteorological subdivisions of India—Central, Northwest, South peninsular, and Northeast—is plotted in Fig. 3.7. The geographical location of these four subdivisions is shown in Fig. 3.7a. Over Central India (Fig. 3.7b), the observed rainfall anomaly exceeds 0.2 mm/day (~0.3 mm/day) during the summer of 2013 and is deficient for the summers of 2009 (~ -0.10 mm/day) and 2014 (~ -0.15 mm/day). The suppressed rainfall is not unexpected, given the major non-canonical El Niño episode

of 2009–10 and the weak El Niño episode of 2014–15 (cf. Fig. 3.3a, 3.3c for impacts of ENSO variability modes on Indian summer rainfall). The observed rainfall time series is correlated with the 1-season SST-lead hindcast at +0.65 and with the 2-season and 3-season lead ones at +0.54 and +0.35 respectively. The rainfall deficit in Northwest India (Fig. 3.7c) is even greater, being of the order of -0.2 mm/day for the two El Niño episodes of 2009–10 and 2014–15. This deficit is in line with the significant footprint of the ENSO-related rainfall anomalies in the northern Gangetic Plain and the northwestern states of India. The time series of observed anomaly is correlated with the 1-season, 2-season, and 3-season SST-lead hindcasts at +0.48, +0.51 and +0.38 respectively. The rainfall prediction using antecedent SSTs with different lead times is most impressive over South peninsular India (Fig. 3.7d); correlation values are the highest, being +0.72, +0.66 and +0.46 respectively for the three hindcast schemes. The SST-based monsoon rainfall strategy appears to be not as competitive over Northeast India (Fig. 3.7e); correlation values for the 1-season, 2-season and 3-season SST-lead hindcasts are -0.15, -0.20 and +0.02 respectively. The low correlation values for this region can be attributed to the lack of reliable gridded rainfall data (due to the complex terrain and sparseness of stations), which affects the SST-rainfall training period regressions — the "building blocks" of the observationally rooted prediction scheme.

3.8 Forecast and verification of the 2019 summer (JJA) monsoon

The forecast for the geographical distribution of the 2019 summer monsoon rainfall anomalies (based on the SST-based statistical model presented above) and its verification are shown in Fig. 3.8, with respect to a base period of 1951–2000. The

forecast is generated from regressions of observed GPCC ver. 8 precipitation on the SST principal components (extracted in Chapter 2) over the period 1901–2016. The forecast verification is generated from IMD's gridded rainfall dataset. An intercomparison of the University of Maryland (UMD) SST-based statistical forecast with two other statistical forecasts — from Skymet and AccuWeather, and two dynamical forecasts — from IRI Columbia and APEC Climate Center are also documented in the same figure. The UMD forecast (Fig. 3.8b) called for significantly below-normal rainfall in Ganges and Brahmaputra basins (states of Uttarakhand, Uttar Pradesh, Bihar, Jharkhand, Assam, Arunachal Pradesh, and eastern Bangladesh), and above-normal rainfall in western India, notably, coastal Maharashtra and southern Gujarat. The forecasted rainfall deficit in the Ganges and Brahmaputra basins is attributed principally to the contributions from the ENSO principal components, both canonical and non-canonical. The above-normal rainfall over southern Gujarat and coastal Maharashtra has its origin in the regressions on ENSO-decay, biennial, and the SST secular trend principal components (cf. Fig. 3.3).

The IMD-based forecast verification (Fig. 3.8a) has broadly similar spatial structure (although larger amplitude) with the UMD forecast, characterized by rainfall deficits in the Ganges–Brahmaputra river basins, and surplus over western coastal India and northwest India. The Skymet statistical forecast (Fig. 3.8c) captures some aspects of the observed rainfall distribution. Notable departures include an expansive rainfall deficit over western and southern India and surplus in the upper Gangetic Plains. The AccuWeather forecast (Fig. 3.8d) departs the most from the observed rainfall distribution. Summer rainfall is significantly underestimated in northwest India and

overestimated to the east (eastern Gangetic Plains and northeast India). The IRI probabilistic forecast (Fig. 3.8e) underestimates the observed rainfall anomaly even more over eastern and western coastal India. The APEC Center's dynamical forecast (Fig. 3.8f) for the 2019 summer monsoon is reasonable but for the lack of positive anomalies along the western coast. The forecast also has other deficiencies, notably, the absence of negative anomalies over northeastern India.

3.9 Concluding remarks

The southwest monsoon brings bountiful rain to South Asia in summer and is widely recognized as the "backbone" of the economy of a billion-plus people living in the Indian subcontinent. The differential heating of the land as compared to the surrounding ocean during boreal spring into summer produces a meridional temperature gradient and sets up a cross-equatorial flow at the surface. The resulting low-level, moisture-laden, southwesterly winds are instrumental for onshore moisture influx; flux convergence is, however, needed for rainfall, often aided by orographic interaction which produces convergent conditions, for example, in the Western Ghats along the west coast of India. SST variability in the global ocean is an influential driver of monsoon rainfall. SST-based summer rainfall prediction targets have, however, hitherto been unavailable because SST-rainfall linkages were generally investigated in a piecemeal manner that did not permit integration across the SST variability spectrum, and because most previous analyses did not consider temporal evolution in the characterization of SST modes. This motivated our observationally rooted analysis which focuses on quantifying the potential SST-based predictability of summer monsoon rainfall. Here we

- Adopt a statistical approach rooted in the innovative rotated extended-EOF spatiotemporal analysis of the 20^{th} -21^{st} century global SST variability. This provides a consistent characterization of the secular trend and natural variability in the global ocean SSTs.
- Document the characteristic influence of the modes of SST variability on summer monsoon rainfall. A key finding here is the dissimilar regional hydroclimate footprint depending on the type of the emerging ENSO episode.
- Show an impressive reconstruction of the observed seasonal rainfall anomalies in the post-IGY period from both contemporaneous as well as temporally leading SST modal predictors. A much larger SST-based prediction signal in summer monsoon rainfall is obtained in terms of amplitude and phase when SST evolutionary aspects are considered. An interesting finding here is the quantification of the extent of the relative contribution of the ocean basins on monsoon rainfall: Pacific SSTs are found to be more influential than the Atlantic ones.
- Demonstrate that the SST-based hindcast shows high prediction skill during the recent eight-year independent verification period. The *1-season* and *2-season* SST-lead time hindcasts explain 80–100% of the observed variability and exhibit high correlation values (~0.6) over key monsoon regions — the Indo-Gangetic Plain and peninsular India, indicating prospects for improved seasonal predictions.

The current prediction effort is closely linked to the operational seasonal

summer monsoon forecasting goals of the India Meteorological Department and seeks to establish an empirical benchmark for the evaluation of dynamical model forecast improvements. The present analysis is also encouraging for the investigation of the skill of dynamical models (e.g., the NCEP CFSv2) in predicting the SST-related summer monsoon rainfall variations over South Asia using the SST-based potential predictability targets. Intercomparison of the simulated SST modal structures and related precipitation (and circulation) regressions with their observational counterparts will facilitate identification of model shortcomings at the modal resolution, thereby, directly contributing towards model improvement efforts.

While this research improved the prospects for seasonal monsoon forecasting, it has not shed any light on the mechanisms that generate SSTs' influence on rainfall. SSTs can impact monsoon rainfall through several mechanisms, e.g., through upper-tropospheric wave propagation from remote tropical basins; via modulation of lower-tropospheric flow over regional orography; from modification of the regional meridional temperature gradient; and from remotely forced influences on the large-scale divergent environment over South Asia. The investigation of influence mechanisms and their relative roles would be clearly challenging for observational studies because of the inability to selectively suppress one or more mechanisms. Controlled modeling experiments would be needed to assess the mechanisms of SST influence on monsoon rainfall, but these were not undertaken as present-day models were found significantly deficient in their rendition of spatiotemporal variability of the South Asian summer monsoon rainfall distribution.

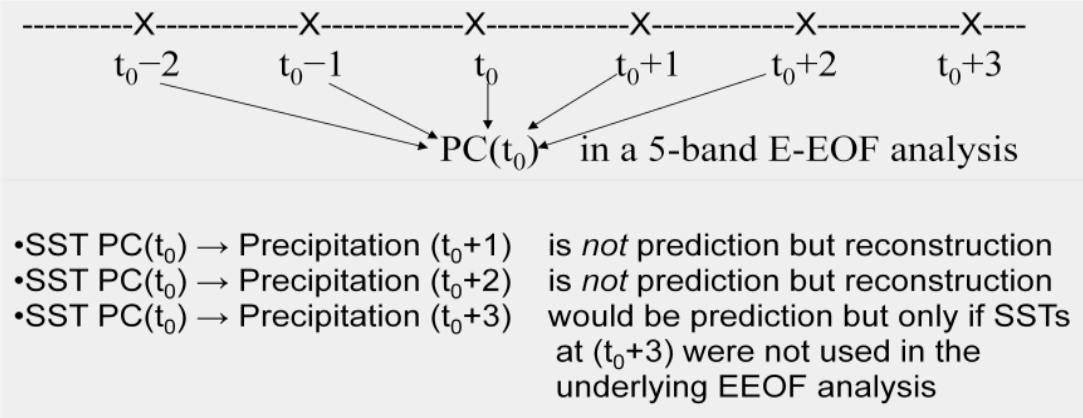

Figure 3.1. Schematic illustration of rainfall reconstruction and prediction in context of the Extended-EOF analysis where SST principal component at $t=t_o$ is determined using both antecedent and subsequent seasons' SST anomalies. The extent of seasonal outreach depends on the width of the sampling window which is 5- season long in the schematic (and in the undertaken Rotated EEOF analysis).

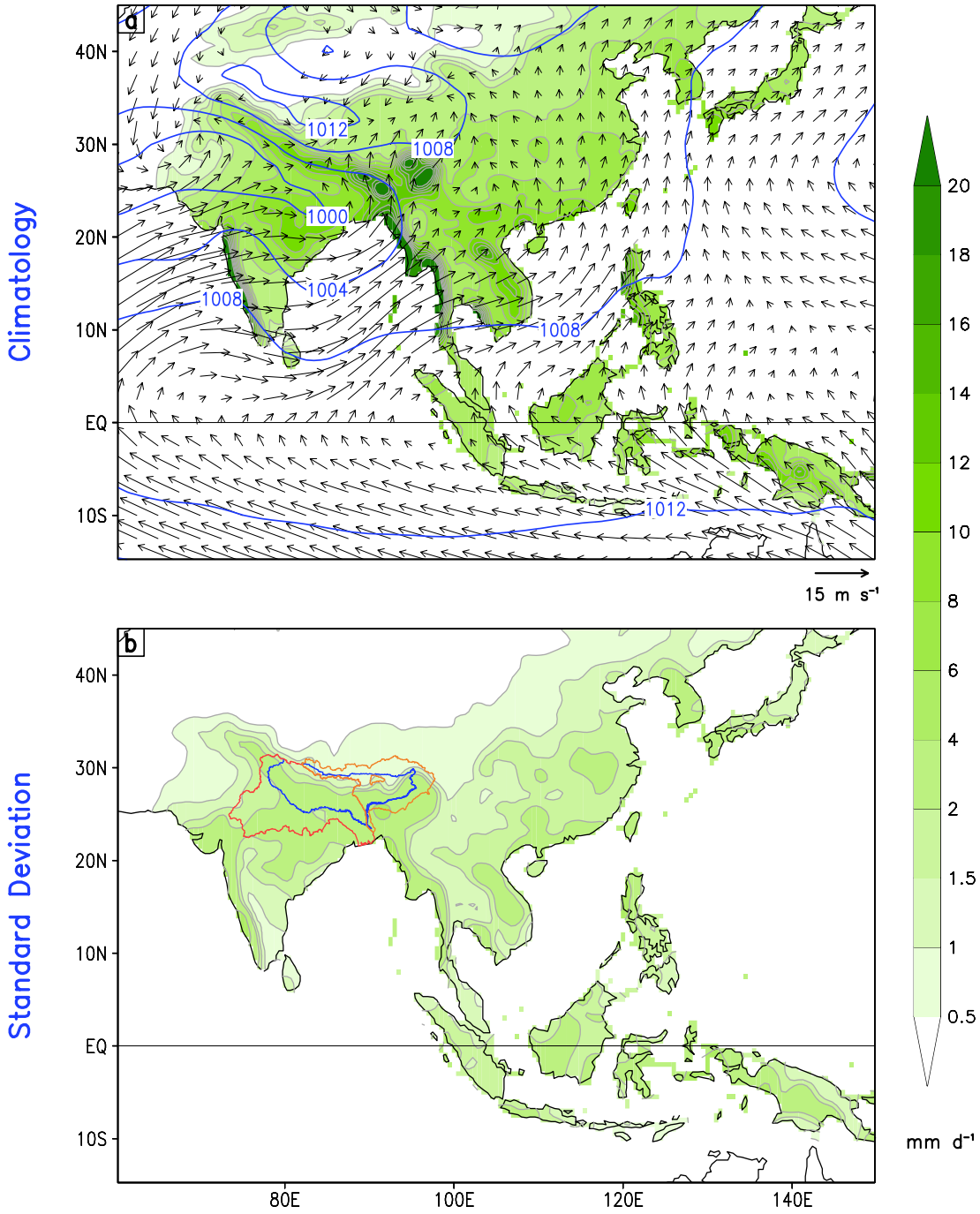

Figure 3.2. Climatological summer rainfall, associated circulation, and variability. (a) Seasonal mean rainfall (from GPCC ver. 8), 925-hPa vector winds and mean sea level pressure (MSLP; from NCEP Reanalysis) are shown for the summer (June-August) season. The period of analysis is 1958–2016. (b) Standard deviation of summer rainfall is also based on the GPCC ver. 8 dataset, for the same period. The Ganges and Brahmaputra river basins are demarcated in red in (b). For both the panels, contour interval for rainfall is 0.5 mm/day for values less than 2.0 mm/day, and 2.0 mm/day for higher values; shading threshold is 0.5 mm/day. The threshold for plotting wind vectors is 1.0 m/s; MSLP is contoured at intervals of 4-hPa. The rainfall fields are displayed after smoothing twice with the GrADS smth9 function.

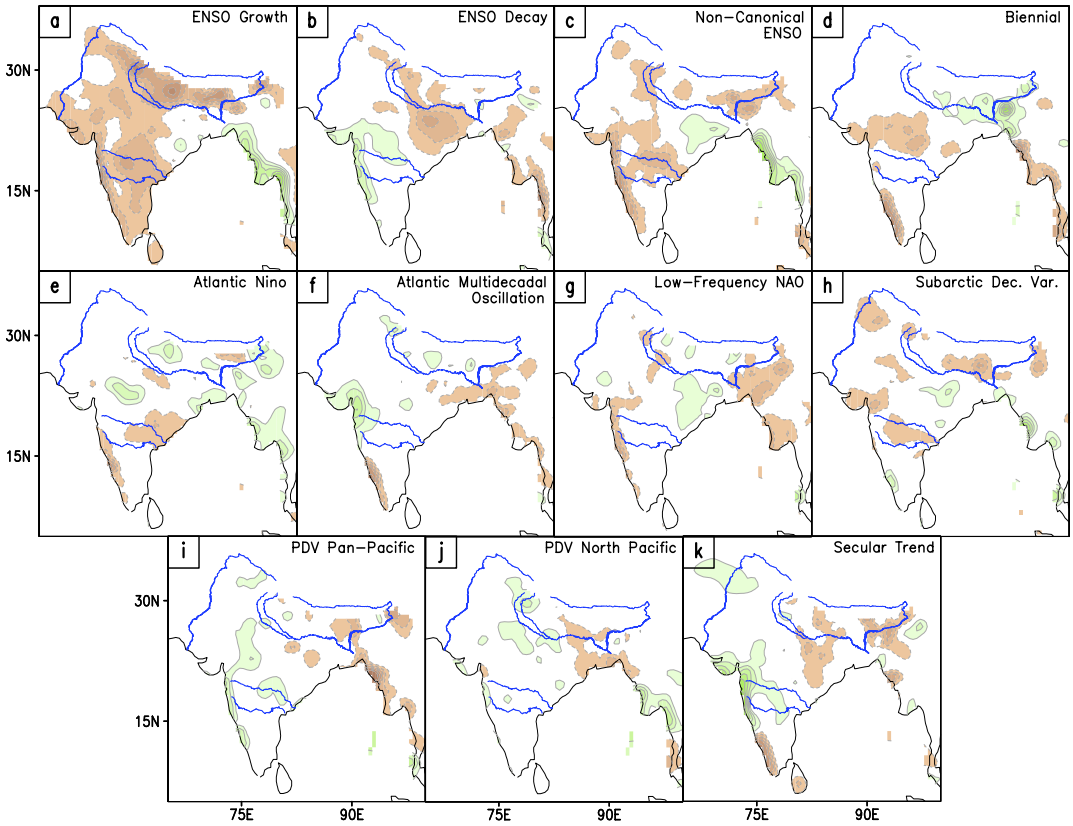

Figure 3.3. *Characteristic influence of the extracted modes of SST variability* (from extended-EOF analysis) on summer (June-August) rainfall. The influence is obtained from linear, contemporaneous regressions of the GPCC (version 8) summer rainfall on the individual principal components in the period 1901–2016. Contour interval is 0.2 mm/day per SST-index unit. Brown (green) shading denotes rainfall deficit (surplus); the zero contour is suppressed. The individual modal contribution to the rainfall anomaly for any summer can be obtained by multiplying the time-dependent PC amplitude for that summer with the time-independent rainfall regression pattern.

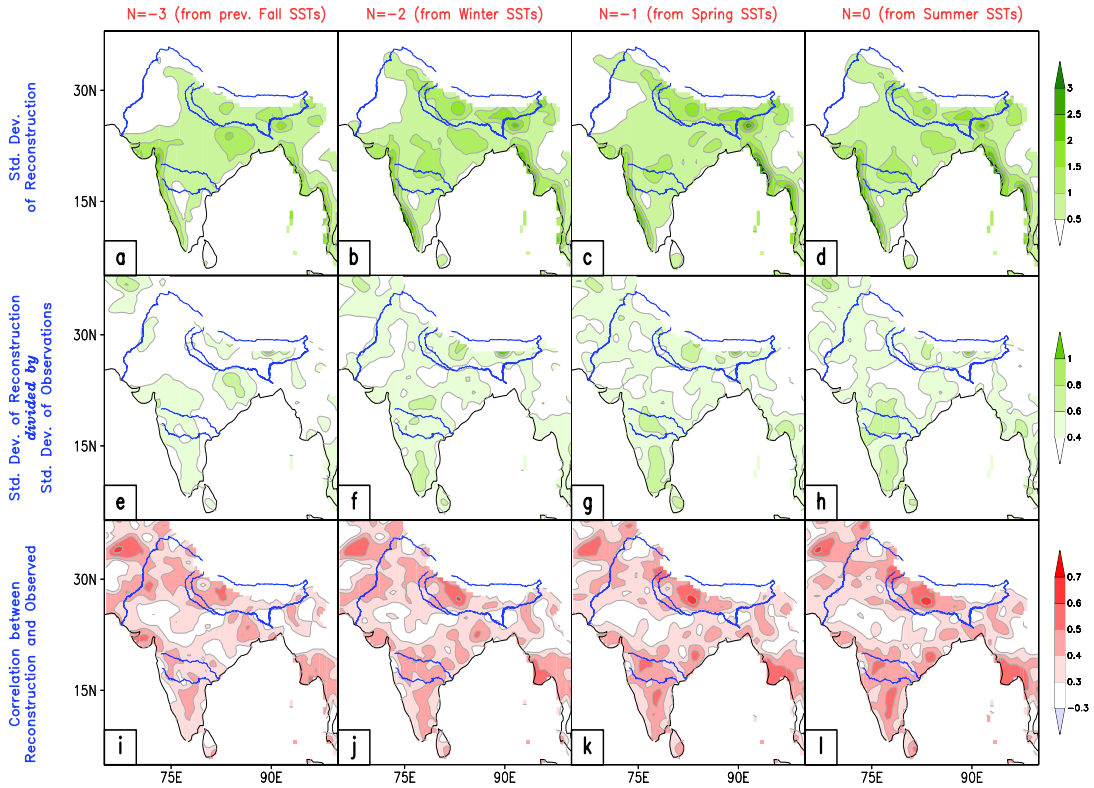

Figure 3.4. *Intercomparison of observed and reconstructed summer monsoon rainfall* anomalies from antecedent (N = -3, -2, -1) and contemporaneous (N=0) seasons' SST anomalies during the period 1958–2016. The building blocks for the reconstruction are based on the regressions of GPCC (ver. 8) summer rainfall on the SST principal components during the period 1901–2016. Top panel shows the standard deviation (SD) of the summer rainfall from modal SST-based reconstruction using 11 global modes. The extent of reconstruction, evaluated from the ratio of SDs, is shown in the middle panel. The temporal coherence of the observed and reconstructed summer rainfall anomalies is shown using correlations in the bottom panel. The SD contour interval and shading threshold is 0.5 mm/day. The SD Ratio is contoured at 0.2 interval when ≥0.4; shading when ≥0.4. The correlation field is shown at 0.1 interval when ≥0.4; shading when ≥0.4, as well. The fields are displayed after smoothing from 1 application of GrADS's smth9 function.

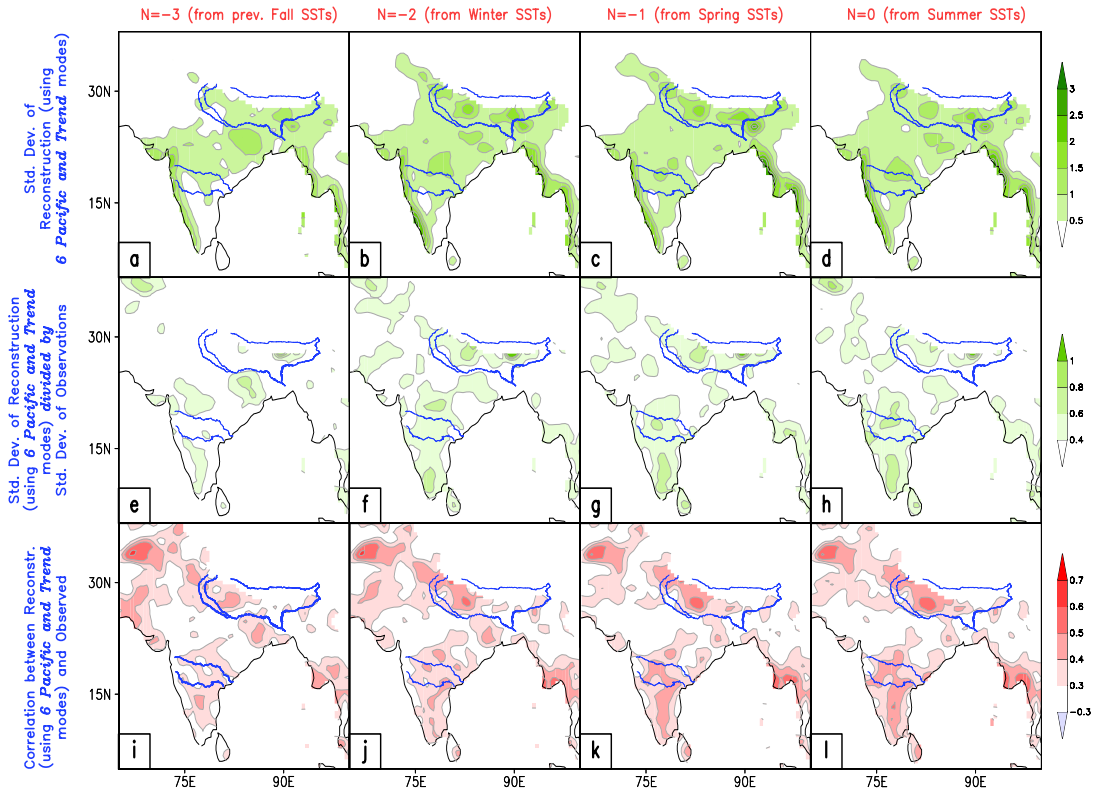

Figure 3.5. *Intercomparison of observed and reconstructed summer monsoon rainfall* anomalies from antecedent (N = -3, -2, -1) and contemporaneous (N=0) seasons' SST anomalies during the period 1958–2016. The building blocks for the reconstruction are based only on Pacific basin contributions, i.e., from the regressions of GPCC (ver. 8) summer rainfall on the principal components of the six Pacific-basin and secular warming trend modes during the period 1901–2016. Top panel shows the standard deviation (SD) of the summer rainfall from modal SST-based reconstruction using the 6 Pacific modes and the Trend mode. The extent of reconstruction, evaluated from the ratio of SDs, is shown in the middle panel. The temporal coherence of the observed and reconstructed summer rainfall anomalies is shown using correlations in the bottom panel. The contour interval and shading threshold are same as in Fig. 3.4. The fields are displayed after smoothing from 1 application of GrADS's smth9 function.

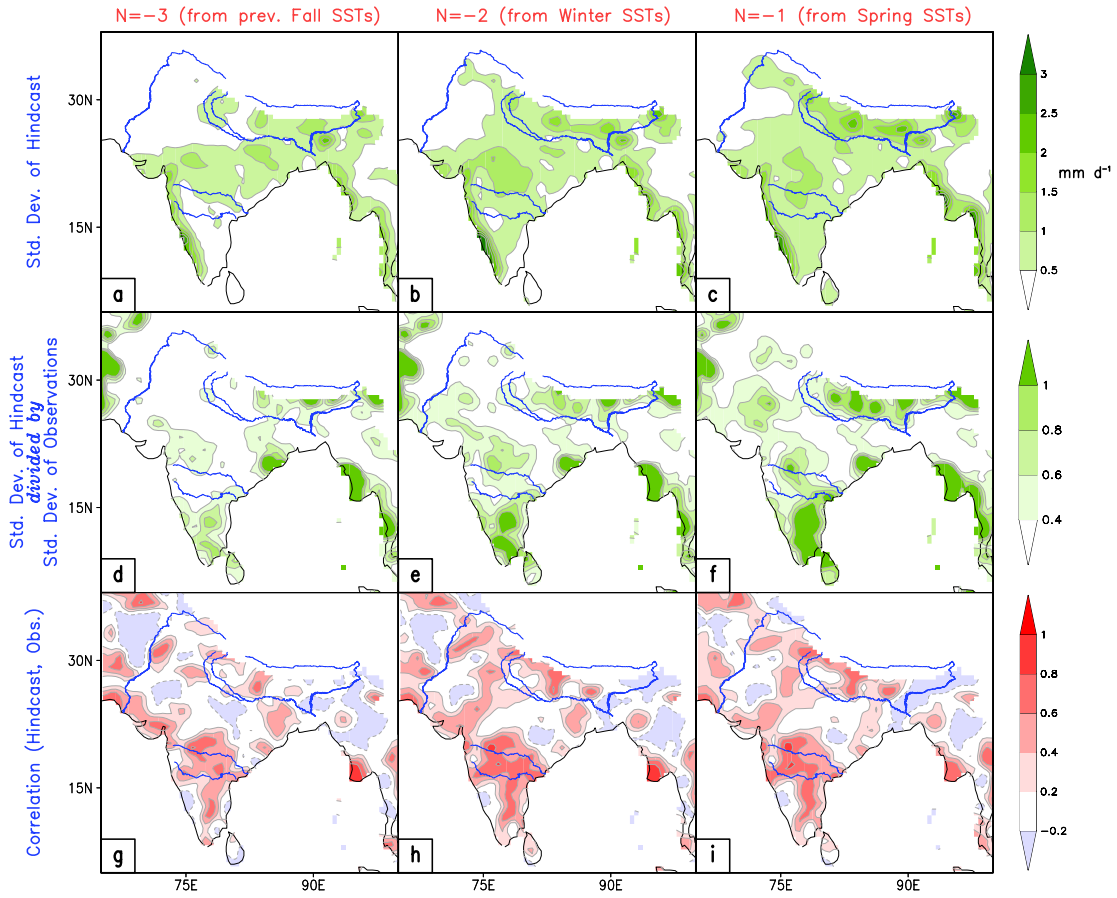

Figure 3.6. *Intercomparison of observed and hindcast summer monsoon rainfall* anomalies from antecedent (N = -3, -2, -1) seasons' SST anomalies during the period 2009–2016. The building blocks for the hindcast are based on the regressions of GPCC (ver. 8) summer rainfall on the principal components of the eleven global SST modes during the period 1901–2008. Top panel shows the standard deviation (SD) of the hindcast rainfall. The extent of amplitude hindcasted, evaluated from the ratio of SDs, is shown in the middle panel. The temporal coherence of the observed and hindcast summer rainfall anomalies is shown using correlations in the bottom panel. The contour interval and shading threshold for the top and middle panel are the same as the corresponding fields in Fig. 3.4. The correlation subplots are shown at a 0.2 interval when ≥0.2; shading when ≥0.2, as well. All fields are displayed after smoothing from 1 application of GrADS's smth9 function.

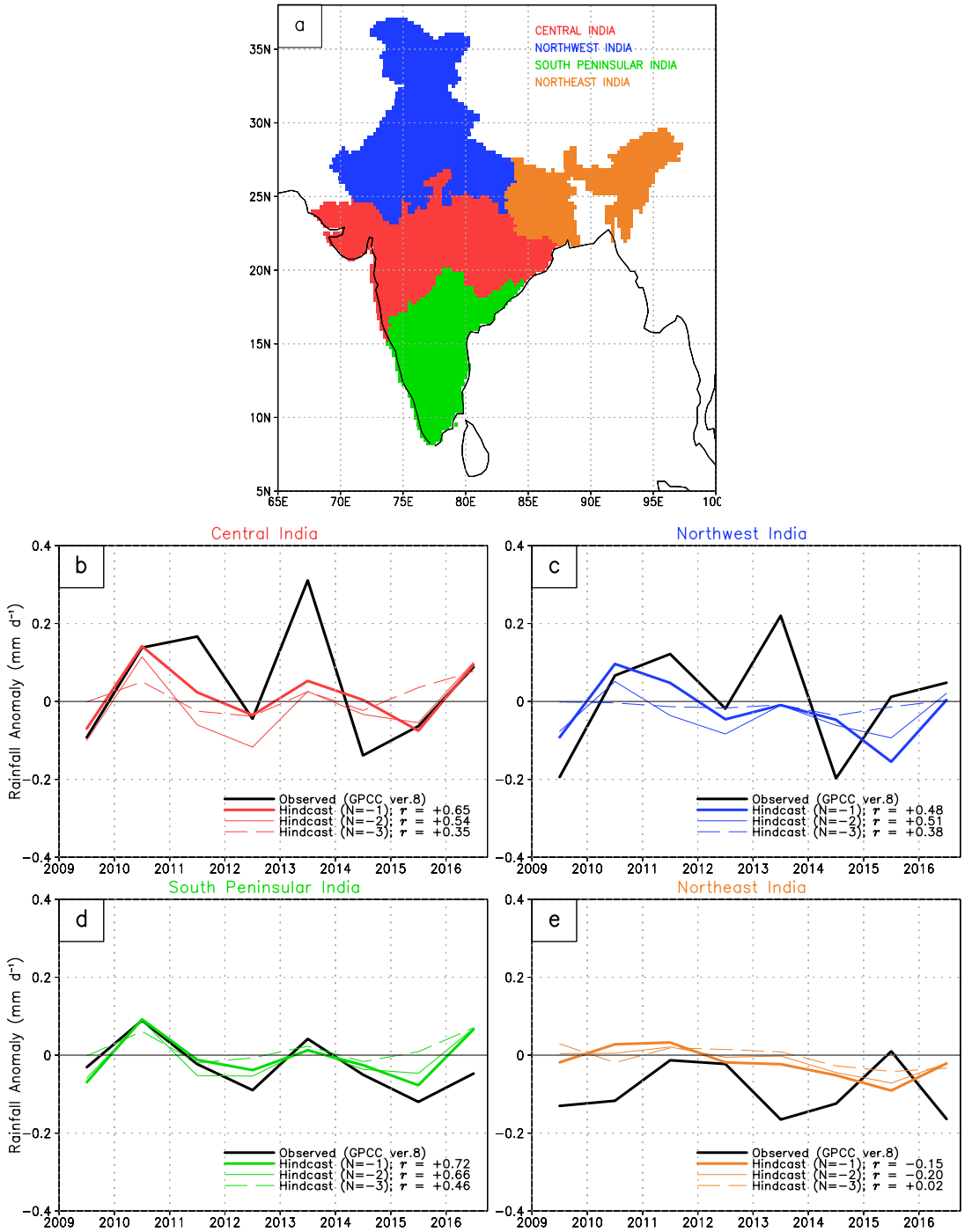

Figure 3.7. Time series of observed and hindcast summer rainfall anomalies during the period 2009-2016 over the four meteorological sub-divisions of India. The subdivisions are as follows: Central India, Northwest India, South Peninsular India and Northeast India, whose geographical location is shown in (a). Hindcast performance from 1-, 2-, and 3-season SST-lead is shown for these four subdivisions in (b)-(e). The correlation (*r*) between the observed and hindcast time series is noted next to each hindcast scheme.

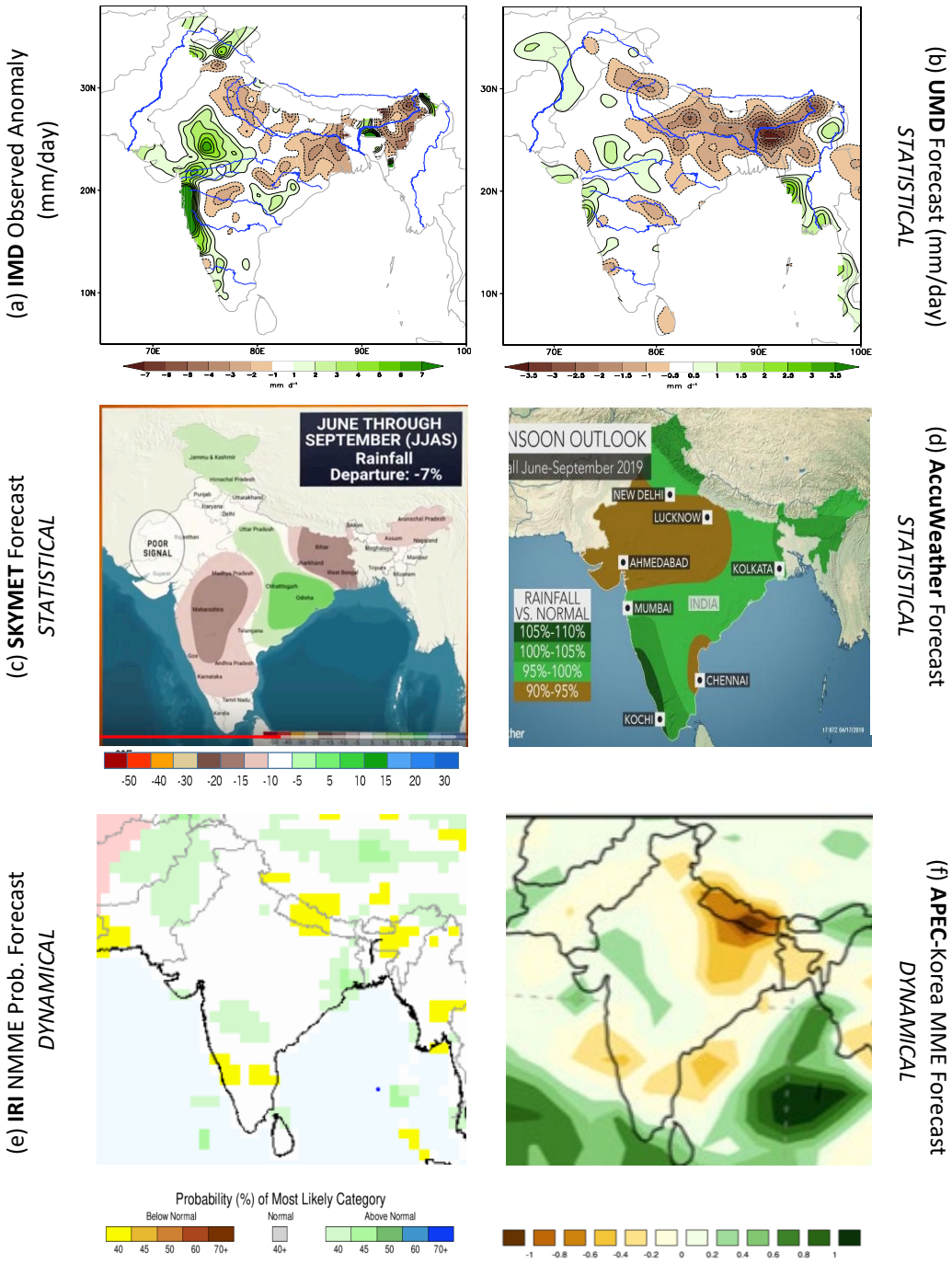

Figure 3.8. *Verification of the University of Maryland 2019 summer (JJA) monsoon forecast and comparison with other statistical and dynamical forecasts*. (a) The forecast verification is generated from the IMD gridded rainfall dataset. (b) The UMD SST-based experimental forecast is generated from regressions of the GPCC ver. 8 precipitation data on the SST PCs over the period 1901-2016. Green shading represents above-average rainfall while brown shading denotes below-average rainfall. The shading interval is 0.5 mm/day in the forecast and 1.0 mm/day in verification – all as indicated in the shading bar. (c)-(d) Statistical forecasts developed by Skymet and AccuWeather, respectively. (e)-(f) Dynamical forecasts generated by IRI Columbia and the APEC Climate Center (Korea), respectively.

Chapter 4: The Northeast Winter Monsoon over the Indian Subcontinent and Southeast Asia: Evolution, Interannual Variability, and Model Simulations

4.1 Background

Monsoons over South Asia are characterized by a southwest summer monsoon from June to September and a northeast monsoon (NEM) from October to December (OND). The boreal summer monsoon, which brings copious amounts of rainfall accounting for over 70% of the annual rainfall over India, has been more widely studied. However, southeastern peninsular India remains in the rain-shadow region of the Western Ghats, the orographic barrier along the west coast that shields the region from the moisture-laden southwest monsoon winds. The agricultural productivity in this region is largely dependent on the NEM rainfall, which supplies nearly 50% of the annual rainfall to southeastern peninsular India, Sri Lanka, and the neighboring seas (Kumar et al. 2007). The prospect of seasonal prediction along with its impacts on water re- sources and agriculture (the winter crops: Rabi in southern India and Maha in Sri Lanka) warrants a closer look at the winter monsoon and its variability.

Despite its significant agricultural and economic importance, the NEM has been considerably understudied relative to its summer monsoon counterpart. The India Meteorological Department forecasting manual (Srinivasan and Ramamurthy 1973) provided a detailed description of the NEM. Dhar and Rakhecha (1983) studied

monthly rainfall data for a 100-yr period (1877–1976) to investigate the association between the north- east and southwest monsoons over Tamil Nadu, India, and concluded that summer rainfall is negatively correlated with NEM rainfall. Matsumoto (1990) investigated variations in tropical wind fields and noted activation of the NEM during the end of October in the northern Indian Ocean sector. Singh and Sontakke (1999) examined the Indian postmonsoon rainfall features and its variability and attempted to extrapolate the future trend in rainfall fluctuations over a 10-yr period. Wang and LinHo (2002) noted a bimodal seasonal distribution of rainfall over Sri Lanka and Indochina with rainfall maxima in October–November. The in- terannual variation of late-autumn rainfall over Vietnam was discussed by Chen et al. (2012). NEM also influences the eastern coast of the Philippines (Akasaka et al. 2007); however, its onset and interannual variation do not show prominent fluctuations like those of the summer rainy season (Akasaka 2010).

The El Niño–Southern Oscillation (ENSO) phenomenon is perhaps the most studied mode of interannual climate variability since Bjerknes (1969) linked El Niño SST anomalies with basinwide sea level pressure variations (Southern Oscillation; Walker 1923). Over India, El Niño events have been associated with below-normal summer monsoon rainfall (Sikka 1980; Rasmusson and Carpenter 1983; Pant and Kumar 1997; Kumar et al. 2007). El Niño's impact on the NEM is, however, the opposite (Sridharan and Muthuswamy 1990; Suppiah 1997; De and Mukhopadhyay 1999; Jayanthi and Govindachari 1999), that is, above-normal rainfall. Contrary to the robust ENSO–NEM rainfall link over South Asia, the relationship between ENSO and

the East Asian winter monsoon (EAWM) undergoes low-frequency oscillation (Zhou et al. 2007) with a periodicity of about 50 years (He and Wang 2013).

ENSO is widely monitored using the Niño SST indices, for example, the Niño-3.4 index—the area- averaged SST anomaly in the equatorial central- eastern Pacific Ocean, computed, for example, using HadISST data (Rayner et al. 2003). The relationship between ENSO and the NEM has strengthened in the recent past (Zubair and Ropelewski 2006; Kumar et al. 2007), whereas the relationship between ENSO and the EAWM has weakened since the mid-1970s (Wang and He 2012). Wang et al. (2008) found that the Pacific decadal oscillation, whose negative phase leads to robust low-level temperature change over East Asia, modulates the ENSO–EAWM relationship. Sun et al. (2011) identified the Atlantic meridional overturning circulation as a potential driver of the abrupt changes in the EAWM from rainfall reconstruction over the past 60 000 years using grain-size records in northwestern China's Loess Plateau. In contrast, comparatively little is known about the decadal–multidecadal variability of the NEM over the Indian subcontinent and Southeast Asia.

Likewise, historical simulations and future projections of the South Asian summer monsoon rainfall have been analyzed in numerous studies: The simulations show the presence of large systematic biases in summer precipitation and evaporation over the Indian subcontinent and Indian Ocean (Bollasina and Nigam 2009), while the projections indicate a consistent increase in summer season rainfall (Endo and Kitoh 2016; Sharmila et al. 2015; Sengupta and Rajeevan 2013; Menon et al. 2013) but with weakening of the large-scale monsoon circulation (Sooraj et al. 2015). In contrast, there are few analyses of the NEM simulations and projections: Siew et al. (2014) evaluated

10 atmosphere–ocean general circulation model simulations over Southeast Asia and the Maritime Continent and found widespread biases across the region; a weaker relationship between regional rainfall and ENSO and thus reduced interannual variability was also noted. Parvathi et al. (2017) recently noted the weakening of winter monsoon winds over the Arabian Sea in the Intergovernmental Panel on Climate Change's Fifth Assessment (IPCC-AR5) climate projections, which was attributed to the reduction in the interhemispheric sea level pressure gradient. The projected change in the low-level winds to the east of the Indian Peninsula (i.e., over the southern Bay of Bengal), a key circulation element of the NEM, was not discussed. This study is motivated by the evaluative opportunities presented by the lack of analyses of the NEM rainfall and circulation climatologies and their interannual variability, especially in the context of the IPCC-AR5 simulations and projections. Datasets and analysis method are discussed in section 4.2. Seasonal hydroclimate variability over the South and Southeast Asian continent is presented in section 4.3, including a harmonic analysis showing the annual mean and annual cycle of observed rainfall. The spatial distribution of the climatological OND rainfall, circulation, and related rainfall standard deviation is also described in section 4.3, followed by an intercomparison of in situ and satellite-based precipitation estimates. The rendition of seasonal hydroclimate variability over South and Southeast Asia in select IPCC-AR5 historical simulations is critiqued in section 4.4, followed by an evaluation of the models' skill in replicating the observed OND climatological rainfall distribution. ENSO's characteristic influence on the northeast monsoon in observations and historical climate simulations is described in section 4.5, which also investigates the influence mechanism. The linear trend in

northeast monsoon hydroclimate—rainfall and low-level winds—is examined in section 4.6. Concluding remarks, including implications of this analysis for the potential prediction of winter monsoon rainfall and its hydroclimate impacts, follow in section 4.7.

4.2 Datasets and analysis method

4.2.1 Observed precipitation

Four different gridded rainfall datasets are used to investigate the October–December NEM rainfall distribution, including seasonal and interannual variability, and the influence of ENSO.

The Climatic Research Unit (CRU) Time Series, version 4.00 (CRU-TS4.00; Harris et al. 2014), at 0.5° x 0.5° resolution is high-resolution gridded data of month-by-month variation in climate, available online over the land points for the January 1901–December 2015 period (from https://crudata.uea.ac.uk/cru/data/hrg/cru_ts_4.00). The Global Precipitation Climatology Centre (GPCC; Schneider et al. 2014; Becker et al. 2013) Full Data Reanalysis, version 7, on a 0.5° continental grid (provided online by the Physical Sciences Division of the NOAA Earth System Research Laboratory; https://www.esrl.noaa.gov/psd/data/gridded/data.gpcc.html) is a quality-controlled monthly precipitation dataset derived from 67,200 stations worldwide for the January 1901–December 2013 period using the WMO Global Telecommunication System (GTS), synoptic weather reports (SYNOP), and monthly climate reports (CLIMAT).

The Asian Precipitation—Highly Resolved Observational Data Integration Toward Evaluation of Water Resources (APHRODITE; Yatagai et al. 2012), version 1101 (v1101), is a daily gridded precipitation dataset available online at 0.5° x 0.5° resolution for the January 1951–December 2007 period. The monthly mean is computed from the daily APHRODITE precipitation data, which are available over land from a dense network of rain gauge data over Asia. Last, the joint United States–Japan Tropical Rainfall Measuring Mission (TRMM) satellite product 3B42, version 7 (3B42v7; Huffman et al. 2007, 2010), is available online at 0.25° x 0.25° resolution over both the land and ocean for the period January 1998–present (with a 2-month latency). The TRMM algorithm 3B42 produces merged (satellite rainfall estimates with gauge data) high-quality precipitation data and root-mean-square (RMS) precipitation error estimates on a 3-h temporal resolution in a global belt extending from 50°S to 50°N. The daily-accumulated precipitation product is generated from these 3-hourly merged precipitation estimates.

4.2.2 Observed winds and sea level pressure

The analysis draws on the National Centers for Environmental Prediction (NCEP) Reanalysis (Kalnay et al. 1996) to characterize the circulation associated with the NEM monsoon, especially the 925-hPa winds and mean sea-level pressure (MSLP). This dataset is a global retrospective analysis of atmospheric fields via recovery of land surface, ship, rawinsonde, pibal, aircraft, satellite, and other data, followed by quality controlling and data assimilation, available at monthly resolution on a 2.5° by 2.5° global grid at 17 pressure levels from January 1949.

4.2.3 Observed diabatic heating and streamfunction

The European Centre for Medium Range Weather Forecasting's (ECMWF) interim Re-Analysis (ERA-Interim; Dee et al. 2011), a state-of-the-art global atmospheric reanalysis for the 1979–present period obtained from a 4-dimensional variational (4D-Var) data assimilation system, is used for diagnosis of diabatic heating and streamfunction. The heating diagnosis (N. Dai et al. 2018, unpublished manuscript) follows the strategy outlined in Chan and Nigam (2009); see also Nigam et al. (2000). The mass-weighted vertically averaged (surface-to-100 hPa) diabatic heating and 850-hPa streamfunction are analyzed in the context of the ENSO influence mechanism.

4.2.4 Historical climate simulations

Simulations of 20th-century climate forced by historical greenhouse gas emissions, aerosol loadings, and solar activity are referred to as historical climate simulations (Taylor et al. 2012). Historical simulations of precipitation and SST from five CMIP5 models informing the IPCC-AR5 assessment are analyzed in this study; pertinent features of the models are noted in Table 1. Models from the major climate modeling centers of the US – National Center for Atmospheric Research (NCAR) and NOAA's Geophysical Fluid Dynamics Laboratory (GFDL), and Europe – UK Met Office (UKMO) and the Max Planck Institute (MPI), are investigated, as in Nigam et al. (2017).

4.2.5 Analysis method

The analysis domain is the Indian Subcontinent and Southeast Asia (5°N–40°N, 60.25°E –123°E), and the analysis is restricted to the post-International Geophysical

Year (IGY) period (1958-present). The NEM extends from October to December, consistent with the India Meteorological Department's definition; NEM plots are constructed by averaging the October–December (OND) fields. Analysis of the IPCC-AR5 simulations and projections is based on each model's ensemble–mean; the number of ensemble members is noted in Table 4.1.

Table 4.1. List of CMIP5 GCMs used in this study with their spatial resolution, available time period, and number of ensemble members. Expansion of model names and modeling centers are available online (https://ametsoc.org/pubsacronymlist)

Model name	Modeling center	Number of realizations (ensemble size)	Spatial resolution (longitude x latitude)	Available Time period
CCSM4	NCAR	6	1.25º x 0.942º	1850–2005
GFDL–CM3	NOAA GFDL	5	2.5º x 2.0º	1860–2004
HadCM3	UKMO	9	3.75º x 2.5º	1860–2005
HadGEM2–ES	UKMO	4	1.875º x 1.25º	1860–2005
MPI–ESM–LR	MPI	3	1.875º x 1.865º	1850–2005

The ENSO–NEM relationship is characterized from the temporally leading (OND) regressions of precipitation on the winter [December–February (DJF) averaged] Niño-3.4 SST index in the post-IGY period (1958–2013). Because ENSO SST anomalies are robust in boreal winter, using just the winter value of the Niño-3.4 SST index ensures robust tracking of ENSO variability. The Niño-3.4 SST index is

constructed by areal-averaging of the SST anomalies in the 5°S–5°N and 170°W–120°W domain, using the *aave* function in the Grid Analysis and Display System (GrADS–2.1.a3) toolkit. In most figures, a 9-point smoother (the *smth9* function in GrADS) is applied to highlight the coherent, larger-scale spatial features.

The statistical significance of the regressions at the 95% level is evaluated through a two-tailed Student's *t* test using the original sample size. The *t*-value from observations is calculated via the formula: $t = \frac{r\sqrt{n-2}}{\sqrt{1-r^2}}$ where $n = N$ is the original sample size, and *r* is the correlation at each grid point. The results were almost identical while using an effective sample size, $n = N_e$ [following the method of Quenouille (1952)], suggesting that serial correlation is not an issue for this analysis.

The statistical significance of a rainfall trend is computed as the ratio between its slope and standard error. Trends are considered to be statistically significant when the *t* value of observations computed using an effective sample size (n_e) from lag-1 autocorrrelation of the residual time series *e(t)* exceeds the critical *t*-value at 95% level [following the adjusted standard error and adjusted degrees of freedom method (AdjSE + AdjDF); Santer et al. 2000].

4.3 Hydroclimate variability over South and Southeast Asia

4.3.1 Seasonal cycle

Precipitation and surface air temperature are the extensively monitored hydroclimate fields. The annual mean and annual cycle of observed precipitation from the GPCC (version 7; land-station based) and TRMM (3B42v7; satellite based, and thus for both land and ocean) data are displayed in Fig. 4.1. A harmonic analysis (Wilks

2006) of the climatological monthly mean precipitation is performed to extract the annually varying component, which is displayed using vectors, with the length denoting the amplitude of the annual cycle and the direction indicating its peak phase, following Nigam and Ruiz-Barradas (2006). The rainfall annual mean is shown with superposed contours plotted at a 1.0 mm/day interval (Fig. 4.1). It is notably large (~7–8 mm/day) on the western coast (Konkan) and northeastern states of India, and over Bangladesh, Myanmar, and the Philippines; over southeast peninsular India and Sri Lanka, the annual-mean rainfall is 3–4 mm/day. On the other hand, rainfall is scanty (<2 mm/day) over northwestern India and central and southern Pakistan and moderate (3–4 mm/day) over eastern China. Over the oceans (see Fig. 4.1, lower panel), the rainfall annual mean is large (~6–8 mm/day) over the eastern Bay of Bengal along Bangladesh and Myanmar coastlines [in agreement with Shige et al. (2017)] and over the southeastern South China Sea.

The vectors in Fig. 4.1—their large amplitude and especially direction—succinctly capture the prominent seasonality (i.e., monsoonal nature) of rainfall over South and Southeastern Asia: The summer monsoon rainfall over India, Bangladesh, and the Indochina Peninsula peaks in July (blue vectors pointing northward), while the pre-Mei-yu and Mei-yu rainfall over eastern China peaks in late spring (blue arrows pointing northwestward). Also present in Fig. 4.1 are regions where rainfall peaks in late autumn and early winter (red arrows pointing east and southeastward); these regions, primarily confined to the eastern coasts, are far smaller in extent than the spring to summer monsoon rainfall region, which encompasses large swaths of the southern continent. Notable regions of peak early winter rainfall—the focus of this

study—are southeastern peninsular India, Sri Lanka, and the east coasts of Thailand, Malaysia, Vietnam, and the Philippines. In the Indian subcontinent, the early winter rainfall is often referred to as the NEM, or just the winter monsoon; the ‘‘northeast’’ attribute comes from the prevailing surface northeasterlies, shown later in Fig. 4.2.

The TRMM precipitation that provides a rare view of the rainfall over tropical oceans is analyzed in the lower panel of Fig. 4.1. Harmonic analysis of the land–ocean rainfall shows that the NEM rainfall region is not just confined to peninsular India, Sri Lanka, and the east coast regions in Southeast Asia but expansive, extending over large sectors of the neighboring seas, for example, southwestern Bay of Bengal, north-equatorial Indian Ocean, and the western South China Sea. Minor discrepancies in vector magnitude and orientation between GPCC and TRMM annual cycles are found over remote mountainous regions in the northeastern sector of the subcontinent (e.g., Bhutan, Assam, and Myanmar) and over the Western Ghats in peninsular India; some of the discrepancies result from the different climatology periods. Note, in some regions of India and Bangladesh, the amplitude of the annual cycle is larger than the annual mean, reflecting the presence of semiannual variability (originating from an extended dry season).

4.3.2 Northeast monsoon rainfall and circulation

The spatial distribution of NEM rainfall and associated sea level pressure and low-level circulation is displayed at monthly resolution during October–January in Fig. 4.2. October is evidently the wettest month in the period, with rainfall progressively decreasing through January. Southeast peninsular India records more than 6.0 mm/day in October, 4.5 mm/day in November, and more than 1.5 mm/day in December; there

is no significant rainfall in January. October rainfall is large also over Sri Lanka (>6.0 mm/day), Vietnam (>9.0 mm/day), the Philippines (>6.0 mm/day), Myanmar (>4.5 mm/day), Laos (>3.0 mm/day), Cambodia (>4.5 mm/day), and Thailand (>3.0 mm/day). Rainfall becomes more coastally confined as the winter monsoon season progresses, with the entire continent, except Sri Lanka and the Malay Peninsula, devoid of rainfall in January.

A salient feature of the seasonal circulation during the winter monsoon is the low-level northeasterly flow over the Indian subcontinent and Southeast Asia. Interestingly, in October—the wettest month of the monsoon—the onshore flow from the Bay of Bengal is easterly, with the northeasterlies confined to peninsular India. This flow structure is, of course, consistent with the presence of a low pressure center over the southwestern Bay of Bengal (e.g., the 1010-hPa isobar in Fig. 4.2, top panel) and the associated cyclonic (counterclockwise) circulation. The advent of significant northeasterly winds (~5–8 m/s) over the Bay of Bengal in November (i.e., a month after their appearance over the South China Sea) reflects organization by the southern flank of the emerging continental-scale Siberian high; see the SLP distribution in Fig. 4.2.[11] The northeasterly flow remains firmly embedded in the region, at least until January, accounting for winter rainfall in the narrow onshore coastal regions. Over the South China and Philippine Seas, the northeasterly winds are established in October itself (i.e., earlier than the Bay of Bengal),[12] as part of the regional high-SLP feature over

[11] October is the transition month between summer and winter monsoons, considering vestiges of low SLP in the southwestern Bay of Bengal and the related cyclonic circulation. A hypothesis for the origin—or the lingering—of low SLP in the bay in October is currently being evaluated from observational analysis.

[12] Early retreat of the westerlies over the South China Sea relative to the Bay of Bengal was reported by Matsumoto (1997) as well, although at pentad resolution.

northern China. The northeasterlies bring impressive winter rains, especially over the eastern coasts of Vietnam and Thailand, and also over the Philippines, Laos, and Cambodia.

4.3.3 Interannual variability of Northeast monsoon rainfall

The interannual variability of rainfall is assessed in Fig. 4.3 from the display of the rainfall standard deviation (SD) in October and December, the start and end months of the NEM season. In October, the SD over southeastern peninsular India and Sri Lanka is 1.5– 4.5 mm/day against a climatology of ~6 mm/day, whereas the SD is >3 mm/day over Vietnam, where climatological rainfall is ~9 mm/day; the SD is large over the Philippines as well. The October rainfall SD is also large (>3 mm/day) over Bangladesh and northeastern India, although this region is not an NEM region (cf. Fig. 4.1b). The December rainfall is seemingly less variable but not when viewed relative to its climatology; for example, SD over coastal peninsular India is 1.5–3.0 mm/day against a regional climatology of ~3 mm/day.

4.3.4 Northeast monsoon rainfall in in-situ and satellite-based precipitation analyses

The climatological October-December rainfall is displayed over land and ocean in Fig. 4.4 using TRMM data, and the three gauge-based precipitation analyses commonly used to monitor rainfall over the Asian continent are compared with the satellite-based precipitation estimate; the climatology is based on the common 10-year period (1998–2007)[13] of the four datasets. Although the OND months span the NEM

[13] Of the four, the APHRODITE v1101 data is most restrictive as it ends in December 2007.

season, regions other than the NEM regions also have rainfall in this period; just not their peak rainfall. The NEM regions noted earlier (the red arrow regions in Fig. 4.1b) are apparent in Fig. 4.4a when attention is restricted to the regions where OND rainfall is larger than 4.5 mm/day (the third contour). Of the three in-situ datasets, GPCC (Fig. 4.4b) is in closest agreement with TRMM but for the differences over Vietnam where in-situ data is unable to resolve the influence of narrow coastal orography on regional rainfall—more rain on the windward side (i.e., to the east, in view of the prevailing northeasterlies) with a rain shadow to the west. The CRU rainfall (Fig. 4.4c) is positively biased with respect to TRMM, especially over Myanmar, Laos, Cambodia, and Vietnam where the bias is in the 0.5–3 mm/day range. The APHRODITE rainfall (Fig. 4.4d), on the other hand, exhibits a dry bias of similar range with respect to TRMM, notably over the core NEM regions (peninsular India, Sri Lanka, Southeast Asia, and the Philippines). The intercomparison indicates some preference for the GPCC precipitation analysis in documentation of the longer-period NEM climatology and interannual variability.

4.4 The Northeast monsoon in historical climate simulations

4.4.1 Simulation of seasonal cycle

The simulations of 20th-century (i.e., historical) climate provide a unique opportunity for the evaluation of models whose projections of future climate form the backbone of the IPCC-AR5 Report (Flato et al. 2013). The annual-mean and annual-cycle of rainfall, obtained from harmonic analysis of the climatological monthly rainfall in five historical simulations, is shown in Fig. 4.5; the TRMM precipitation

analysis (Fig. 4.1b; and reproduced in Fig. 4.5a to facilitate comparison) is the target for these simulations. Although the simulated hydroclimate can be comprehensively critiqued using harmonic plots – for example, both summer and winter monsoons can be assessed – the focus here is on the NEM whose amplitude and temporal phase is visually highlighted using red arrows in Fig. 4.5 (as in Fig. 4.1b).

The NCAR-CCSM4 simulation (Fig. 4.5b) of the winter monsoon is reasonable but for the lack of confinement of the monsoon region to near-coastal waters; for example, the NEM region is unrealistically expansive over the South China Sea and even over the north-equatorial Indian Ocean. The temporal phasing is also a bit off in view of the lack of southeastward orientation of the arrows off the tip of Indian peninsula. The NCAR simulation is not without other deficiencies—notably, the absence of intense summer monsoon precipitation along the southwest coast of India and the west coast of Myanmar and Thailand, which is likely from the lack of model resolution of the narrow orographic features in these regions (e.g., the Western Ghats). Likely related to this deficiency is the overrepresentation of summer monsoon precipitation over the Himalayan region and the northern Gangetic Plain. The GFDL-CM3 simulation (Fig. 4.5c) of the NEM is like NCAR's but more deficient along the Vietnam coast where the peak rainfall month in the simulation is late summer rather than in mid-autumn. The distribution of rainfall annual mean in the GFDL simulation, again, shows the impact of unresolved orography, even the Himalayan–Tibetan complex, to an extent.

The UKMO HadCM3 simulation departs the most from the observed rainfall distribution (Fig. 4.5d): Although it has some vestiges of the NEM, the annual-mean

rainfall is underestimated in the west (Indian subcontinent) and overestimated in the east (South China Sea); the lack of intense precipitation zones over the continent, likely, results from the coarse model resolution (see Table 4.1). The other UKMO model (HadGEM2–ES; Fig. 4.5e) underestimates even more the rainfall annual mean over western and peninsular India. Despite this dry bias (reflected also in the reduced red-arrow amplitudes along the southeastern coast), the NEM timing and its eastward extent over the Bay of Bengal and the South China Sea are well represented. The model's finer resolution allows a quasi-realistic representation of the intense precipitation along Myanmar's coast and over the northeastern Indian subcontinent. The MPI–ESM–LR simulation (Fig. 4.5f) captures aspects of the NEM and the larger rainfall distribution. Notable departures include an expansive NEM over the South China Sea and the shifted location of rainfall maxima, for example, a northward shift over the northeastern Indian subcontinent and a southward one along the Myanmar coast.

4.4.2 Simulation of October-December rainfall

The models' skill in simulating the October–December rainfall over South and Southeast Asia and the adjacent seas/bays is assessed in Fig. 4.6, which compares the OND period climatology in the common period of the historical simulations and TRMM dataset (1998–2005). The model rainfall climatology is shown as the difference from the TRMM one (Fig. 4.4a; the validation target). Focusing on the NEM regions, the bias in simulations is large and extensively distributed over peninsular India and Vietnam and the southwestern Bay of Bengal and the South China Sea. Over peninsular India, the bias is generally negative, especially in the Hadley simulations which underestimate rainfall by as much as 50%; the NCAR simulation is the only one

overestimating NEM rainfall. All 5 simulations underestimate the OND rainfall over Vietnam and its coastal zone, and overestimate rainfall over the central-eastern South China Sea. The OND rainfall bias over Sri Lanka is similar to that over peninsular India: positive in the NCAR simulation and negative in the others, with GFDL being neutral in this regard.

4.5 Influence of El Niño Southern Oscillation on the Northeast monsoon rainfall

The influence of El Niño Southern Oscillation (ENSO) on the South Asian summer monsoon—the southwest monsoon—has been extensively documented since the pioneering analysis of Rasmusson and Carpenter (1983) and Sikka (1980) and used in the dynamical and statistical predictions of summer monsoon rainfall over the Indian subcontinent. The summer preceding the peak warm-phase of ENSO—El Niño—shows impressive rainfall deficits over the entire subcontinent; the following summer also exhibits deficits but only over the eastern-northeastern subcontinent.

El Niño's influence on the northeast winter monsoon has also been investigated from observational analysis: the NEM was shown to strengthen during the ENSO build-up year, i.e., above-normal autumn precipitation over southeastern peninsular India and Sri Lanka (Rasmusson and Carpenter 1983; Ropelewski and Halpert 1987). A closer examination of how Sri Lanka's rainfall distribution is impacted was undertaken by Suppiah (1997). The present analysis expands on these studies, principally, in three ways. First, it shows the ENSO impact on the larger NEM region, one that includes eastern Indochina and the Philippines, in addition to peninsular India and Sri Lanka.

Second, instead of compositing, it uses objective analysis based on linear regressions on the Niño-3.4 SST index to extract the ENSO influence. Finally, it documents, perhaps, for the first time, the subseasonal variation of the ENSO influence; all in Fig. 4.7.

4.5.1 The ENSO influence in observations

The influence of El Niño on the NEM is obtained from rainfall regressions on the winter Niño-3.4 SST index, as discussed in section 4.2.5. The influence on OND rainfall (Fig. 4.7a) is essentially confined to the core NEM regions: southeastern peninsular India and Sri Lanka with above-normal rainfall, and further to the east, eastern Indochina and the Philippines with below-normal rainfall. The ENSO influence is significant: Over India and Sri Lanka, the regressions are ~0.4 mm/day/unit index, which translates into a rainfall anomaly of ~0.8 mm/day for a strong El Niño episode (Niño-3.4 SST index of ~2). Comparison with the regional OND climatology (~5 mm/day; cf. Fig. 4.4a) indicates that the anomalies are significant, being ~16% of the climatology. Likewise, anomalies over eastern Vietnam are ~1.5 mm/day/unit index, or ~3 mm/day for a strong episode, while the regional OND climatology is 12-15 mm/day (cf. Fig. 4.4a). Outside the core monsoon region, the ENSO influence on the seasonally averaged (OND) rainfall is modest.

The ENSO influence on the NEM low-level (925 hPa) circulation is also shown in Fig. 4.7. The seasonal (OND; Fig. 4.7a) influence consists of weak anticyclonic flows: one centered over the Bay of Bengal with easterlies (~0.8 m/s/unit SST index) in the deep Tropics and weak southeasterlies over peninsular India and another over the South China Sea associated with southwesterly flow over Southeast Asia and

eastern China (~1 m/s/unit SST index).

The subseasonal variation in ENSO's influence is documented from separate regressions of the October and November rainfall (Figs. 4.7b, c). The October influence (Fig. 4.7b), especially the rainfall deficit over the western-central and northeastern subcontinent, is broadly similar to the El Niño–related anomalies in summer monsoon rainfall in the ENSO-development year (Rasmusson and Carpenter 1983), generating an impression that the summer monsoon season (June–September in climatological rainfall) continues for an additional month, at least, in the context of the ENSO influence. In the NEM regions, El Niño generates positive anomalies in October rainfall over southeastern peninsular India and Sri Lanka, and negative ones over Indochina and the Philippines. The ENSO wind regressions consist of robust anticyclonic flow over the South China Sea, with easterlies (~0.8–1.2 m/s/unit index) over lower Indochina and southwesterlies to the north; wind regressions over peninsular India are also strong and primarily easterly.

El Niño's influence on November rainfall (Fig. 4.7c) shows positive anomalies over peninsular India, especially in its southeastern sector (Kerala, Tamil Nadu, and Andhra Pradesh, India), and negative ones over southeastern Indochina and the Philippines, the latter, much as in October. Farther to the north over peninsular India, the November anomalies (positive) are quite opposite of the October ones—an impressive subseasonal variation in ENSO's rainfall influence that is concealed in the OND average. The November anomalies are significant and positive also over eastern China, and the ones over Bangladesh and Myanmar, while negative, are relatively positive vis-à-vis the October ones. ENSO's November wind regressions depict a well-

developed anticyclonic flow structure over the Bay of Bengal, with southerly flow over peninsular India—in contrast with the ENSO-related easterly anomalies in the preceding month.

4.5.2 The ENSO influence mechanism

The mechanisms by which El Niño SST anomalies in the central-eastern equatorial Pacific influence the northeast winter monsoon rainfall are briefly investigated in this section. The vertically averaged (1000–100 hPa) diabatic heating (Q_D), residually diagnosed from ERA-Interim, and the lower-tropospheric streamfunction ψ_{850} anomalies are examined in November when El Niño's influence on peninsular India is strongest (cf. Fig. 4.7). As before, the anomalies are obtained from the temporally leading regressions on the DJF Niño-3.4 SST index.

The ENSO-related November diabatic heating anomalies (Fig. 4.8) are positive in the central-eastern equatorial Pacific (approaching +1.0 K/day/unit SST index) and negative over the Maritime Continent, northwestern tropical Pacific (including Indochina and the Philippines), and the South Pacific convergence zone, in line with their earlier characterization (Nigam et al. 2000). Superposed ψ_{850} contours in Fig. 4.8 characterize the low-level rotational circulation response, which consists of cyclonic circulation straddling the equator in the central basin, leading to equatorial westerlies in the heating anomaly longitudes. Likewise, a pair of anticyclones straddle the equator in the eastern Indian Ocean basin, with related easterlies. The rotational response has some resemblance with the response of deep convective heating in the Matsuno–Gill model (Matsuno 1966; Gill 1980). This model is however unable to realistically model

the divergent response, as noted in Nigam and Shen (1993),[14] and, of course, the near-surface wind response under the large-scale subsidence zones over tropical basins (Lindzen and Nigam 1987).

The characterization of El Niño–related low-level winds in the global Tropics (Fig. 4.8) facilitates understanding of how El Niño's influence on NEM rainfall is generated: The anticyclonic circulation over the Indian Ocean (notably in Fig. 4.7c)—key to onshore moisture transports over peninsular India and the resulting orography-mediated positive rainfall anomalies in the core NEM regions—is itself a key element of El Niño's widely modeled tropical atmospheric response (Watanabe and Jin 2002, their Fig. 2a; Wang and Zhang 2002, their Figs. 6c-d) to reduced convection over the Maritime Continent and adjoining regions (northwestern tropical Pacific and Southeast Asia).

4.5.3 ENSO influence on the NEM rainfall record

The rainfall anomalies over southeastern peninsular India and Sri Lanka – a core NEM region marked in red in Fig. 4.3 (top panel) – is plotted in Fig. 4.9 both for October and November, and for the OND period. Also plotted is the winter (December–February) Niño3.4-SST index, in red. The index exceeds +2.0 during 1982–83 and 1997–98, marking major episodes of the recent period; the most recent one, in 2015–16, when the index was even higher (~ +3.0) is not shown as the GPCC rainfall record ends in December 2013. The ENSO index is correlated with October rainfall at +0.11,

[14] The low-level convergence over the heating maximum is generated mostly from meridional convergence (i.e., $\partial v/\partial y$) in nature but not in the Matsuno–Gill model where zonal convergence (i.e., $\partial u/\partial x$) remains dominant.

and with the November and OND rainfall at +0.29 and +0.29, respectively; the latter two are statistically significant at the 95% level. The low October correlation is not unexpected, given the very limited footprint of the ENSO precipitation anomalies in the core NEM region (Fig. 4.7b).

4.5.4 The ENSO influence on NEM rainfall in historical simulations

The rendition of ENSO's influence on the NEM rainfall in the IPCC-AR5 historical simulations is documented in Fig. 4.10, notwithstanding the significant biases in the modeled NEM rainfall climatologies (cf. Fig. 4.6). Rainfall regressions on the Niño3.4-SST index (obtained from the related SST simulation) were computed for each ensemble member, and then averaged across all simulations of each model. The El Niño influence on NEM rainfall is evidently very weak in the simulations, especially over continents where the impact is below the contouring threshold (0.3 mm/day/unit index); lowering the threshold by one-half was also unproductive. Two of the five simulations [NCAR (Fig. 4.10a) and MPI (Fig. 4.10e)] do contain a weak signal over southeastern peninsular India but of the wrong sign. The El Niño's influence over eastern Indochina is however correctly represented, sign-wise, but again with weaker amplitude. Unfortunately, the TRMM rainfall record is too short for the extraction of the characteristic El Niño influence on oceanic precipitation. In the absence of a validation target, the veracity of the simulated El Niño–related rainfall deficit over the South China Sea remains unassessed.

4.6 Trends in Northeast monsoon rainfall

Historical precipitation trends over Southeast Asia have been investigated from

an extensive suite of meteorological stations in previous studies. Heavy precipitation was shown to increase (decrease) in southern (northern) Vietnam (Endo et al. 2009). Trends in extreme precipitation in the Philippines were assessed by Villafuerte et al. (2014). The present study is focused on the seasonal winter monsoon (OND) precipitation trends; thus, not limited to extreme events. The NEM rainfall is analyzed in the post-IGY period (1958–2013) to uncover potential trends in this 56-year record over the NEM regions (eastern Indochina, the Philippines, peninsular India and Sri Lanka); the October–December trends are displayed in Fig. 4.11.

In focusing on the core NEM regions, positive trends are found over southern Vietnam, the Philippines, Malaysia, and southern and eastern peninsular India. The trends are larger than 1.5 mm/day/century and statistically significant (at the 95% level) over southern Vietnam, reflecting a ~0.84 mm/day increase in OND rainfall in the post-IGY period. The increase is notable as climatological rainfall in these months is ~4.5–6.0 mm/day; the IGY-period trends thus represents, approximately, 15–20% increase in OND rainfall in this region. Over southeastern Philippines, significant positive trend larger than 2.0 mm/day/century reflects a 15% increase in OND rainfall. Meanwhile, over peninsular India, the NEM trends are not statistically significant; however, trends are not declining, being typically larger than +1.0 mm/day/century. Notable trends in OND rainfall are also present outside the NEM regions, but these are not as consequential as OND is not the peak rainfall season there, for example, the drying trend in the Irrawaddy River basin (Myanmar).

The origin of the modest post-IGY increase in NEM rainfall over coastal Vietnam was briefly investigated from analysis of the near-surface (925 hPa) wind

trend, drawing on the basic notion of the monsoon as being driven by onshore moisture-laden winds. Although uncertainties in the early-period upper-air winds, especially over the oceans, preclude attribution, in some regions, such as eastern Indochina, a positive northeasterly wind trend is evident. No such trend is, however, present over peninsular India, another region of positive rainfall trends.

4.7 Concluding remarks

The northeast winter monsoon, the diminutive cousin of the southwest summer monsoon, brings seasonal (winter) rains to the eastern coast of peninsular India, Indochina and the Philippines. The low-level northeasterly winds impinge on the eastern coasts after gathering moisture over the upstream bays and seas, for example, the Bay of Bengal in case of the peninsular India, and the South China Sea in case of eastern Indochina. The onshore moisture influx is a necessary but not sufficient condition; flux convergence is needed for rainfall, with orographic interaction, often generating the convergent conditions, for example, with the Eastern Ghats over peninsular India. Quite like the teeming Indo-Gangetic plain where southwest monsoon brings bountiful rain in summer, the populous eastern coastal regions depend on the northeast monsoon for life and sustenance. The NEM has, however, received less research attention, motivating this observational analysis that focuses on the NEM's climatological evolution at monthly resolution, its interannual variability, and long-term trend.

Given the complex orography and narrow coastal zones in the NEM domain, the longer period in-situ precipitation analyses were first assessed from intercomparison with the recent period Tropical Rainfall Measuring Mission's

(TRMM) precipitation. The overlap period comparisons showed the Global Precipitation Climatology Center's (GPCC) in-situ analysis to have the least bias, prompting its further use in the interannual variability and trend analysis; the CRU-TS4.00 slightly overestimates precipitation over southern Myanmar and Indochina, and the APHRODITE-v1101 analysis exhibits a dry bias over the core NEM regions.

The four major findings of this study are:

- The NEM core regions are demarcated from harmonic analysis of climatological monthly precipitation data, both in-situ (GPCC) and remotely sensed (TRMM).
- The monthly evolution of the NEM is documented from analysis of rainfall, sea level pressure, and the low-level winds. A key finding here is the asynchronicity in the establishment of northeasterlies over the Bay of Bengal and the South China Sea; the northeasterlies appear over the Bay of Bengal in November, i.e., a month later than over South China Sea.
- El Niño–Southern Oscillation's impact on NEM rainfall is shown to be significant: The El Niño phase leads to a stronger NEM rainfall over southeastern peninsular India and Sri Lanka, but diminished rainfall over Thailand, Vietnam, and Philippines. An interesting finding here is that the impact varies subseasonally, being weak in October and strong in November. The positive rainfall anomalies over peninsular India are generated by the anticyclonic flow centered over the Bay of Bengal, which is forced by the El Niño–related reduction in deep convection over the Maritime Continent.
- The historical 20th-century climate simulations informing the IPCC-AR5

show varied deficiencies in the NEM rainfall distribution, and a markedly weaker (and often unrealistic) ENSO–NEM rainfall relationship.

Statistical and dynamical predictions of the northeast winter monsoon rainfall over peninsular India and Sri Lanka are in relative infancy vis-à-vis the southwest summer monsoon. Perhaps, this analysis of the El Niño–Southern Oscillation impacts, especially their subseasonal variation, presented in this chapter will reinvigorate these efforts, bringing hydroclimate relief to millions.

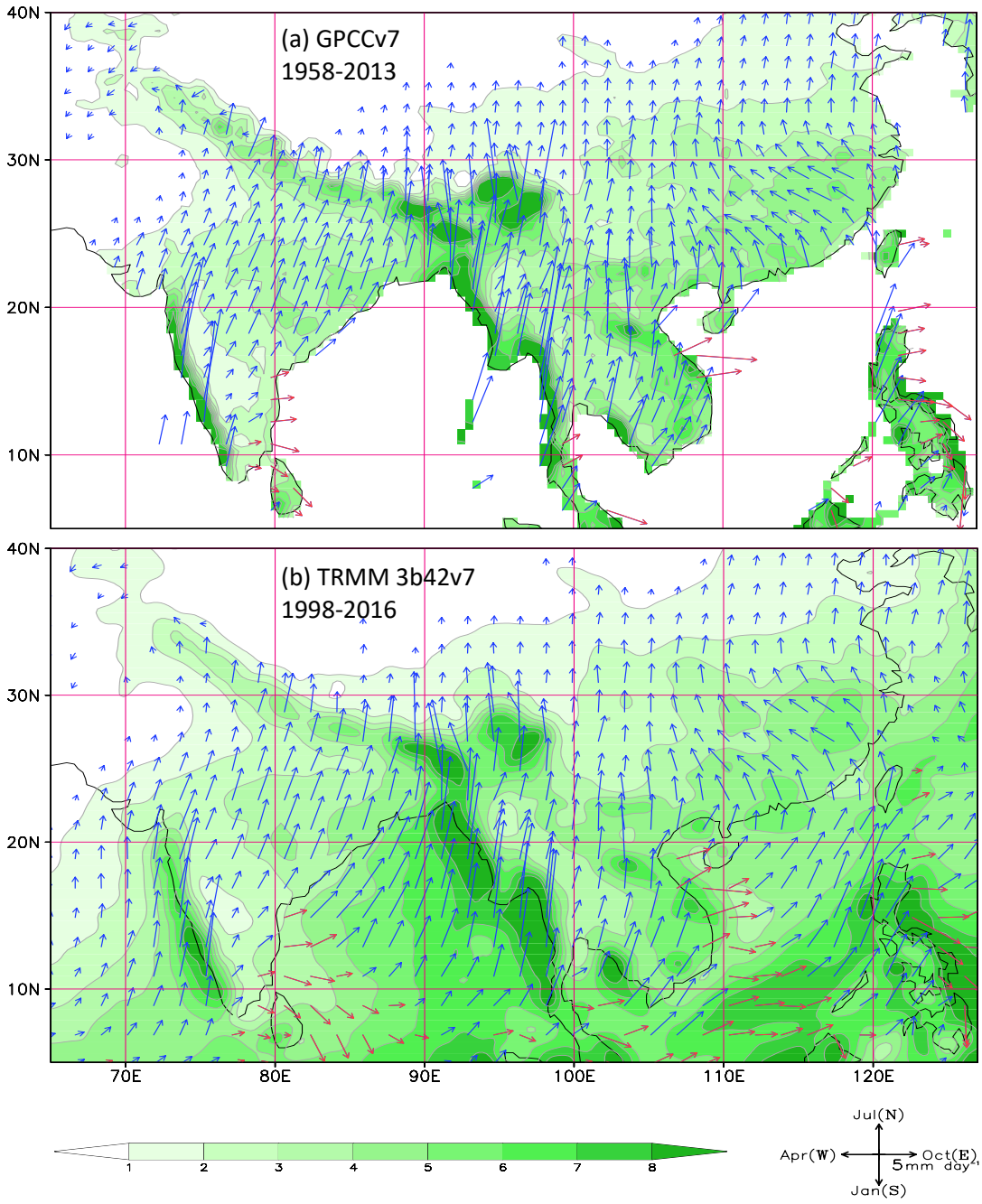

Figure 4.1. Annual-mean and annual-cycle of rainfall: (a) GPCC ver. 7 (1958–2013) and (b) TRMM 3b42v7 (1998–2016). Vectors represent annual-cycle (first harmonic) while contours show the annual-mean in mm/day. Vector scaling and annual-cycle phase is shown on the lower right; vectors pointing north indicate July as the maximum rainfall month, and so on. Vectors in red represent regions receiving winter monsoon rainfall during the OND season. Annual mean rainfall is contoured and shaded at 1.0 mm/day intervals. The amplitude threshold for plotting vectors is 0.75 mm/day. The plot (b) is shown after four applications of the nine–point smoother (smth9) in GrADS.

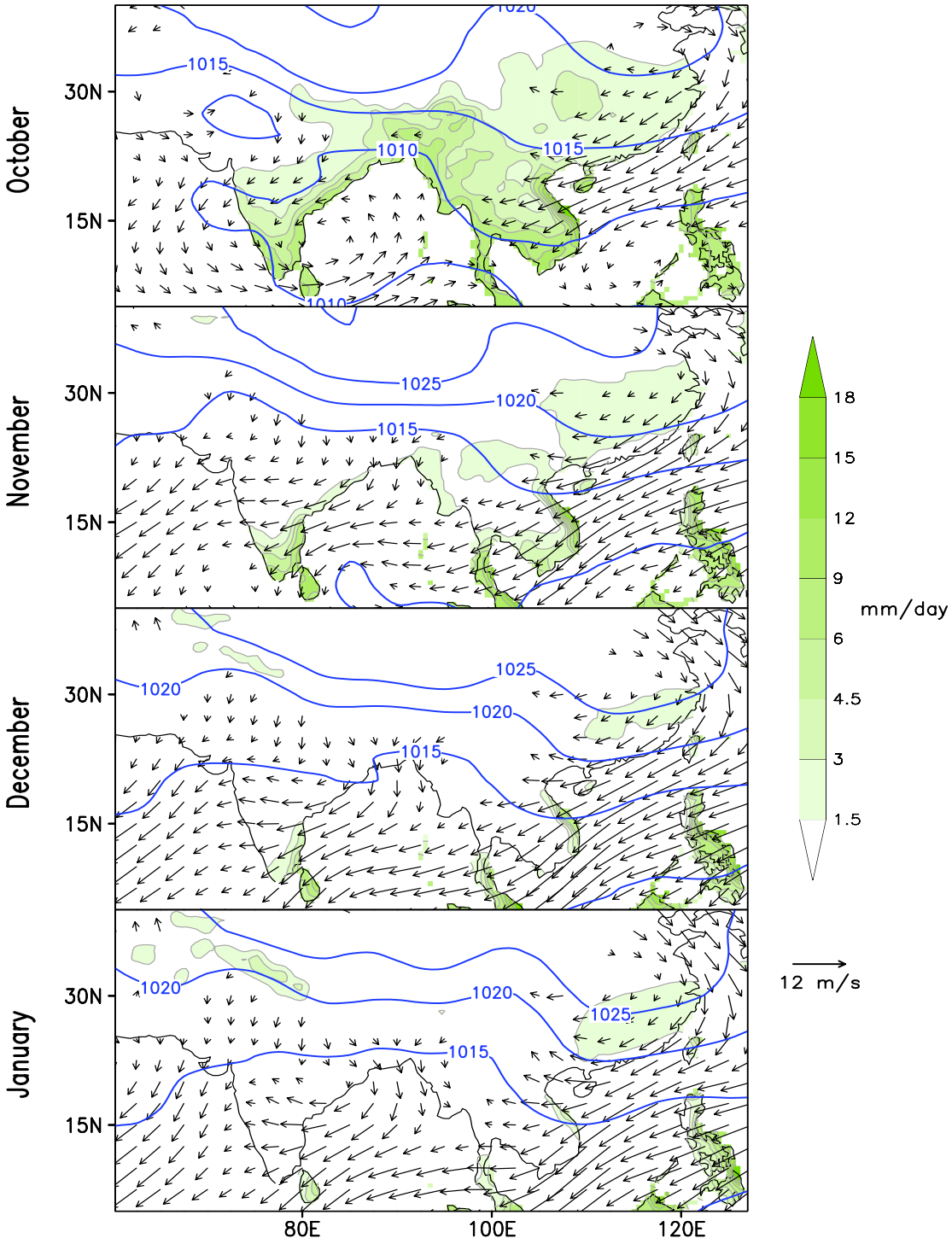

Figure 4.2. Climatological rainfall (GPCC ver. 7), 925-hPa vector winds and MSLP (NCEP Reanalysis) for the months of October, November, December and January. The period of analysis is 1958–2013. Contour interval (C.I.) for rainfall is 1.5 mm/day for values less than 6.0 mm/day, and 3.0 mm/day for higher values; shading threshold is 1.5 mm/day. The threshold for plotting wind vectors is 1.0 m/s; SLP is contoured at 5-hPa. The rainfall field is displayed after one application of smth9.

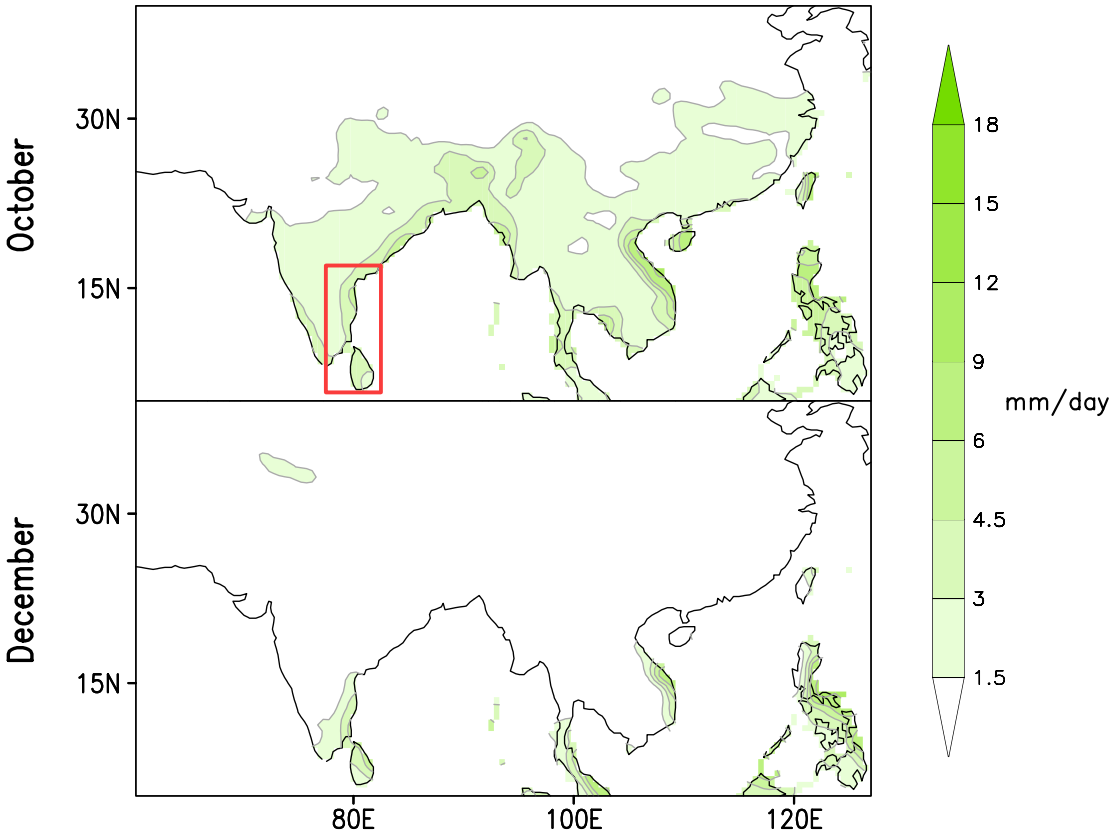

Figure 4.3. Standard deviation of rainfall (1958–2013) showing rainfall variability based on GPCC ver. 7 dataset for the months of October and December. Contour interval is 1.5 mm/day for values less than 6.0 mm/day, and 3.0 mm/day for higher values; shading threshold is 1.5 mm/day. The fields are displayed after one application of smth9.

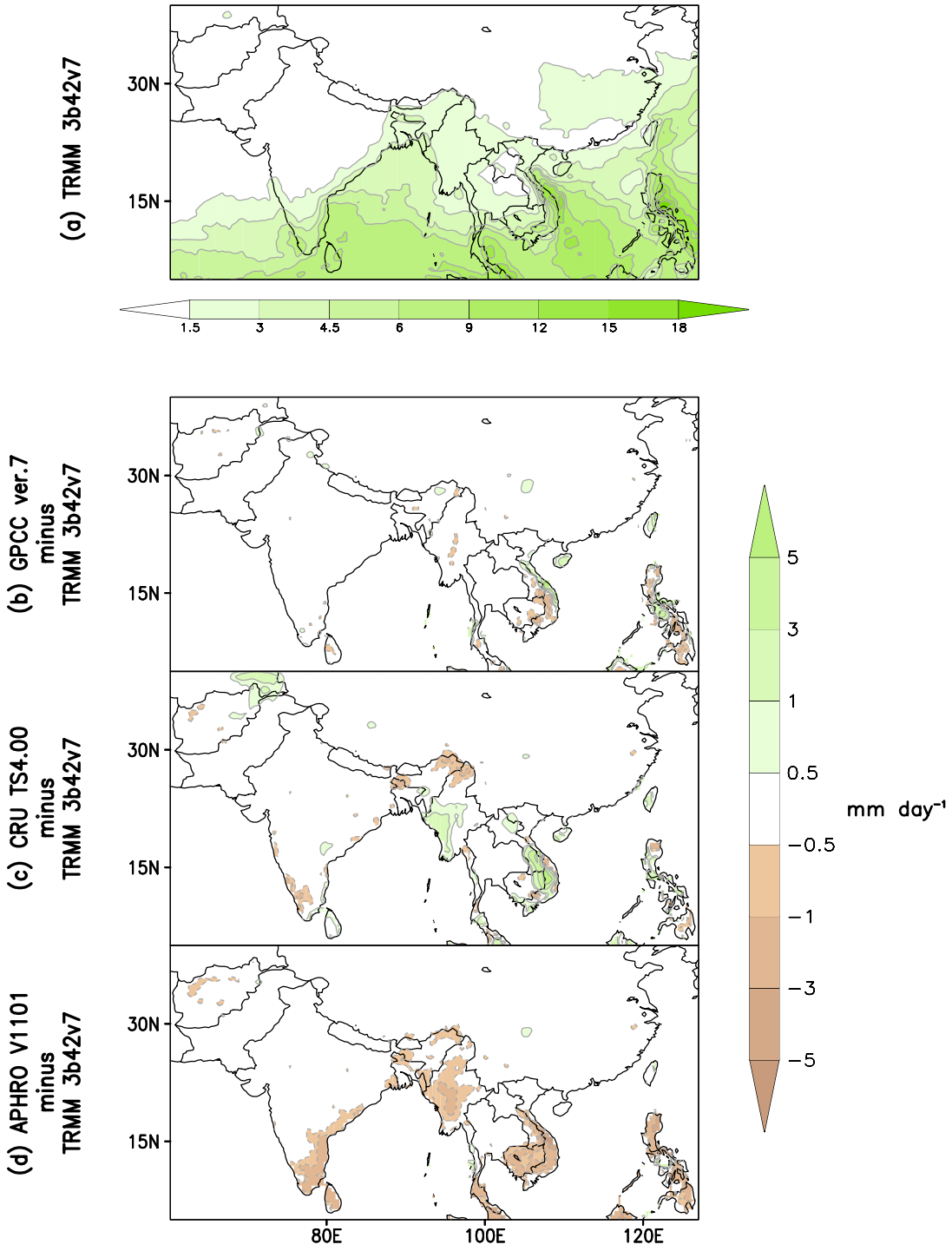

Figure 4.4. Climatological October through to December (OND) seasonal rainfall (1998–2007): (a) based on TRMM 3B42v7; difference between (b) GPCC ver.7 and TRMM; (c) CRU-TS4.00 and TRMM; and (d) APHRODITE v1101 and TRMM. For (a), contour interval (C.I.) is 1.5 mm/day for values < 6.0 mm/day, and 3.0 mm/day for higher values. For (b), (c), and (d), C.I. is 0.5 mm/day for values < 1.0 mm/day and 2.0 mm/day for higher values. Shading threshold is 1.5 mm/day for (a), 0.5 mm/day for (b), (c), and (d). The fields are displayed after one application of smth9 in GrADS.

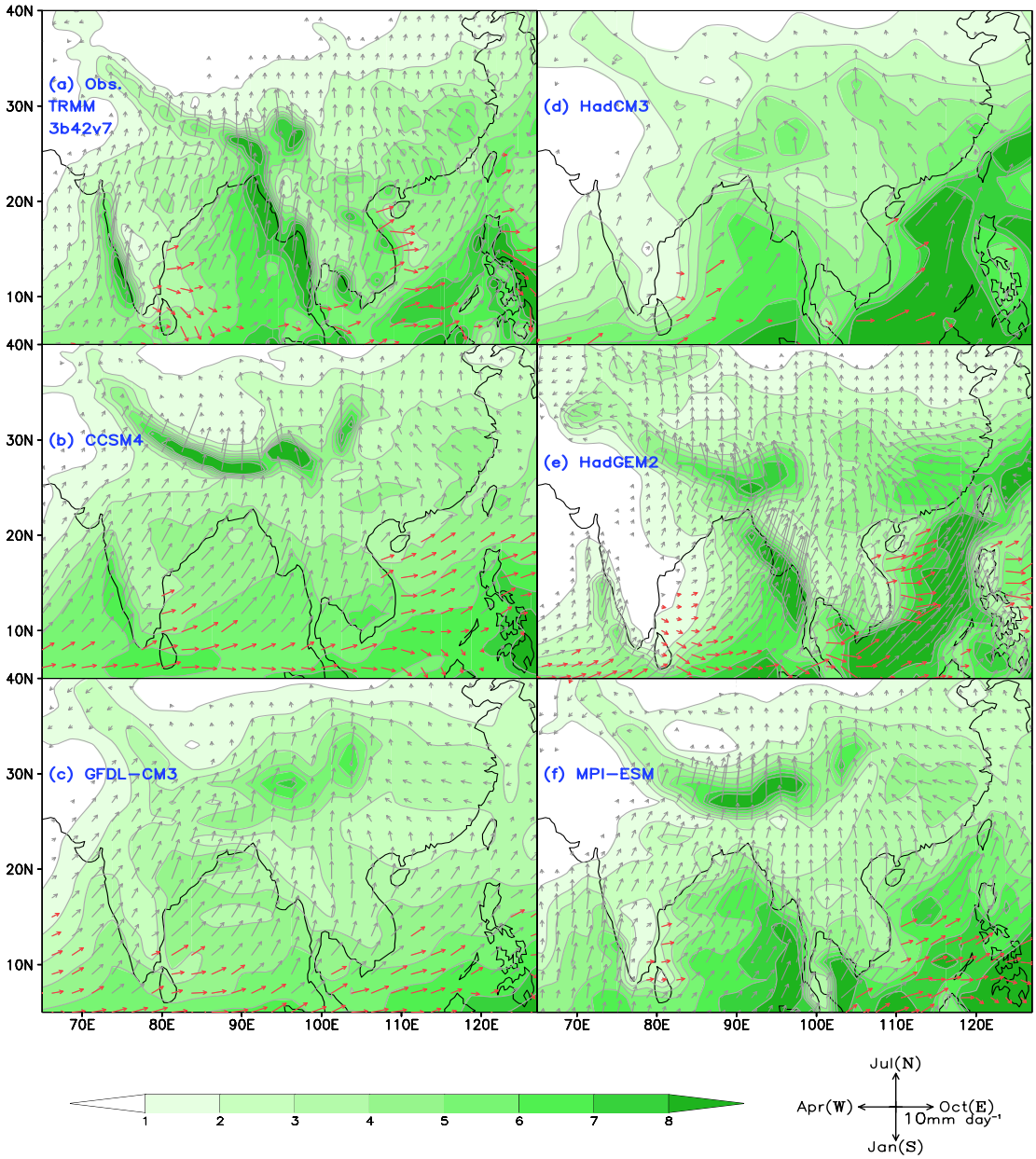

Figure 4.5. Climatological rainfall in five IPCC–AR5 historical climate model simulations (1986–2005). The climatological precipitation from TRMM 3b42v7 (1998–2016) — the observational target — is shown in (a). The average field across all ensemble members of each simulation is shown in (b)-(f). Vectors represents annual cycle (first harmonic) while contours show annual mean in mm/day. Vector scaling and annual-cycle phase is shown at the bottom right; vectors pointing north indicate July as the maximum rainfall month, and so on. Vectors in red represent regions receiving winter monsoon (OND) rainfall. Annual mean rainfall is contoured and shaded at 1.0 mm/day intervals. The amplitude threshold for plotting vectors is 0.75 mm/day. As the observational dataset is on a much finer resolution compared to the model fields, subplot (a) is shown after four applications of smth9 in GrADS.

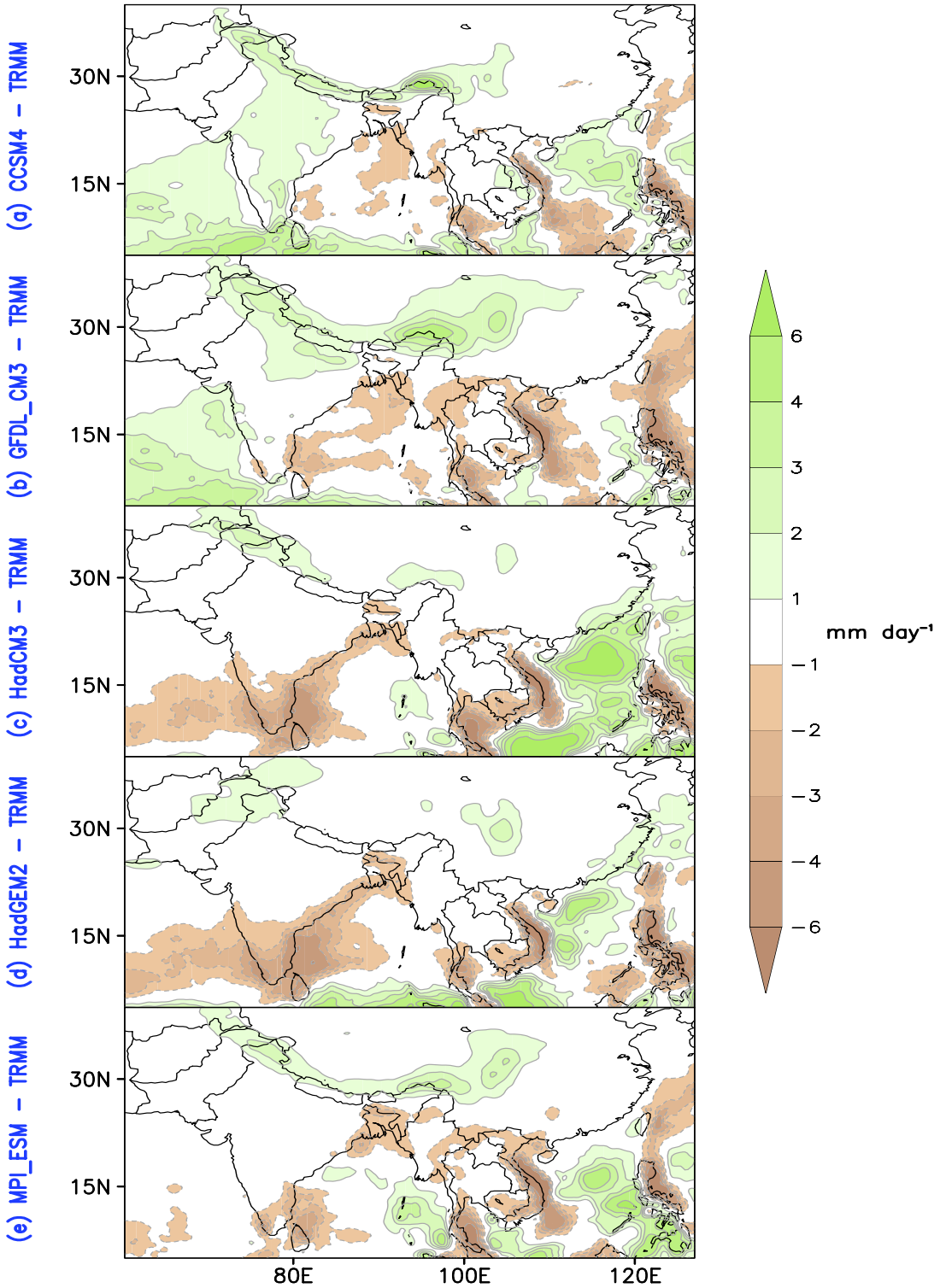

Figure 4.6. Climatological October through to December (OND) seasonal rainfall (1998–2005) in five IPCC–AR5 historical climate model simulations evaluated against TRMM 3b42v7 observations: (a) NCAR CCSM4, (b) NOAA GFDL-CM3, (c) UKMO HadCM3, (d) UKMO HadGEM2-ES, and (e) MPI-ESM-LR. Contour interval (C.I.) and shading threshold is 1.0 mm/day. The fields are displayed after two applications of smth9 in GrADS.

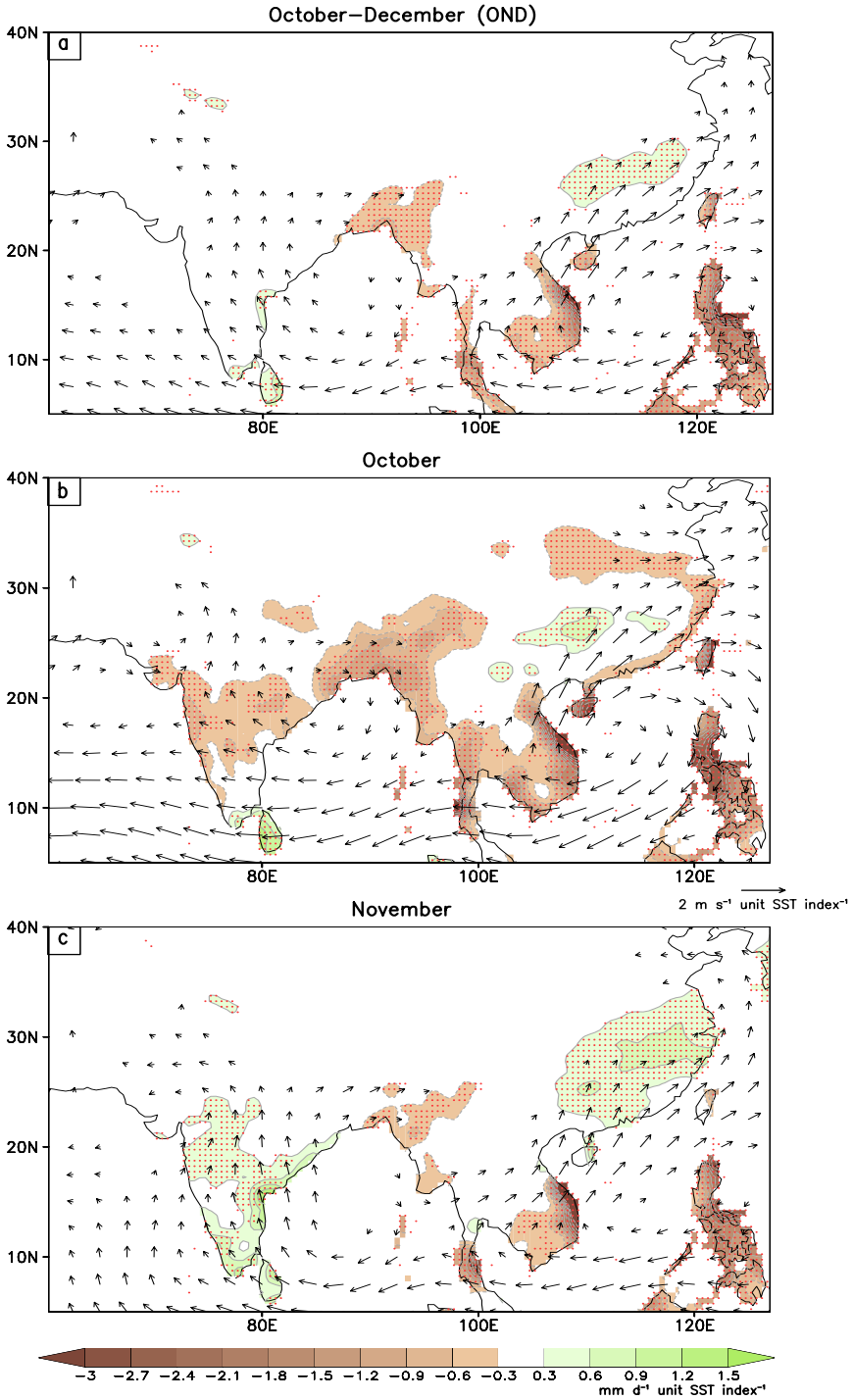

Figure 4.7. Characteristic influence of ENSO on winter monsoon rainfall and 925-hPa winds from observations for (a) the Oct.-Dec. season and the months of (b) October and (c) November. The influence is obtained from temporally leading regressions of rainfall (GPCC ver. 7) and winds (NCEP Reanalysis) on the winter (DJF averaged) Niño-3.4 SST anomaly index (constructed from HadISST1.1) in the post-IGY period (1958–2013). Green (brown) contours represent rainfall surplus (deficit). Contour interval is 0.3 mm/day/(unit of normalized SST index). Regressions are shown after one application of smth9 in GrADS. Regressions significant at the 95% level are stippled.

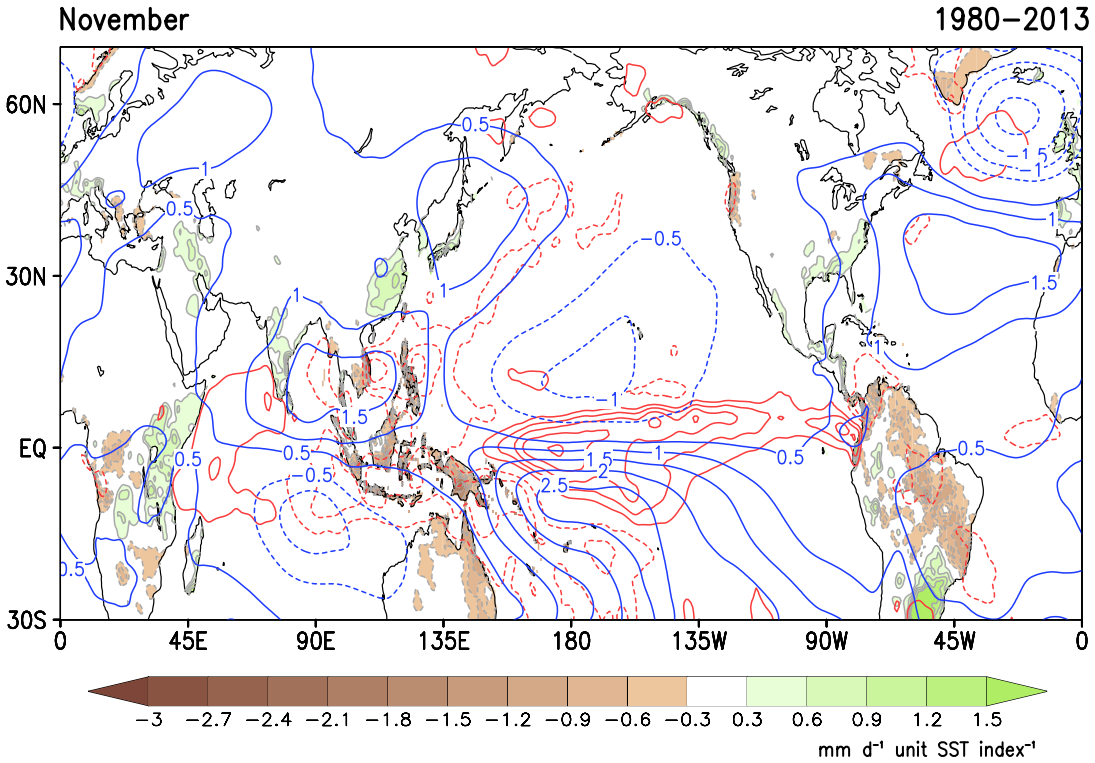

Figure 4.8. Changes in precipitation, vertically averaged (1000 to 100-mb) diabatic heating and 850-mb streamfunction for the month of November associated with ENSO. The response is obtained from temporally leading regressions of precipitation (GPCC ver. 7), vertically averaged diabatic heating and streamfunction (both fields diagnosed from ERA-Interim) on the winter (DJF-averaged) Niño-3.4 SST anomaly index for November (1980-2013). Green (brown) contours represent rainfall surplus (deficit); contour interval is 0.3 mm/day/unit SST index. Solid (dashed) red contours represent positive (negative) diabatic heating anomalies; contour interval is 0.2 K/day/unit SST index. Solid (dashed) blue contours represent positive (negative) 850-mb streamfunction anomalies; contour interval is 0.5 x 10^6 m^2/s/unit SST index.

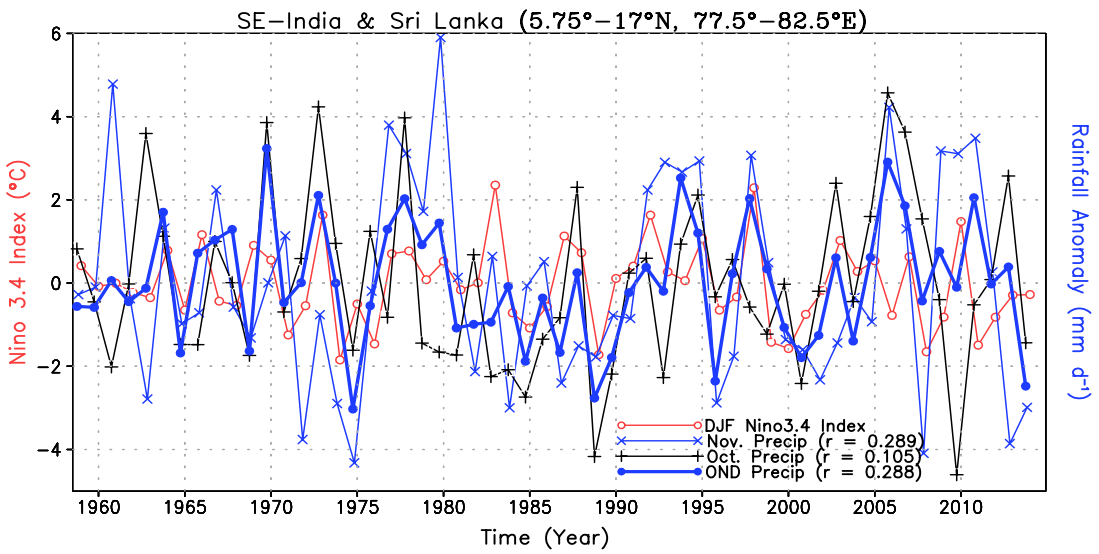

Figure 4.9. Correlation between Niño-3.4 SST index and NEM rainfall anomaly time series over Southeast Peninsular India & Sri Lanka. The Niño-3.4 SST index obtained from HadISST1.1 is in units of °C and GPCC ver. 7 observed rainfall anomaly is in units of mm/day. The period of analysis is 1958–2013. November rainfall anomaly is shown using solid blue line with multiplication sign marker, October using solid black line with plus sign marker, Oct.-Dec. (OND) using thick blue line with closed circles respectively. The rainfall anomaly in each case is the area-averaged value computed from continental grid points with standard deviation exceeding 1.5 mm/day. The correlation between the rainfall and Niño-3.4 SST time series are noted within parenthesis.

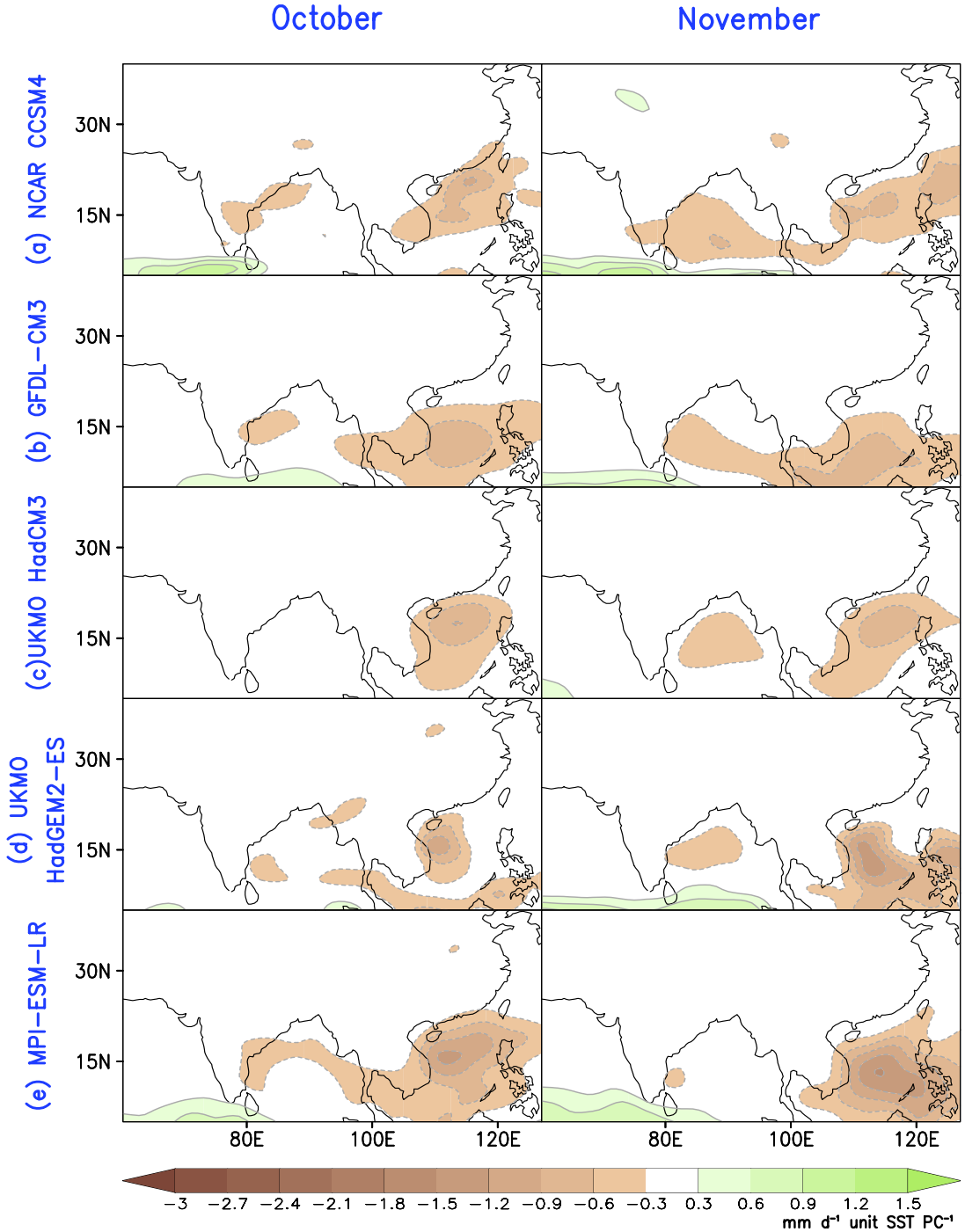

Figure 4.10. Characteristic influence of ENSO on winter monsoon rainfall in five IPCC–AR5 historical climate model simulations for the months of October and November: the influence is obtained from temporally-leading regressions of precipitation on the winter Niño-3.4 SST anomaly index (constructed from model SST simulations) in the post-IGY period (1958–2004). The average field across all ensemble members of each simulation is shown in (a)-(e). Green (brown) contours represent rainfall surplus (deficit). Contour interval is 0.3 mm/day/(unit SST index). Regressions are shown after one application of smth9 in GrADS.

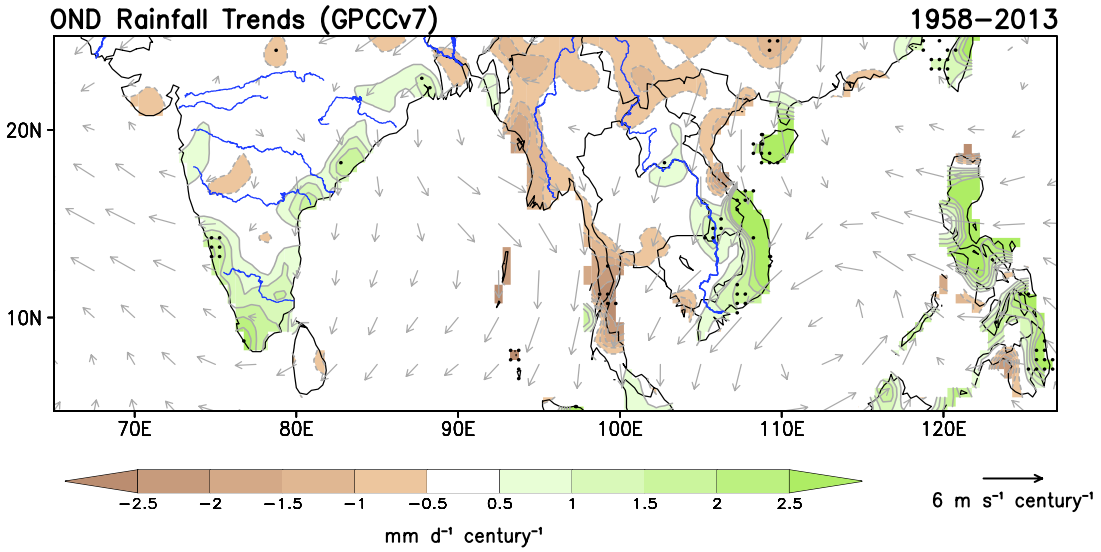

Figure 4.11. Linear trend in winter monsoon (OND) rainfall and 925-hPa winds (1958–2013). Rainfall trend is based on GPCC ver. 7 while winds are from NCEP Reanalysis. Green (brown) contours represent positive (negative) rainfall trend values. Contour interval and shading threshold is 0.5 mm/day/century. Rainfall trend is shown after one application of smth9 in GrADS. Trends significant at the 95% level are stippled in black.

Chapter 5: Summary and Discussion

5.1 Summary

This dissertation focuses on the quantitative assessment of the potential predictability of regional rainfall over South Asia based primarily on innovative spatiotemporal analyses of the 20th–21st century precipitation and SST observations. The work is motivated by the evaluative opportunities presented by the lack of observational analyses on the potential predictability of South Asian monsoon rainfall at longer lead times. Reliable and timely monsoon predictions have immense socioeconomic impact as summer rainfall remains a key determinant of the economic well-being of hundreds of millions in the still largely agrarian South Asia. The common theme across the studies presented in this dissertation is the examination of the role of climate drivers, namely SSTs in the global oceans, which evolve on a time scale slower than that of the monsoon system. This is exploited in the development of the statistical seasonal forecast model, with special emphasis on the *spatiotemporal* characterization of the predictors—the global SST modes, instead of the customary consideration of just their spatial patterns.

The first study, shown in Chapter 2, utilizes the extended-empirical orthogonal function technique to characterize the SST variability in the global oceans with particular interest in the space-time structure of the multidecadal modes, especially its rendition in a spatiotemporal analysis that has no *a priori* basin preference. It is found that:

- The evolution-centric analysis effectively discriminates between the biennial, interannual, decadal variability modes, as well as the nonstationary secular trend. All the constituent SST modes are extracted in a single step, without any additional filtering and potential aliasing of the SST record.
- An array of *sensitivity* and *mode-physicality* tests based on analogs and significantly augmented fish recruitment data (from both the Pacific and the Atlantic basins) yield robustness to the analysis.
- Significant temporal *lead-lag* links exist between the Pacific and Atlantic basins in the context of the evolution of the multidecadal SST modes: For example, a positive PDV-NP (equivalent to a –negative PDO) evolves in the Atlantic basin into a negative LF-NAO in 6.5 years, which in the following 16 years evolves into a negative AMO. The AMO negative phase, interestingly, evolves in the Pacific into a negative PDV-NP, i.e., a phase-reversed PDV-NP.
- The phase-reversal of PDV-NP (or LF-NAO or AMO) arises from both intra-basin and inter-basin interactions; a preliminary investigation of the latter is reported. The phase-reversal time (~35 years), obtained from summing of intervening lags, is the same for all 3 modes, and in accord with the ~70-year oscillation timescale estimated from the autocorrelation structure of the related principal components.

Based on the above analysis, Chapter 3 presents a statistical model to forecast the South Asian summer monsoon rainfall distribution using the extracted modes of SST variability (in Chapter 2) in the Pacific and Atlantic basins as predictors. The study also examines the relative contributions of the two basins to the observed SST-based monsoon predictability. The principal findings of this chapter are:

- The SST anomalies in the Pacific, Atlantic and Indian Ocean basins are established as viable predictors of the summer monsoon rainfall. The statistical model allows the reconstruction of observed rainfall anomalies from both *contemporaneous* and *SST-leading* regressions of summer rainfall on the leading modes of SST variability permitting the integration of the influence of the full spectrum of SST variability on rainfall.
- The undertaken reconstruction provides a *quantitative assessment* of the potential predictability of summer monsoon rainfall anomalies – the maximum predictable summer rainfall signal (amount, distribution) over South Asia from prior SST information – at *various seasonal leads*, and notably, at *SST-mode resolution*.
- Hindcast results for an independent verification period (2009–2016) demonstrates high forecast skill, explaining 80–100% of the observed variability and exhibiting correlation values of ~0.6 over core monsoon regions – the Indo-Gangetic Plain and southern peninsular India.
- The skill of the SST-based statistical forecast model is found to be competitive (if not superior) with the dynamical forecast models based on the real-time verification of the 2019 summer monsoon season rainfall distribution.

Interannual variability of rainfall is then examined in Chapter 4 for the northeast winter monsoon, which brings the bulk of annual rainfall to southeastern peninsular India, Sri Lanka, and the neighboring Southeast Asian countries during the months October–December. In this study, we:

- Objectively demarcate the winter monsoon region from analysis of the timing of peak monthly rainfall using both in-situ (GPCC) and remotely sensed (TRMM)

precipitation data.

- Document the monthly evolution of the NEM from analysis of rainfall, sea level pressure, and the low-level winds. An intersting finding here is the asynchronicity in the establishment of northeasterlies over the Bay of Bengal and the South China Sea; the northeasterlies appear over the Bay of Bengal in November, i.e., a month later than over South China Sea.
- Show that the El Niño–Southern Oscillation's impact on NEM rainfall is significant, leading to stronger NEM rainfall over southeastern peninsular India and Sri Lanka but diminished rainfall over Thailand, Vietnam, and the Philippines. The impact *varies subseasonally*, being weak in October and strong in November. The positive anomalies over peninsular India are generated by anomalous anticyclonic flow centered over the Bay of Bengal, which is forced by an El Niño–related reduction in deep convection over the Maritime Continent.
- Show that the NEM rainfall distribution in the historical 20th-century climate simulations informing the IPCC-AR5 exhibit varied deficiencies, and a markedly weaker (and often unrealistic) ENSO–NEM rainfall relationship.

5.2 Discussion

The Atlantic–Pacific basin links among the recurrent modes of multidecadal SST variability are targeted in this observational analysis. The intra and inter-basin links are schematically summarized in Fig. 5.1. The black (red) connecting lines in the main loop link similar (opposite) phases of the lead-lagged modes. One (or an odd number) of red-line links in a closed loop lead to phase-reversal, permitting cycling

through both phases of all the linked modes. For example, the +*ve* phase of PDV-NP (with its Atlantic vestiges) evolves into a –*ve* LF-NAO in 6.5 years, which in the following 16 years evolves into a –*ve* AMO; interestingly, the –*ve* AMO evolves in the Pacific basin into a –*ve* PDV-NP, i.e., a full clockwise cycle leads to a phase-reversal of PDV-NP! The related inter-basin evolutions of SST and SLP (Fig. 2.10) indicate a role for both intra-basin processes and inter-basin interactions in the phase-reversal of the PDV-NP (or LF-NAO or AMO, for that matter) – the latter, a new finding. The phase-reversal time – about 35 years, obtained by summing, clockwise, the lags in the main loop – would be the same for the LF-NAO, AMO, and the PDV-NP modes in this scheme.[15] The schematic also depicts, outside of the main loop, a same-phase LF-NAO-to-AMO transition over 6.5 years related to AMO's decadal pulses, several of which populate each of its multidecadal phase. This 6-7-year lag is consistent with the findings in Nigam et al. (2018) on the evolution and phase-reversal of AMO's decadal pulses.

The inter-basin links noted above are not an artifact of the statistical analysis technique used to analyze spatiotemporal variability. For one, the PCs are extensively vetted from intercomparison with other related indices (e.g., PDO, NPGO, AMO) and from physicality assessments through correlations with the fish recruitment records – which were augmented vis-à-vis Hare and Mantua (2000) in the Pacific, and newly assembled for the Atlantic. Even more, the inter-basin links are patent in the lead-lag correlations of the widely used AMO-NOAA (Enfield et al. 2001) and PDO (Mantua

[15] The spatiotemporal analysis of SST variations also yielded the Sub-Arctic mode which was lowest ranked in terms of explained variance, and whose evolution is thus not documented. Although its interactions are indicated in the schematic, they are not the focus as the origin of this high-latitude SST variability mode remains enigmatic.

et al. 1997) indices, i.e., in the variability markers completely independent of the present analysis! Fig. 5.2 shows the lead-lag correlations of these indices (in red) along with those of corresponding PCs (in black; PDV-NP's sign is flipped to facilitate comparison). The *simultaneous* (i.e., zero-lag) correlation of the two PCs (and even indices) is near-zero, suggesting a lack of relationship; an evaluation of the *lead-lag* correlations, however, suggests otherwise: The positive correlation peak (~0.67) at $t \approx 21$ years implies that PDO index leads the AMO one by 21 years while the negative peaks (~−0.57) imply that AMO index's *negative* phase leads the PDO index by 12 (and 19) years.[16]

The primary contribution of this dissertation is in the determination of potential predictability and prediction skill of the SST-based statistical model for the South Asian summer monsoon. The two motivating questions for the monsoon predictability work described in Chapter 3 – the central theme of this dissertation – are re-examined below.

a. *What is the potential predictability of summer monsoon rainfall at longer forecast lead times?*

The first attempt at long range forecasting of the Indian summer monsoon rainfall was made more than a century ago by Blanford (1884). More recently, seasonal monsoon forecasting has received significant research attention in the past four decades through both statistical and dynamical modeling studies. However, attainment of the desirable prediction skill remains elusive. The work described in this thesis is not the

[16] The 12-year lead was noted in Figs. 2.10 and 5.1, but not the 19-year one. The lead-lag correlations of the PCs are similar to those of the indices but for notable differences when $t < -12$ years; in particular, the PCs do not support the indices-based finding of a 19-year-lead of AMO's negative phase over the PDO.

first to advocate for the seasonal forecasting using lower-tropospheric forcing such as SSTs as predictors. Sahai et al. (2003, 2008) and Rajeevan et al. (2007) have used global SSTs for long lead prediction of the Indian monsoon. This thesis expands on these previous studies primarily in three ways. First, this analysis focuses on the evolutionary aspect of recurrent SST variability and is able to extract secular warming (through a nonstationary secular trend) and natural variability modes from a single analysis, as opposed to the more common residual estimation of either component. Second, the forecast model utilizes contribution of decadal-multidecadal modes in addition to the customary consideration of interannual variability. Lastly, instead of selecting SST predictors from different geographical locations with varying temporal lags, this study allows the full expression of inter-basin linkages among constituent modes in the global domain (20°S-80°N)—a primary target of Chapter 2.

Chapter 3 provides a quantitative assessment of the SST-based monsoon predictability at lead times of *1-season* to *3-season*—the first of its kind from observationally based studies? Reconstruction schemes using SST lead times of *1-season* and *2-season* are shown to explain 60% of the observed variance in the historical period, with high correlation (~0.5) with the observed rainfall anomalies over the Indo-Gangetic Plain and southern peninsular India, i.e., regions where monsoonal rains are considered as the "*backbone*" of the agrarian economy.

b. Which are the primary drivers of monsoon variability?

The current body of work contains an attempt to utilize local and remote SST forcing of monsoon rainfall, in view of IMD's National Monsoon Mission – a focused applied science endeavor – potentially capable of delivering a quantum jump in the

accuracy of forecasts, fulfilling an overdue scientific promise. SSTs affect both regional and faraway climate systems through modulation of surface fluxes, convection and clouds, and moisture transports, among others, with the influence being two-way, as SST responds to atmospheric circulation and near-surface meteorology as well. The contribution of Pacific SST anomalies on monsoonal forcing is shown to be more influential than Atlantic ones.

Are there other lower-tropospheric drivers that will add to the predictability skill? Li et al. (2016a) show evidence of a connection between higher sea-surface salinity (SSS) in the North Atlantic Ocean and increased rainfall on land in the African Sahel. High springtime SSS in the western North Atlantic is also demonstrated to be correlated with high summer rainfall in the U.S. Midwest (Li et al. 2016b). Can SSS potentially augment SST-based monsoon predictions? Are such salinity signals across the globe independent of SST forcing? Perhaps, but not entirely, because SST-induced downwelling can leave warm, more saline waters at the surface. Hence, the effect of SSS is already incorporated in this SST-based prediction scheme. Nevertheless, a diagnosis of the magnitude of the residual SSS signal needs to be performed by removing the salinity regressions of the modes of SST variability from the total SSS field.

Given its seasonal persistence, the Himalayan snow cover has been suggested as an empirical predictor of the intensity and advent of the southwest monsoon (Blanford 1884; Walker 1910; Hahn and Shukla 1976). A negative correlation between the pre-monsoon Himalayan snow cover depth and the amount of summer monsoon rainfall over India has been suggested in these past studies. The brevity of available

data records, however, is a barrier in context of snow cover-based statistical predictions. Other key questions include: Given the strong influence of ENSO on summer monsoon, what is the nature of snow cover anomalies during ENSO years? How strong is the observed monsoon–snow cover relationship during non–ENSO years? Fasullo (2004) used NOAA/NESDIS version 2 satellite retrieval data from 1967 to 2001 to examine the snow cover anomaly patterns during both anomalous monsoon years and ENSO events. The study concluded that ENSO has a strong influence on the monsoon–snow cover relationship. The SST-based monsoon prediction scheme presented here thus implicitly accounts for the monsoon–snow cover relationship in that sense.

5.3 Future work

It is hoped that the results presented in this dissertation will invigorate further statistical prediction efforts of regional rainfall and provide specific prediction targets for dynamical model performance evaluation. The future research avenues are detailed below.

5.3.1 Subseasonal prediction: MJO's predictive influence on rainfall

While the work presented in this dissertation aims at seasonal prediction and assessment of seasonal monsoon predictability, its *sub-seasonal* variations—active and break phases remains unaccounted in our empirical model. An important source of intraseasonal variability in the global tropics is the Madden-Julian Oscillation (MJO; Madden and Julian 1971, 1972), which is a natural component of the coupled ocean-atmosphere system.

Several studies have noted MJO's important role in generating the active and break spells of the summer monsoon (Lau et al. 1998; Waliser et al. 2003; Goswami 2005), and its influence on the monsoon onset and retreat timings (Hendon and Liebmann 1990; Sperber et al. 2000; Annamalai and Sperber 2005; Waliser 2006). Fig. 5.3 shows that MJO activity can robust during boreal summer, and not just during winter. A notably strong episode is seen in July 2015. In 2016 too, MJO activity in summer is not any less intense than during the following winter. Preliminary results for the MJO's contemporaneous influence on *pentad* rainfall, computed separately for each summer monsoon month, is shown in Fig. 5.4. While regressions are notably stronger in August, their structure, interestingly, exhibits a broad pattern – a wetter central subcontinent (between and around the Narmada and Godavari rivers) and west coast, sandwiched between a drier northern Gangetic Plain and a drier southeastern peninsula.

A moderate to strong MJO episode (e.g., amplitude ≥ 2.5, as in Fig. 5.3) can be quite influential on rainfall. For example, the MJO signal in August's rainfall can easily be as large as 4-5 mm/day in central India where green colors are saturated in Fig. 5.4 (at 2 mm/day); note, the signal is obtained by multiplying the regressions by the MJO amplitude. Hence, a skillful empirical prediction of the MJO's lagged influence on pentad resolution rainfall with lead times of 2-4 weeks can clearly advance subseasonal forecasting efforts. This will enable our seasonal forecasting effort to be extended to the subseasonal realm through the issuance of rainfall distribution forecasts for the individual months of June–September.

5.3.2 Dynamical model performance evaluation

Another potential research problem is the evaluation of the predictive skill of the dynamical models, for example, the NCEP CFSv2, in predicting the SST-related summer monsoon rainfall variations over South Asia using the SST-based potential predictability targets presented in this dissertation. Pillai et al. (2018) recently assessed the potential predictability of boreal summer monsoon rainfall using CFSv2-T382 hindcasts. The potential predictive skill of the model was evaluated at different temporal lead times, where the tropical SST–rainfall relationship was assessed using the area-averaged Indian summer monsoon rainfall (ISMR) index. However, the area-averaged index incorporates the possibility of combining diverse regions with dissimilar background rainfall climatology and interannual variability.

Hence, the predictive skill needs to be evaluated from analysis of the CFSv2 seasonal hindcasts (initiated at various lead times) using the corresponding SST-based predictive signal diagnosed from observational analysis. The spatiotemporal SST analysis will need be repeated on century long CFSv2 simulations. Intercomparison of the simulated SST modal structures and related precipitation (and circulation) regressions with their observational counterparts will facilitate identification of the model shortcomings at modal resolution, focusing model improvement efforts.

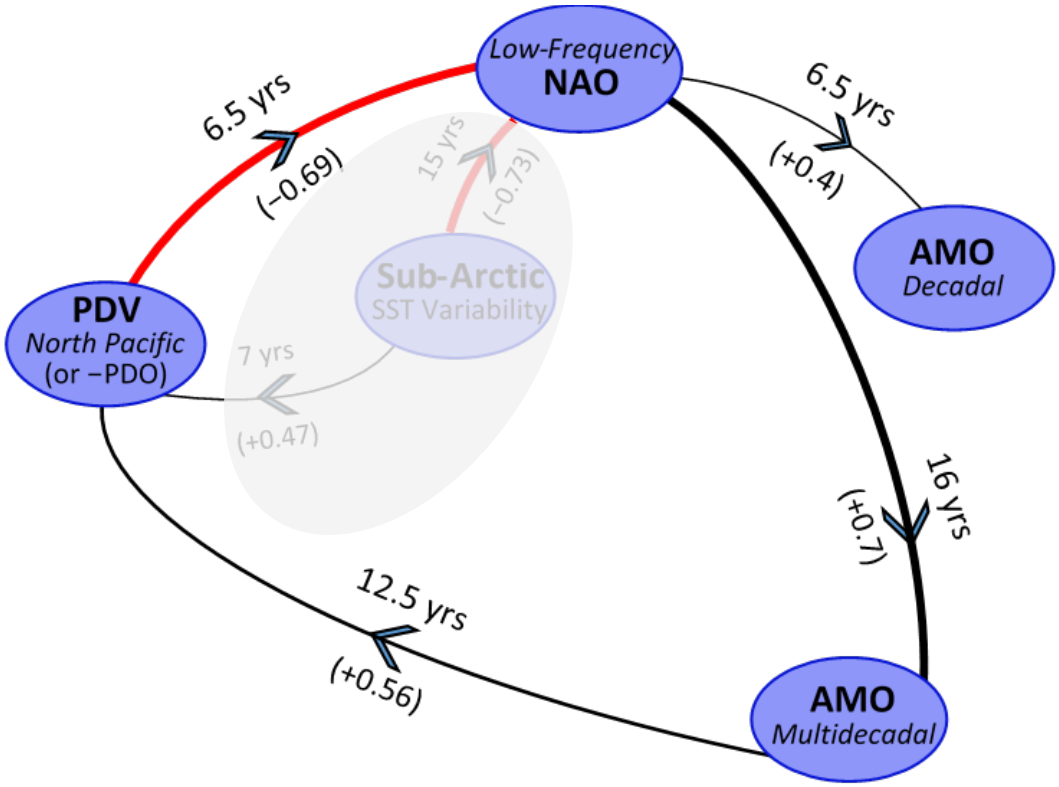

Figure 5.1. *Schematic of Intra and Inter-Basin Interactions*: Spatiotemporal analysis of global SST variations during 1900-2017 reveals the Pacific and Atlantic basins to be linked. The main loop represents the linkage of multidecadal variabilities in the Atlantic (Low-Frequency NAO and AMO-Multidecadal), and of the Atlantic and Pacific (PDV-North Pacific) basins. Black (red) line connects similar (opposite) phases of the lead-lagged modes, with line-thickness reflecting, qualitatively, the lag-correlation strength. Note, one (or an odd number) of red-line links in a closed loop indicate phase-reversal, permitting cycling through both phases of represented variabilities. For example, the positive phase of PDV-NP evolves in the Atlantic basin into a negative LF-NAO in 6.5 years, which in the following 16 years evolves into a negative AMO; interestingly, the negative AMO evolves in the Pacific basin into a negative PDV-NP, i.e., a full clockwise cycle leads to a phase-reversal of PDV-NP! The phase-reversal time – about 35 years, obtained by summing, clockwise, the lags in the main loop – would be the same for the LF-NAO, AMO, and the PDV-NP modes in this scheme. The spatiotemporal analysis of SST variations also yielded the Sub-Arctic mode which was lowest ranked in terms of explained variance, and whose evolution is thus not documented. Although its interactions are indicated in the schematic, they are not the focus as the origin of this high-latitude SST variability mode remain enigmatic at this time. The schematic also depicts, outside of the main loop, a LF-NAO-to-AMO transition over 6.5 years related to AMO's decadal pulses, several of which populate each of its multidecadal phase.

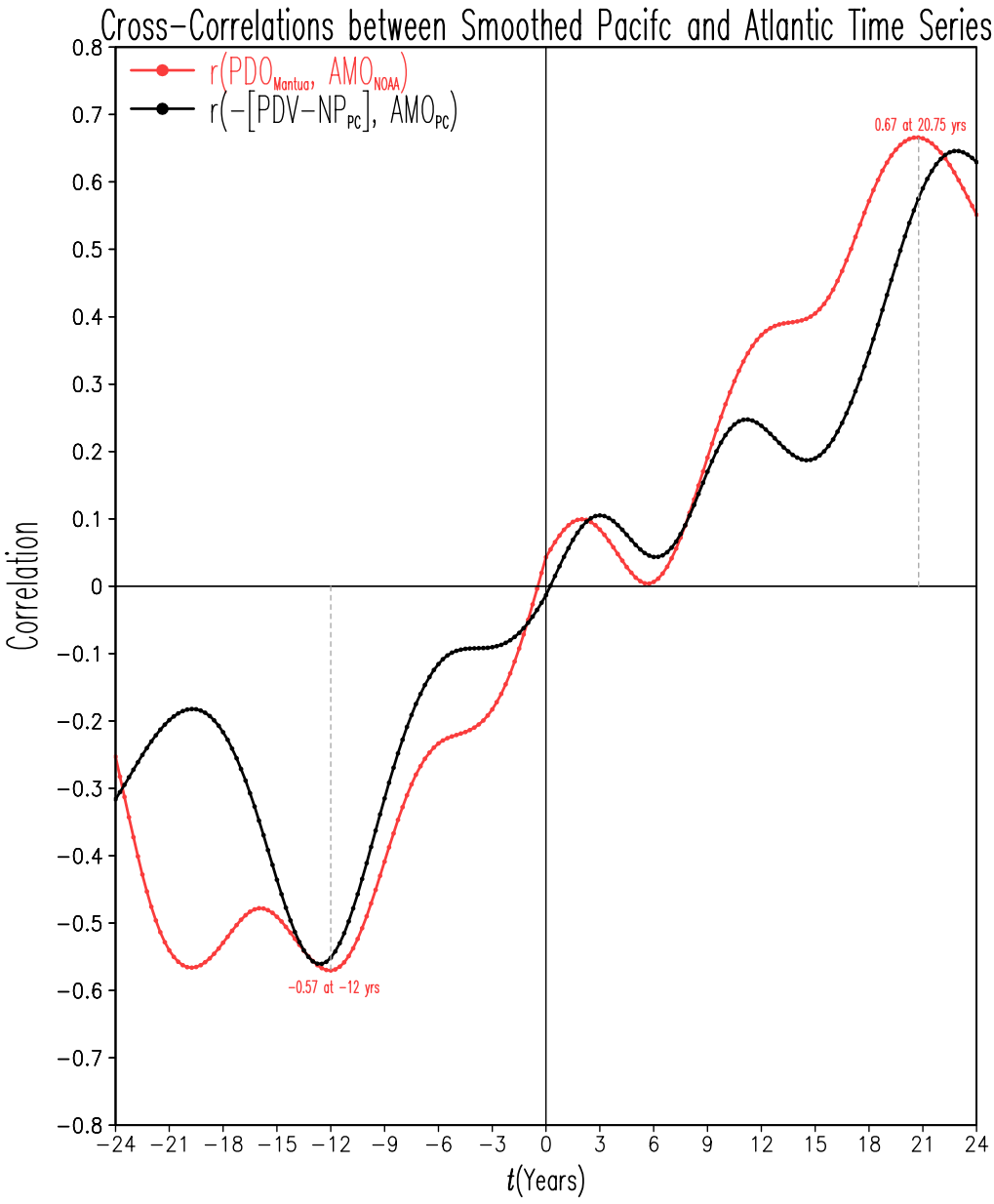

Figure 5.2. Lead-lag cross-correlations of the smoothed (LOESS-10%) Pacific Decadal Oscillation index (PDO, Mantua et al. 1997) and the Atlantic Multidecadal Oscillation index (AMO-NOAA, Enfield et al. 2001) are in red, while those of the related SST principal components (PCs) – AMO and the negative PDV-NP – both similarly smoothed, are in black; correlations were computed over 1900-2017 and displayed using a lead-lag convention noted in Fig. 2.9. The simultaneous (i.e., zero-lag) correlation of the two PCs (and even indices) is near-zero, suggesting a lack of relationship; additional evaluation of lead-lag correlations, however, suggests otherwise: The positive correlation peak (~0.67) at t≈21 years implies that PDO leads the AMO by 21 years while the negative peaks (~−0.57) imply that AMO's negative phase leads the PDO by 12 (and 19) years; the 12-year lead was noted in Figs. 2.10 and 5.1, but not the 19-year one. Lead-lag correlations of the PCs are similar to those of the indices but for some differences when $t < -12$ years; in particular, the PCs do not support the indices-based finding of a 19-year-lead of AMO's negative phase over the PDO.

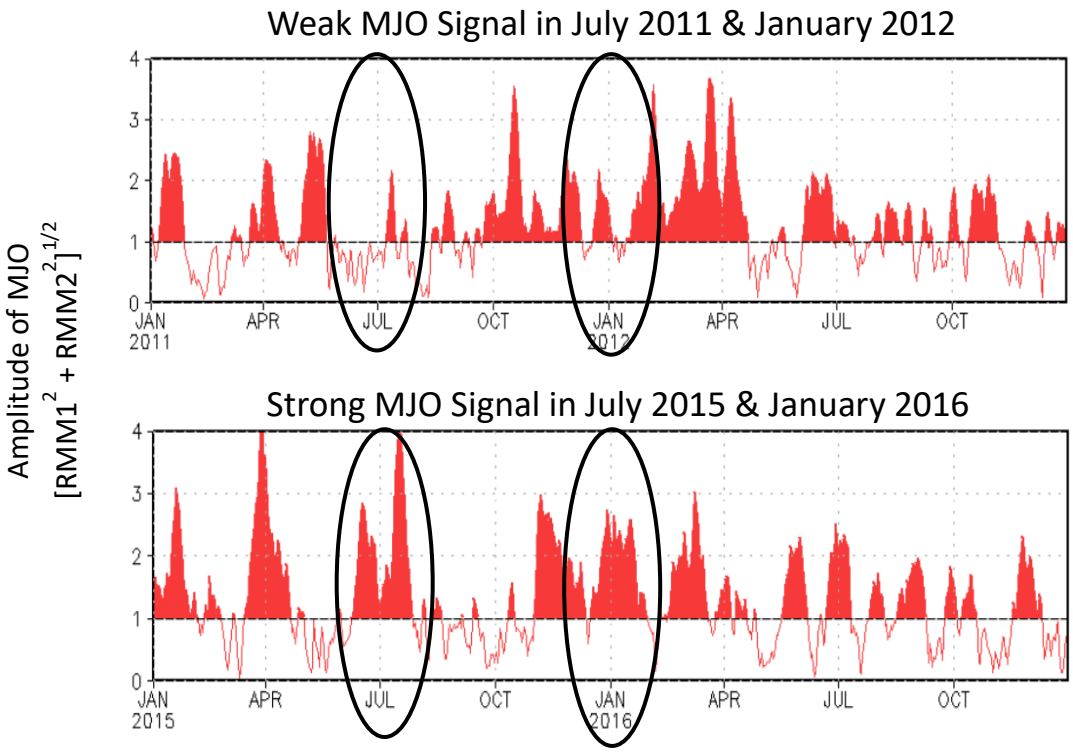

Figure 5.3. *Daily MJO index amplitude*, i.e., $[RMM1^2 + RMM2^2]^{½}$ during 2011–2012 (upper) and 2015–2016 (bottom). Weak (strong) MJO activity is highlighted in the upper (lower) panel. Index magnitude ≥ 1.0 is shaded in red. Data (and figures) are from NOAA's Climate Prediction Center website.

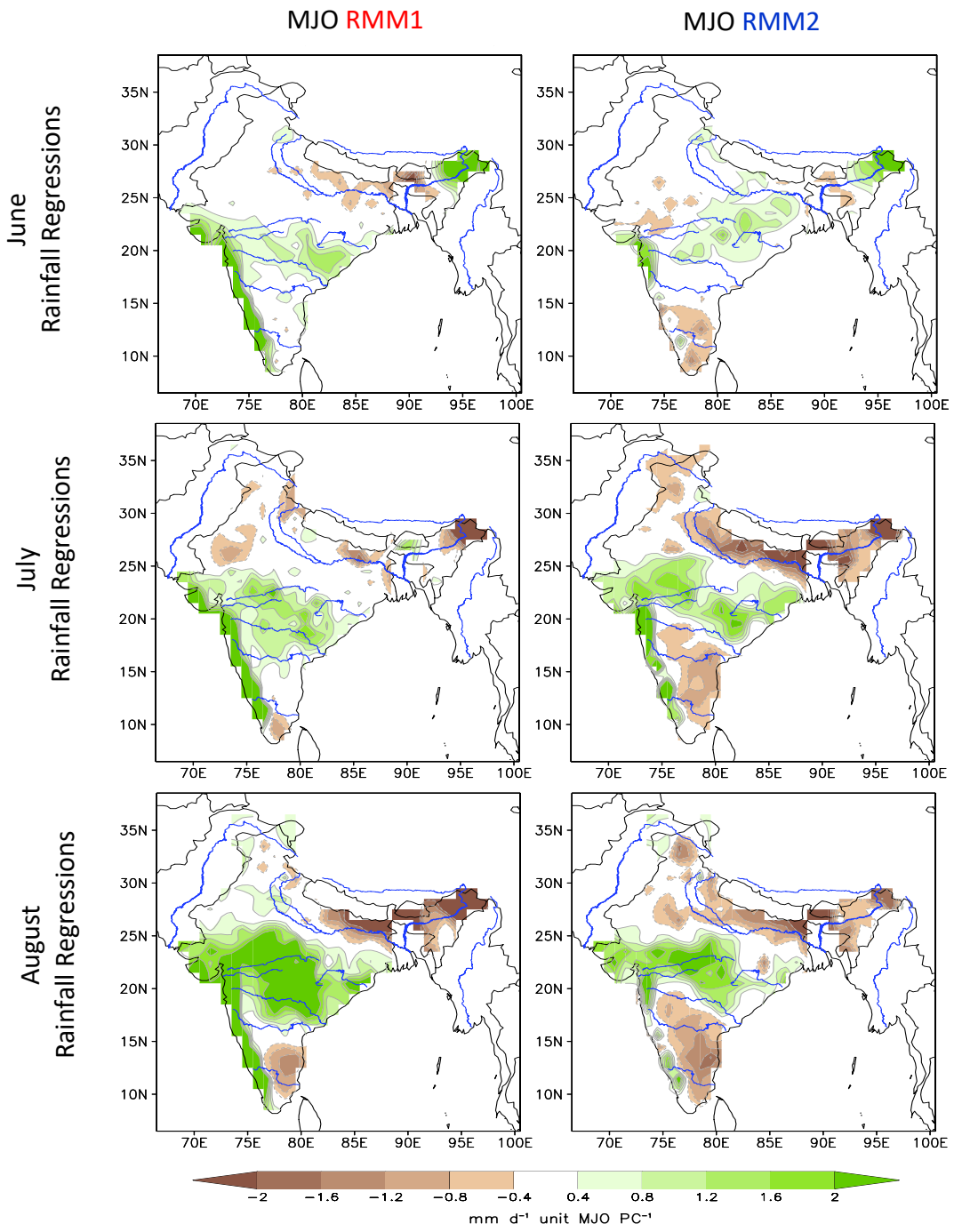

Figure 5.4. *MJO's impact on monsoon rainfall*, obtained from contemporaneous regressions of the IMDv4 rainfall (1°× 1°; pentad) on MJO indices RMM1 (left) and RMM2 (right); regression period 1979–2014. Pentad regressions are computed separately for the month of June (top), July (middle), and August (bottom). Contour-interval is 0.4 mm/day/unit index. Green (brown) shading denotes positive (negative) rainfall anomalies starting at 0.4 mm/day/unit index. Pentad resolution RMM1 and RMM2 were generated from the Wheeler and Hendon (2004) daily indices, downloaded from the Australian Bureau of Meteorology website.

Bibliography

Akasaka, I., 2010: Interannual variations in seasonal march of rainfall in the Philippines. *Int. J. Climatol*., **30**, 1301–1314.

Akasaka, I., W. Morishima, and T. Mikami, 2007: Seasonal march and its spatial difference of rainfall in the Philippines. *Int. J. Climatol*., **27**, 715–725.

Alexander, M. A., I. Bladé, M. Newman, J. R. Lanzante, N.-C. Lau, and J. D. Scott, 2002: The atmospheric bridge: The influence of ENSO teleconnections on air–sea interaction over the global oceans. *J. Climate*, **15**, 2205–2231.

Allan, R., and T. Ansell, 2006. A New Globally Complete Monthly Historical Gridded Mean Sea Level Pressure Dataset (HadSLP2): 1850 2004. *J. Climate*, **19**, 5816-5842.

Alvarez-Garcia, F., M. Latif, and A. Biastoch, 2008: On multidecadal and quasi-decadal North Atlantic variability. *J. Climate*, **21**, 3433–3452.

Annamalai, H., and K. R. Sperber, 2005: Regional heat sources and the active and break phases of boreal summer intraseasonal (30–50 day) variability. *J. Atmos. Sci*., **62**, 2726–2748.

Bader, J., and M. Latif, 2003: The impact of decadal-scale Indian Ocean sea surface temperature anomalies on Sahelian rainfall and the North Atlantic Oscillation. *Geophys. Res. Lett.*, **30**.

Barlow, M., S. Nigam, and E. H. Berbery, 2001: ENSO, Pacific decadal variability, and U.S. summertime precipitation, drought, and stream flow. *J. Climate*, **14**, 2105–2127.

Becker, A., and Coauthors, 2013: A description of the global land-surface precipitation data products of the Global Precipitation Climatology Centre with sample applications including centennial (trend) analysis from 1901–present. *Earth Syst. Sci. Data*, **5**, 71–99.

Bjerknes, J., 1969: Atmospheric teleconnections from the equatorial pacific. *Mon. Wea. Rev*., **97**, 163-172.

Bjerknes, J., 1964: Atlantic air-sea interaction. *Advances in geophysics*, Vol. 10 of, Elsevier, 1–82.

Blanford, H. H., 1884: On the connection of Himalayan snowfall and seasons of drought in India, *Proc. R. Soc. London*, **37**, 3– 22.

Bollasina, M. A., Y. Ming, and V. Ramaswamy, 2011: Anthropogenic aerosols and the weakening of the South Asian summer monsoon. *Science*, **334**, 502–505.

Bollasina, M., and S. Nigam, 2009: Indian Ocean SST, evaporation, and precipitation during the South Asian summer monsoon in IPCC-AR4 coupled simulations. *Climate Dyn.*, **33**, 1017.

Bond, N. A., M. F. Cronin, H. Freeland, and N. Mantua, 2015: Causes and impacts of the 2014 warm anomaly in the NE Pacific. *Geophys. Res. Lett.*, **42**, 3414–3420.

Booth, B.B., N.J. Dunstone, P.R. Halloran, T. Andrews, and N. Bellouin, 2012: Aerosols implicated as a prime driver of twentieth-century North Atlantic climate variability. *Nature*, **484**(7393), 228.

Chafik, L., S. Häkkinen, M. H. England, J. A. Carton, S. Nigam, A. Ruiz-Barradas, A. Hannachi, and L. Miller, 2016: Global linkages originating from decadal

oceanic variability in the subpolar North Atlantic. *Geophys. Res. Lett*., **43**, 10909–10919.

Chakraborty, A., and T. N. Krishnamurti, 2006: Improved seasonal climate forecasts of the South Asian summer monsoon using a suite of 13 coupled ocean–atmosphere models. *Mon. Weather Rev*., **134**, 1697–1721.

Chan, S. C., and S. Nigam, 2009: Residual diagnosis of diabatic heating from ERA-40 and NCEP reanalyses: Intercomparisons with TRMM. *J. Climate*, **22**, 414–428.

Charney, J. G., and J. Shukla, 1981: *Predictability of monsoons. Monsoon Dynamics, J. Lighthill and RP Pearce, Eds*. Cambridge University Press,.

Chen, T.-C., J.-D. Tsay, M.-C. Yen, and J. Matsumoto, 2012: Interannual variation of the late fall rainfall in central Vietnam. *J. Climate*, **25**, 392–413.

Chen, T.-C., and M.-C. Yen, 1994: Interannual variation of the Indian monsoon simulated by the NCAR Community Climate Model: Effect of the tropical Pacific SST. *J. Climate*, **7**, 1403–1415.

Chen, X., J.M. Wallace, and Ka-Kit Tung, 2017. Pairwise-rotated EOFs of global SST. *J. Climate*, **30**, 5473–5489.

Chikamoto, Y., M. Kimoto, M. Watanabe, M. Ishii, and T. Mochizuki, 2012: Relationship between the Pacific and Atlantic stepwise climate change during the 1990s. *Geophys. Res. Lett*., **39**, L21710.

Chung, C., S. Nigam, and J. A. Carton, 2002: SST-forced surface wind variability in the tropical Atlantic: An empirical model. *J. Geophys. Res*., **107**, 4244.

Clement, A., K. Bellomo, L.N. Murphy, M.A. Cane, T. Mauritsen, G. Rädel, and B. Stevens, 2015: The Atlantic Multidecadal Oscillation without a role for ocean circulation. *Science*, **350**(6258), 320-324.

Cleveland, W.S., and C.L. Loader, 1996: Smoothing by local regression: Principles and methods. *Statistical Theory and Computational Aspects of Smoothing*, W. Haerdle and M. G. Schimek, Eds., Springer, 10–49.

Czaja, A., A. Robertson, and T. Huck, 2003: The role of coupled processes in producing NAO variability. *N. Atl. Oscil. Clim. Significance Environ. Impact Geophys Monogr*, **134**, 147–172.

Dai, N., S. Nigam, and P.A. Arkin, 2018: Diabatic heating differences in ERA-Interim, MERRA-2 and CFSR atmospheric reanalyses, and intercomparison of the reanalyses and CMIP5 ENSO heating distribution, to be submitted to *Climate Dyn*.

De Coetlogon, G., and C. Frankignoul, 2003: On the persistence of winter sea surface temperature in the North Atlantic. *J. Climate*, **16**, 1364–1377.

De, U.S., and R. K. Mukhopadhyay, 1999: The effect of ENSO/Anti-ENSO on northeast monsoon rainfall. *Mausam*, **50**: 343-354.

Dee, D. P., and Coauthors, 2011: The ERA-Interim reanalysis: Configuration and performance of the data assimilation system. *Quart. J. Roy. Meteor. Soc*., **137**, 553–597.

DelSole, T., and J. Shukla, 2012: Climate models produce skillful predictions of Indian summer monsoon rainfall. *Geophys. Res. Lett*., **39**.

DelSole, T., and J. Shukla, 2002: Linear prediction of Indian monsoon rainfall. *J. Climate*, **15**, 3645–3658.

Delworth, T. L., F. Zeng, L. Zhang, R. Zhang, G. A. Vecchi, and X. Yang, 2017: The central role of ocean dynamics in connecting the North Atlantic Oscillation to the extratropical component of the Atlantic Multidecadal Oscillation. *J. Climate*, **30**, 3789–3805.

Delworth, T., S. Manabe, and R.J. Stouffer, 1993: Interdecadal variations of the thermohaline circulation in a coupled ocean-atmosphere model. *J. Climate*, **6**, 1993-2011.

Deser, C., M. Alexander, S. Xie, and A. Phillips, 2010: Sea surface temperature variability: patterns and mechanisms. *Annu. Rev. Mar. Sci*., **2**, 115–43.

Deser, C., A. S. Phillips, and J. W. Hurrell, 2004: Pacific interdecadal climate variability: Linkages between the tropics and the North Pacific during boreal winter since 1900. *J. Climate*, **17**, 3109–3124.

Deser, C., M. Alexander, and M. Timlin, 2003: Understanding the persistence of sea surface temperature anomalies in midlatitudes. *J. Climate*, **16**, 57–72.

Deser, C., and M. Blackmon, 1995: On the relationship between tropical and North Pacific sea surface temperature variations. *J. Climate*, **8**, 1677–80.

Dhar, O. N., and P. R. Rakhecha, 1983: Foreshadowing northeast monsoon rainfall over Tamil Nadu, India. *Mon. Wea. Rev.,* **111,** 109–112.

Di Lorenzo, E., and Coauthors, 2008: North Pacific Gyre Oscillation links ocean climate and ecosystem change. *Geophys. Res. Lett.*, **35**.

Dix, M. R., and B. G. Hunt, 1995: Chaotic influences and the problem of deterministic seasonal predictions. *Int. J. Climatol.*, **15**, 729–752.

Dorigo, W., R. de Jeu, D. Chung, R. Parinussa, Y. Liu, W. Wagner, and D. Fernández-Prieto, 2012: Evaluating global trends (1988–2010) in harmonized multi-satellite surface soil moisture. *Geophys. Res. Lett*., **39**.

Drews, A. and R.J. Greatbatch, 2016: Atlantic multidecadal variability in a model with an improved North Atlantic Current. *Geophys. Res. Lett.*, **43**(15), 8199-8206.

Endo, H., and A. Kitoh, 2016: Projecting changes of the Asian summer monsoon through the twenty-first century. In L.M.V. Carvalho and C. Jones (Eds.), *The Monsoons and Climate Change: Observations and Modeling*, 47–66, Springer.

Endo, N., J. Matsumoto, and T. Lwin, 2009: Trends in precipitation extremes over Southeast Asia. *SOLA*, **5**, 168–171.

Enfield, D. B., A. M. Mestas-Nuñez, and P. J. Trimble, 2001: The Atlantic multidecadal oscillation and its relation to rainfall and river flows in the continental US. *Geophys. Res. Lett.*, **28**, 2077–2080.

Enfield, D. B., and A.M. Mestas-Nuñez, 1999: Multiscale variabilities in global sea surface temperatures and their relationships with tropospheric climate patterns. *J. Climate*, **12**, 2719–2733.

Enfield, D. B. and D. A. Mayer, 1997: Tropical Atlantic sea surface temperature variability and its relation to El Niño Southern Oscillation. *J. Geophys. Res*. **102**, 929–945.

Fasullo, J., 2004: A stratified diagnosis of the Indian monsoon– Eurasian snow cover relationship. *J. Climate*, **17**, 1110–1122.

Flato, G., and Coauthors, 2013: Evaluation of climate models. *Climate Change 2013: The Physical Science Basis*, T. F. Stocker et al., Cambridge University Press, 741–866.

Folland, C. K., T. N. Palmer, and D. E. Parker, 1986: Sahel rainfall and worldwide sea temperatures, 1901–85. *Nature*, **320**, 602.

Frankignoul, C., and K. Hasselmann, 1977: Stochastic climate models. Part 2. Application to sea-surface temperature variability and thermocline variability. *Tellus*, **29**, 284–305.

Gadgil, S., and S. Gadgil, 2006: The Indian monsoon, GDP and agriculture. *Econ. Polit. Wkly.*, 4887–4895.

Gadgil, S., M. Rajeevan, and R. Nanjundiah, 2005: Monsoon prediction—why yet another failure. *Curr Sci*, **88**, 1389–1400.

Gastineau, G., and C. Frankignoul, 2015: Influence of the North Atlantic SST variability on the atmospheric circulation during the twentieth century. *J. Climate*, **28**, 1396–1416.

Giannini, A., R. Saravanan, and P. Chang, 2003: Oceanic forcing of Sahel rainfall on interannual to interdecadal time scales. *Science*, **302**, 1027–1030.

Gill, A. E., 1980: Some simple solutions for heat-induced tropical circulation. *Quart. J. Roy. Meteor. Soc*., **106**, 447–462.

Good, S. A., M. J. Martin and N. A. Rayner, 2013. EN4: Quality controlled ocean temperature and salinity profiles and monthly objective analyses with uncertainty estimates. *J. Geophys. Res*., **118**, 6704-6716.

Goswami, B.N. 2005: South Asian monsoon. *Intraseasonal variability of the atmosphere–ocean climate system*, Lau, W.K.M., Waliser, D.E. (eds). Springer-Praxis: Berlin Heidelberg; 19–61.

Goswami, P., 1996: A novel neural network design for long range prediction of rainfall pattern. *Curr. Sci. Bangalore*, **70**, 447–457.

Guan, B., and S. Nigam, 2009: Analysis of Atlantic SST variability factoring interbasin links and the secular trend: Clarified structure of the Atlantic multidecadal oscillation. *J. Climate*, **22**, 4228–4240.

Guan, B., and S. Nigam, 2008: Pacific sea surface temperatures in the twentieth century: An evolution-centric analysis of variability and trend. *J. Climate*, **21**, 2790–2809.

Hahn, D. G., and J. Shukla, 1976: An apparent relationship between Eurasian snow cover and Indian monsoon rainfall. *J. Atmos. Sci*., **33**, 2461–2462.

Ham, Y.-G., J.-S. Kug, J.-Y. Park, and F.-F. Jin, 2013: Sea surface temperature in the north tropical Atlantic as a trigger for El Niño/Southern Oscillation events. *Nat. Geosci*., **6**, 112–116.

Hameed, S., K. R. Sperber, and A. Meinster, 1993: Teleconnections of the Southern Oscillation in the tropical Atlantic sector in the OSU coupled upper ocean-atmosphere GCM, *J. Climate.*, **6**, 487-498.

Hare, S. R., and N. J. Mantua, 2000: Empirical evidence for North Pacific regime shifts in 1977 and 1989. *Prog. Oceanogr*., **47**, 103–145.

Harris, I., P. D. Jones, T. J. Osborn, and D. H. Lister, 2014: Updated high-resolution grids of monthly climatic observations–the CRU TS3. 10 Dataset. *Int. J. Climatol.*, **34**, 623-642.

He, S., and H. Wang, 2013: Oscillating relationship between the East Asian winter monsoon and ENSO. *J. Climate*, **26**, 9819-9838.

Hendon, H. H., and B. Liebmann, 1990: Composite study of onset of the Australian summer monsoon. *J. Atmos. Sci*., **47**, 2227–2240.

Hoerling, M. P., J. W. Hurrell, and T. Xu, 2001: Tropical origins for recent North Atlantic climate change. *Science*, **292**, 90–92.

Hoskins, B. J., and M. J. Rodwell, 1995: A model of the Asian summer monsoon. Part I: The global scale. *J. Atmospheric Sci.*, **52**, 1329–1340.

Huffman, G. J., R. F. Adler, D. T. Bolvin, and E. J. Nelkin, 2010: The TRMM Multi-satellite Precipitation Analysis (TMPA). Chapter 1 in *Satellite Rainfall Applications for Surface Hydrology*, F. Hossain and M. Gebremichael, Eds. Springer Verlag, ISBN: 978-90-481-2914-0, 3-22.

Huffman, G. J. and Coauthors, 2007: The TRMM multisatellite precipitation analysis (TMPA): Quasi-global, multiyear, combined-sensor precipitation estimates at fine scales. *J. Hydrometeor.*, **8**, 38-55.

Hurrell, J. W., Y. Kushnir, G. Ottersen, and M. Visbeck, 2003: An overview of the North Atlantic Oscillation. *The North Atlantic Oscillation: Climatic Significance and Environmental Impact*, *Geophys. Monogr*., No. 134, Amer. Geophys. Union, 1–35.

Hurrell, J. W., 1995: Decadal trends in the North Atlantic Oscillation: regional temperatures and precipitation. *Science*, **269**, 676–679.

ICES 2011: Report of the Working Group on Widely Distributed Stocks (WGWIDE). ICES CM 2011/ACOM:15.

Jayanthi, N., and S. Govindachari, 1999: El Nino and NE monsoon rainfall over Tamilnadu. *Mausam*, **50**, 2, 217-218.

Joseph, R., and S. Nigam, 2006: ENSO evolution and teleconnections in IPCC's twentieth-century climate simulations: Realistic representation? *J. Climate*, **19**, 4360–4377.

Joyce, T. M., C. Deser, and M. A. Spall, 2000: The relation between decadal variability of subtropical mode water and the North Atlantic Oscillation. *J. Climate*, **13**, 2550–2569.

Kaiser, H. F., 1958: The varimax criterion for analytic rotation in factor analysis. *Psychometrika*, **23**, 187–200.

Kalnay, E., and Coauthors, 1996: The NCEP/NCAR 40-Year Reanalysis Project. *Bull. Amer. Meteor. Soc.*, **77**, 437–471.

Kang, I.-S., and J. Shukla, 2006: Dynamic seasonal prediction and predictability of the monsoon. *The Asian Monsoon*, Springer, 585–612.

Kang, I.-S., J.-Y. Lee, and C.-K. Park, 2004: Potential predictability of summer mean precipitation in a dynamical seasonal prediction system with systematic error correction. *J. Climate*, **17**, 834–844.

Kavvada, A., A. Ruiz-Barradas, and S. Nigam, 2013: AMO's structure and climate footprint in observations and IPCC AR5 climate simulations. *Climate Dyn.*, **41**, 1345–1364.

Kawamura, R., 1994: A rotated EOF analysis of global sea surface temperature variability with interannual and interdecadal scales. *J. Phys. Oceanogr*., **24**, 707–715.

Knight, J. R., R. J. Allan, C. K. Folland, M. Vellinga, and M. E. Mann, 2005: A signature of persistent natural thermohaline circulation cycles in observed climate. *Geophys. Res. Lett*., **32 (20)**.

Kong, T. M., H. L. Gilroy, and R. C. Leickly, 2004: *Definition of IPHC statistical areas*. International Pacific Halibut Commission.

Kothawale, D. R., and K. Rupa Kumar, 2005: On the recent changes in surface temperature trends over India. *Geophys. Res. Lett*., **32**.

Krishna Kumar, K., M. Hoerling, and B. Rajagopalan, 2005: Advancing dynamical prediction of Indian monsoon rainfall. *Geophys. Res. Lett.*, **32**.

Krishnamurti, T. N., and V. Kumar, 2012: Improved seasonal precipitation forecasts for the Asian monsoon using 16 atmosphere–ocean coupled models. Part II: Anomaly. *J. Climate*, **25**, 65–88.

Krishnamurti, T. N., A. Chakraborty, R. Krishnamurti, W. K. Dewar, and C. A. Clayson, 2006: Seasonal prediction of sea surface temperature anomalies using a suite of 13 coupled atmosphere–ocean models. *J. Climate*, **19**, 6069–6088.

Krishnamurti, T. N., C. M. Kishtawal, T. E. LaRow, D. R. Bachiochi, Z. Zhang, C. E. Williford, S. Gadgil, and S. Surendran, 1999: Improved weather and seasonal climate forecasts from multimodel superensemble. *Science*, **285**, 1548–1550.

Krishnan, R., and Coauthors, 2016: Deciphering the desiccation trend of the South Asian monsoon hydroclimate in a warming world. *Climate Dyn.*, **47**, 1007–1027.

Kumar, A., and M. P. Hoerling, 1995: Prospects and limitations of seasonal atmospheric GCM predictions. *Bull. Am. Meteorol. Soc.*, **76**, 335–345.

Kumar, K. K., R. Kleeman, M. A. Cane, and B. Rajagopalan, 1999: Epochal changes in Indian Monsoon-ENSO precursors. *Geophys. Res. Lett.*, **26**, 75–78.

Kumar, P., K. R. Kumar, M. Rajeevan, and A. K. Sahai, 2007: On the recent strengthening of the relationship between ENSO and northeast monsoon rainfall over South Asia. *Climate Dynamics*, **28**, 649-660.

Kumar, V., and T. N. Krishnamurti, 2012: Improved seasonal precipitation forecasts for the Asian monsoon using 16 atmosphere–ocean coupled models. Part I: Climatology. *J. Climate*, **25**, 39–64.

Latif, M. and N.S. Keenlyside, 2011: A perspective on decadal climate variability and predictability. *Deep Sea Res. Part II: Topical Studies in Oceanogr*., **58** (17-18), 1880-1894.

Lau, K. M., H. T. Wu, and S. Yang, 1998: Hydrologic processes associated with the first transition of the Asian summer monsoon: A pilot satellite study. *Bull. Amer. Meteor. Soc.,* **79**, 1871–1882.

Levitus, S., J. Antonov, and T. Boyer, 2009: Global ocean heat content 1955–2007 in light of recently revealed instrumentation problems. *Geophys. Res. Lett*., **36**, L07608.

Li, L., R. W. Schmitt, C. C. Ummenhofer, and K. B. Karnauskas, 2016a: North Atlantic salinity as a predictor of Sahel precipitation. *Science Advances*, **2**.

Li, L., R. W. Schmitt, C. C. Ummenhofer, and K. B. Karnauskas, 2016b: Implications of North Atlantic sea surface salinity for summer precipitation over the U.S. Midwest: Mechanisms and predictive value. *J. Climate*, **29(9)**, 3143–3159.

Li, X., S.-P. Xie, S. T. Gille, and C. Yoo, 2015: Atlantic-induced pan-tropical climate change over the past three decades. *Nat. Climate Change*, **6**, 275–279.

Lindzen, R. S., and S. Nigam, 1987: On the role of sea surface temperature gradients in forcing low-level winds and convergence in the tropics. *J. Atmos. Sci*., **44**, 2418–2436.

Liu, Z., and M. Alexander, 2007: Atmospheric bridge, oceanic tunnel, and global climatic teleconnections. *Rev. Geophys.*, **45**.

Madden, R. A., and P. R. Julian, 1971: Detection of a 40–50 day oscillation in the zonal wind in the tropical Pacific. *J. Atmos. Sci*., **28**, 702–708.

Madden, R. A., and P. R. Julian, 1972: Description of global-scale circulation cells in the tropics with a 40–50 day period. *J. Atmos. Sci*., **29**, 1109–1123.

Manabe, S., D. G. Hahn, and J. L. Holloway Jr, 1974: The seasonal variation of the tropical circulation as simulated by a global model of the atmosphere. *J. Atmos. Sci.*, **31**, 43–83.

Mantua, N. J., S. R. Hare, Y. Zhang, J.M.Wallace, and R. C. Francis, 1997: A Pacific interdecadal climate oscillation with impacts on salmon production. *Bull. Amer.Meteor. Soc*., **78**, 1069–1079.

Marshall, J., and Coauthors, 2001: North Atlantic climate variability: phenomena, impacts and mechanisms. *Int. J. Climatol. J. R. Meteorol. Soc.*, **21**, 1863–1898.

Matsumoto, J., 1997: Seasonal transition of summer rainy season over Indochina and adjacent monsoon region. *Adv. Atmos. Sci*, **14**, 231–245.

Matsumoto J. 1990: The seasonal changes of wind fields in the global tropics. *Geographical Review of Japan*, **63B**, 156–178.

Matsuno, T., 1966: Quasi-geostrophic motions in the equatorial area. *J. Meteor. Soc. Japan*, **44**, 25–43.

McCabe, G. J., and M. A. Palecki, 2006: Multidecadal climate variability of global lands and oceans. *Int. J. Climatol*., **26**, 849–865.

McCabe, G. J., M. A. Palecki, and J. L. Betancourt, 2004: Pacific and Atlantic Ocean influences on multidecadal drought frequency in the United States. *Proc. Natl. Acad. Sci.*, **101**, 4136–4141.

McGregor, S., A. Timmermann, M. F. Stuecker, M. H. England, M. Merrifield, F.-F. Jin, and Y. Chikamoto, 2014: Recent Walker circulation strengthening and Pacific cooling amplified by Atlantic warming. *Nat. Climate Change*, **4**, 888–892.

Menon, A., A. Levermann, J. Schewe, J. Lehmann, and K. Frieler, 2013: Consistent increase in Indian monsoon rainfall and its variability across CMIP-5 models. *Earth Syst. Dyn*., **4**, 287–300.

Messié, M., and F. Chavez, 2011: Global modes of sea surface temperature variability in relation to regional climate indices. *J. Climate*, **24**, 4314–4331

Mestas-Nuñez, A.M., and D.B. Enfield, 1999: Rotated global modes of non-ENSO sea surface temperature variability. *J. Climate*, **12**, 2734–2746.

Mishra, V., B. V. Smoliak, D. P. Lettenmaier, and J. M. Wallace, 2012: A prominent pattern of year-to-year variability in Indian Summer Monsoon Rainfall. *Proc. Natl. Acad. Sci*., **109**, 7213–7217.

Mooley, D. A., B. Parthasarathy, and N. A. Sontakke, 1985: Relationship between all-India summer monsoon rainfall and southern oscillation/eastern equatorial Pacific sea surface temperature. *Proc. Indian Acad. Sci.-Earth Planet. Sci.*, **94**, 199–210.

Namias, J., 1966: Nature and possible causes of the northeastern United States drought during 1962–65. *Mon Wea Rev*, **94**, 543–554.

Namias, J., 1950: The index cycle and its role in the general circulation. *J. Meteorol.*, **7**, 130–139.

Navone, H. D., and H. A. Ceccatto, 1994: Predicting Indian monsoon rainfall: a neural network approach. *Climate Dyn.*, **10**, 305–312.

NEFSC (Northeast Fisheries Science Center) 1996: Report of the 20th Northeast Regional Stock Assessment Workshop (20th SAW): Stock Assessment Review Committee (SARC) consensus summary of assessments. *Northeast Fish. Sci. Cent. Ref. Doc*. 95-18. 211 p.

NEFSC (Northeast Fisheries Science Center) 2006: 42nd Northeast Regional Stock Assessment Workshop (42nd SAW) stock assessment report, part A: silver

hake, Atlantic mackerel, and northern shortfin squid (CRD 06-09a). *U.S. Dep. Commer., Northeast Fish. Sci. Cent. Ref. Doc*. 06-09a; 284 p.

NEFSC (Northeast Fisheries Science Center) 2018: 64th Northeast Regional Stock Assessment Workshop (64th SAW) Assessment Summary Report *U.S. Dep. Commer., Northeast Fish. Sci. Cent. Ref. Doc*. 18-03; 27 p.

Nigam, S., A. Sengupta, and A. Ruiz-Barradas, 2019: Atlantic-Pacific Links in Observed Multidecadal SST Variability: Is Atlantic Multidecadal Oscillation's Phase-Reversal Orchestrated by Pacific Decadal Oscillation? submitted to *J. Climate.*

Nigam, S., A. Ruiz-Barradas, and L. Chafik, 2018: Gulf Stream excursions and sectional detachments generate the decadal pulses in the Atlantic multidecadal oscillation. *J. Climate*, **31**, 2853–2870.

Nigam, S., N.P. Thomas, A. Ruiz-Barradas, and S.J. Weaver, 2017: Striking seasonality in the secular warming of the northern continents: structure and mechanisms. *J. Climate*, **30**, 6521–6541.

Nigam, S., and A. Ruiz-Barradas, 2016: Key role of the Atlantic multidecadal oscillation in twentieth century drought and wet periods over the US Great Plains and the Sahel. *Dynamics and Predictability of Large-Scale, High-Impact Weather and Climate Events*, J. Li, R. Swinbank, H. Volkert, and R. Grotjahn, Eds., Cambridge University Press, 255–270.

Nigam, S., B. Guan, and A. Ruiz-Barradas, 2011: Key role of the Atlantic multidecadal oscillation in 20th century drought and wet periods over the Great Plains. *Geophys. Res. Lett.*, **38**.

Nigam, S., and B. Guan, 2011: Atlantic tropical cyclones in the twentieth century: Natural variability and secular change in cyclone count. *Climate Dyn.*, **36**, 2279–2293.

Nigam, S. and A. Ruiz-Barradas, 2006: Seasonal hydroclimate variability over North America in global and regional reanalyses and AMIP simulations: Varied representation. *J. Climate*, **19,** 815-837.

Nigam, S., J. Pyle, and J. A. Curry, 2003: *Teleconnections. Encyclopedia of atmospheric sciences*. Academic Press London.

Nigam, S., C. Chung, and E. DeWeaver, 2000: ENSO diabatic heating in ECMWF and NCEP reanalyses, and NCAR CCM3 simulation. *J. Climate*, **13**, 3152–3171.

Nigam, S., M. Barlow, and E. H. Berbery, 1999: Pacific decadal SST variability: Impact on U.S. drought and streamflow. *Eos Transactions, AGU*, **Vol. 80, 51**, 621–625.

Nigam, S., and Y. Chao, 1996: Evolution dynamics of tropical ocean-atmosphere annual cycle variability. *J. Climate*, **9**, 3187–3205.

Nigam, S., and H.-S. Shen, 1993: Structure of oceanic and atmospheric low-frequency variability over the tropical Pacific and Indian Oceans. Part I: COADS observations. *J. Climate*, **6**, 657– 676.

Nitta, T., and S. Yamada, 1989: Recent warming of tropical sea surface temperature and its relationship to the Northern Hemisphere circulation. *Journal of the Meteorological Society of Japan*, **67**, 375–383.

North, G. R., T. L. Bell, R. F. Cahalan, and F. J. Moeng, 1982: Sampling errors in the estimation of empirical orthogonal functions. *Mon. Wea. Rev.*, **110**, 699–706.

O'Reilly, C.H., M. Huber, T. Woollings, and L. Zanna, 2016: The signature of low-frequency oceanic forcing in the Atlantic Multidecadal Oscillation. *Geophys. Res. Lett*., **43**(6), 2810-2818.

Palmer, M.C., 2014: Assessment update report of the Gulf of Maine Atlantic cod stock. US Department of Commerce, Northeast Fish. Sci. Cent. Ref. Doc. 14-14; 119 p.

Palmer, T. N., Č. Branković, P. Viterbo, and M. J. Miller, 1992: Modeling interannual variations of summer monsoons. *J. Climate*, **5**, 399–417.

Pant, G. B., and K. R. Kumar, 1997: *Climates of South Asia*. Wiley, 320 pp.

Park, J.H., T. Li, S.W. Yeh, and H. Kim, 2019: Effect of recent Atlantic warming in strengthening Atlantic–Pacific teleconnection on interannual timescale via enhanced connection with the Pacific meridional mode. *Climate Dyn.*, 1-17.

Parvathi, V., I. Suresh, M. Lengaigne, T. Izumo, and J. Vialard, 2017: Robust projected weakening of winter monsoon winds over the Arabian Sea under climate change. *Geophysical Research Letters*, **44**.

Pillai, P. A., S. A. Rao, R. S. Das, K. Salunke, and A. Dhakate, 2018: Potential predictability and actual skill of Boreal Summer Tropical SST and Indian summer monsoon rainfall in CFSv2-T382: Role of initial SST and teleconnections. *Climate Dyn.*, **51**, 493–510.

Quenouille, M.H., 1952: Associated measurements. Academic Press, New York.

Rajeevan, M., C. K. Unnikrishnan, and B. Preethi, 2012: Evaluation of the ENSEMBLES multi-model seasonal forecasts of Indian summer monsoon variability. *Climate Dyn.*, **38**, 2257–2274.

Rajeevan, M., D. S. Pai, R. A. Kumar, and B. Lal, 2007: New statistical models for long-range forecasting of southwest monsoon rainfall over India. *Climate Dyn.*, **28**, 813–828.

Ramu, D. A., and Coauthors, 2017: Prediction of seasonal summer monsoon rainfall over homogenous regions of India using dynamical prediction system. *J. Hydrol.*, **546**, 103–112.

Rasmusson, E. M., and T. H. Carpenter, 1983: The relationship between eastern equatorial Pacific SSTs and rainfall over India and Sri Lanka. *Mon. Wea. Rev*., **111**, 517–528.

Rayner, N. A., D. E. Parker, E. B. Horton, C. K. Folland, L. V. Alexander, D. P. Rowell, E. C. Kent, and A. Kaplan, 2003: Global analyses of sea surface temperature, sea ice, and night marine air temperature since the late nineteenth century. *J. Geophys. Res*., **108**, 4407.

Richman, M. B., 1986: Rotation of principal components. *J. Climatol.*, **6**, 293–335.

Rogers, J. C., 1984: The association between the North Atlantic Oscillation and the Southern Oscillation in the northern hemisphere. *Mon. Wea. Rev.*, **112**, 1999–2015.

Ropelewski, C. F., and M. S. Halpert, 1987: Global and regional scale precipitation patterns associated with the El Niño/Southern Oscillation. *Mon. Wea. Rev*.,**115**, 1606–1626.

Ruiz-Barradas A., S. Nigam, and A. Kavvada, 2013: The Atlantic Multidecadal Oscillation in 20th Century Climate Simulations: Uneven Progress from CMIP3 to CMIP5. *Climate Dyn.*, **41**, 3301-3315.

Ruiz-Barradas, A., and S. Nigam, 2005: Warm season rainfall variability over the US Great Plains in observations, NCEP and ERA-40 reanalyses, and NCAR and NASA atmospheric model simulations. *J. Climate*, **18**, 1808–1830.

Ruiz-Barradas, A., J. A. Carton, and S. Nigam, 2000: Structure of interannual-to-decadal climate variability in the tropical Atlantic sector. *J. Climate*, **13**, 3285–3297.

Saha, S. K., and Coauthors, 2016: Potential predictability of Indian summer monsoon rainfall in NCEP CFSv2. *J. Adv. Model. Earth Syst.*, **8**, 96–120.

Sahai, A. K., R. Chattopadhyay, and B. N. Goswami, 2008: A SST based large multi-model ensemble forecasting system for Indian summer monsoon rainfall. *Geophys. Res. Lett*., **35**.

Sahai, A. K., A. M. Grimm, V. Satyan, and G. B. Pant, 2003: Long-lead prediction of Indian summer monsoon rainfall from global SST evolution. *Climate Dyn*., **20**, 855–863.

Santer, B. D., T. M. L. Wigley, J. S. Boyle, D. J. Gaffen, J. J. Hnilo, D. Nychka, D. E. Parker, and K. E. Taylor, 2000: Statistical significance of trends and trend differences in layer-averaged atmospheric temperature time series. *J. Geophys. Res*., **105**, 7337–7356.

Schneider, U., A. Becker, P. Finger, A. Meyer-Christoffer, and M. Ziese, 2018: GPCC Full Data Monthly Product Version 2018 at 0.5◦: Monthly Land-Surface Precipitation from Rain-Gauges Built on GTS-Based and Historical Data. *Dtsch. Wetterd. Offenb. Am Main Ger.*,.

Schneider, U., A. Becker, P. Finger, A. Meyer-Christoffer, M. Ziese, and B. Rudolf, 2013: GPCC's new land surface precipitation climatology based on quality-controlled in situ data and its role in quantifying the global water cycle. *Theoretical and Applied Climatology*, **115**, 15-40.

Seager, R., Y. Kushnir, C. Herweijer, N. Naik, and J. Velez, 2005: Modeling of tropical forcing of persistent droughts and pluvials over western North America: 1856–2000. *J. Climate*, **18**, 4065–4088.

SEDAR 2015: SEDAR 40 – Atlantic Menhaden Stock Assessment Report. SEDAR, North Charleston, SC, 643 pp.

Sengupta, A., and S. Nigam, 2019: The Northeast Winter Monsoon over the Indian Subcontinent and Southeast Asia: Evolution, Interannual Variability, and Model Simulations. *J. Climate*, **32**, 231–249.

Sengupta, A., and M. Rajeevan, 2013: Uncertainty quantification and reliability analysis of CMIP5 projections for the Indian summer monsoon. *Curr. Sci.*, **105**, 1692–1703.

Sharmila, S., S. Joseph, A. K. Sahai, S. Abhilash, and R. Chattopadhyay, 2015: Future projection of Indian summer monsoon variability under climate change scenario: An assessment from CMIP5 climate models. *Global and Planetary Change*, **124**, 62–78.

Shige, S., Y. Nakano, and M. K. Yamamoto, 2017: Role of orography, diurnal cycle, and intraseasonal oscillation in summer monsoon rainfall over the Western Ghats and Myanmar Coast. *J. Climate*, **30**, 9365–9381.

Shukla, J., and D. A. Mooley, 1987: Empirical prediction of the summer monsoon rainfall over India. *Mon. Weather Rev.*, **115**, 695–704.

Shukla, J., and D. A. Paolino, 1983: The Southern Oscillation and long-range forecasting of the summer monsoon rainfall over India. *Mon. Weather Rev.*, **111**, 1830–1837.

Siew, J. H., F.T. Tangang, L. Juneng, 2014: Evaluation of CMIP5 coupled atmosphere–ocean general circulation models and projection of the Southeast Asian winter monsoon in the 21st century. *Int. J. Climatol*., **34 (9)**, 2872–2884.

Sikka, D. R., 1980: Some aspects of the large scale fluctuations of summer monsoon rainfall over India in relation to fluctuations in the planetary and regional scale circulation parameters. *Proc. Indian Acad. Sci.-Earth Planet. Sci.*, **89**, 179–195.

Singh, N., and N. A. Sontakke, 1999: On the variability and prediction of the rainfall in the post-monsoon season over India. *Int. J. Climatol*, **19**, 300–309.

Slingo, J., H. Spencer, B. Hoskins, P. Berrisford, and E. Black, 2005: The meteorology of the Western Indian Ocean, and the influence of the East African Highlands. *Philos. Trans. R. Soc. Math. Phys. Eng. Sci.*, **363**, 25–42.

Sooraj, K.P., P. Terray and M. Mujumdar, 2015: Global warming and the weakening of the Asian summer Monsoon circulation: Assessments from the CMIP5 models. *Climate Dynamics*, **45**, 1–20.

Sperber, K. R., J. M. Slingo, and H. Annamalai, 2000: Predictability and the relationship between subseasonal and interannual variability during the Asian summer monsoon. *Quart. J. Roy. Meteor. Soc*., **126**, 2545–2574.

Sperber, K. R., and T. N. Palmer, 1996: Interannual tropical rainfall variability in general circulation model simulations associated with the Atmospheric Model Intercomparison Project. *J. Climate*, **9**, 2727–2750.

Sridharan, S., and A. Muthuswamy, 1990: Northeast monsoon rainfall in relation to El-Nino, QBO and Atlantic hurricane frequency. *Vayu Mandal*, **20 (3-4)**, 104-111.

Srinivasan, V., and K. Ramamurthy, 1973: Forecasting manual, part IV: Comprehensive articles on selected topics—Northeast monsoon. India Meteorological Department Field Meteorological Unit Rep. IV-18.4, 132 pp

Stewart, I. J., and S. Martell, 2014: Assessment of the Pacific halibut stock at the end of 2014. *IPHC Report of Assessment and Research Activities 2014*, 161–180.

Sun, C., F. Kucharski, J. Li, F. Jin, I. Kang, and R. Ding, 2017: Western tropical Pacific multidecadal variability forced by the Atlantic multidecadal oscillation. *Nat. Commun*., **8**, 15998.

Sun, Y., S.C. Clemens, C. Morrill, X. Lin, X. Wang, and Z. An, 2011: Influence of Atlantic meridional overturning circulation on the East Asian winter monsoon. *Nature Geoscience*, **5(1)**, 46-49.

Suppiah, R., 1997: Extremes of the southern oscillation phenomenon and the rainfall of Sri Lanka. *Int. J. Climatol.,* **17,** 87– 101.

Taylor, K. E., R. J. Stouffer, and G. A. Meehl, 2012: An overview of CMIP5 and the experiment design. *Bull. Amer. Meteor. Soc*., **93**, 485–498.

Thapliyal, V., 1981: ARIMA model for long-range prediction of monsoon rainfall in Peninsular India. *India Meteorol. Dep. Monogr. Climatol.*, **12**, 81.

Thomas, N., and S. Nigam, 2018: Twentieth-century climate change over Africa: Seasonal hydroclimate trends and Sahara Desert expansion. *J. Climate*, **31**, 3349–3370.

Ting, M. and H. Wang, 1997: Summertime US Precipitation Variability and Its Relation to Pacific Sea Surface Temperature. *J. Climate*, **10**, 1853-1873.

Toresen, R., and O.J. Østvedt, 2000: Variation in abundance of Norwegian spring-spawning herring (*Clupea harengus*, Clupeidae) throughout the 20th century and the influence of climatic fluctuations. *Fish Fish*. **1**, 231–256.

Turner, A. G., and H. Annamalai, 2012: Climate change and the South Asian summer monsoon. *Nat. Clim. Change*, **2**, 587–595.

Villafuerte, M. Q., J. Matsumoto, I. Akasaka, H. G. Takahashi, H. Kubota, and T. A. Cinco, 2014: Long-term trends and variability of rainfall extremes in the Philippines. *Atmos. Res.*, **137**, 1–13.

Waliser, D. E., 2006: Intraseasonal variations. *The Asian Monsoon*, B. Wang, Ed., Springer, 787 pp.

Waliser, D. E., and Coauthors, 2003: AGCM simulations of intraseasonal variability associated with the Asian summer monsoon. *Climate Dyn.*, **21**, 423–446.

Waliser, D.E., K.M. Lau, W. Stern, and C. Jones, 2003: Potential predictability of the Madden–Julian oscillation. *Bull. Amer. Meteor. Soc.*, **84**, 33–50.

Walker, G. T., 1910: On the meteorological evidence for supposed changes of climate in India. *Mem. Indian Meteor.*, **21**, 1–21.

Walker, G. T., 1923: Correlation in seasonal variations of weather, VIII: a preliminary study of world weather. Memoires of the Indian Meteorological Department, Calcutta, **24**, 75–131.

Wang, B., and LinHo, 2002: Rainy season of the Asian-Pacific summer monsoon. *J. Climate*, **15**, 386-398.

Wang, B., and Q. Zhang, 2002: Pacific–East Asian teleconnection. Part II: How the Philippine Sea anomalous anticyclone is established during El Niño development. *J. Climate*, **15**, 3252–3265.

Wang, C., 2006: An overlooked feature of tropical climate: Inter-Pacific-Atlantic variability, *Geophys. Res. Lett.*, **33**, L12702.

Wang, H. and S. He, 2012: Weakening relationship between East Asian winter monsoon and ENSO after mid-1970s. *Chinese Science Bulletin*, 1-6.

Wang, L., W. Chen, and R. Huang, 2008: Interdecadal modulation of PDO on the impact of ENSO on the East Asian winter monsoon. *Geophys. Res. Lett.*, **35(20)**.

Watanabe, M., and F.-F. Jin, 2002: Role of Indian Ocean warming in the development of Philippine Sea anticyclone during ENSO. *Geophys. Res. Lett*., **29**, 1478.

Weare, B. C., and J. S. Nasstrom, 1982: Examples of extended empirical orthogonal function analyses. *Mon. Wea. Rev*., **110**, 481–485.

Wheeler, M. C., and H. H. Hendon, 2004: An all-season real-time multivariate MJO index: Development of an index for monitoring and prediction. *Mon. Wea. Rev,*, **132**, 1917–1932.

Wilks, D.S., 2006: *Statistical methods in the atmospheric sciences, Second Edition*, Academic Press, 630pp.

Yang, D., Y. Tang, Y. Zhang, and X. Yang, 2012: Information-based potential predictability of the Asian summer monsoon in a coupled model. *J. Geophys. Res. Atmospheres*, **117**.

Yasunaka, S., and K. Hanawa, 2005: Regime shift in the global sea-surface temperatures: Its relation to El Niño-Southern Oscillation events and dominant variation modes. *Int. J. Climatol*., **25**, 913–930.

Yatagai, A., K. Kamiguchi, O. Arakawa, A. Hamada, N. Yasutomi, and A. Kitoh, 2012: APHRODITE: Constructing a long-term daily gridded precipitation dataset for Asia based on a dense network of rain gauges. *Bull. Amer. Meteor. Soc*., **93**, 1401-1415.

Zhang, R., 2017: On the persistence and coherence of subpolar sea surface temperature and salinity anomalies associated with the Atlantic multidecadal variability. *Geophys. Res. Lett*., **44**(15), 7865-7875.

Zhang, R., R. Sutton, G. Danabasoglu, T.L. Delworth, W.M. Kim, J. Robson, and S.G. Yeager, 2016: Comment on "The Atlantic Multidecadal Oscillation without a role for ocean circulation". *Science*, **352**(6293), 1527-1527.

Zhang, R., T. L. Delworth, R. Sutton, D. L. Hodson, K. W. Dixon, I. M. Held, Y. Kushnir, J. Marshall, Y. Ming, R. Msadek, and J. Robson, 2013: Have aerosols caused the observed Atlantic multidecadal variability*? J. Atmos. Sc*., **70**(4), 1135-1144.

Zhang, R., and G. K. Vallis, 2006: Impact of great salinity anomalies on the low-frequency variability of the North Atlantic climate. *J. Climate*, **19**, 470–482.

Zhang, R., and T. L. Delworth, 2006: Impact of Atlantic multidecadal oscillations on India/Sahel rainfall and Atlantic hurricanes. *Geophys. Res. Lett.*, **33**.

Zhou, W., X. Wang, T. J. Zhou, C. Li, and J. C. L. Chan, 2007: Interdecadal variability of the relationship between the East Asian winter monsoon and ENSO. *Meteor. Atmos. Phys.*, **98**, 283–293.

Zubair, L. and C. F. Ropelewski, 2006: The strengthening relationship between ENSO and northeast monsoon rainfall over Sri Lanka and southern India. *J. Climate*, **19**, 1567-1575.